GNSS-based remote sensing: Innovative observation of key hydrological parameters in the Central Andes

Nikolaos Antonoglou

Univ.-Diss.

presented for the academic degree of
"doctor rerum naturalium"
(Dr. rer. nat.)
in the scientific discipline "Remote Sensing"

submitted to the
Faculty of Science
Institute of Geosciences
of the University of Potsdam
and
Facultad de Ciencias Naturales
e Instituto Miguel Lillo
of the Universidad Nacional de Tucumán

Place and date of the disputation:
Potsdam 29.01.2024

Principal Supervisor: Prof. Dr. Bodo Bookhagen
Second Supervisor: Prof. Dr. Jens Wickert
Mentor: Prof. Dr. Andreas Güntner
Assessor: Prof. Dr. Alejandro de la Torre

Published online on the Publication Server of the University of Potsdam:
https://doi.org/10.25932/publishup-62825
https://nbn-resolving.org/urn:nbn:de:kobv:517-opus4-628256

Declaration of Authorship

I, Nikolaos Antonoglou, hereby declare that the work presented in this thesis is the result of my own investigation and that clear references are stated in the text when the work of others is used. The entire Chapter 8 and parts of Chapters 2 and 9 have been published in Antonoglou et al. (2022b). All other parts of this manuscript have yet to be submitted for assessment, either at the University of Potsdam or elsewhere.

The investigation was held within the framework of the International Research Training Group-StRATEGy, and carried out at the University of Potsdam and the German Research Centre for Geosciences (Deutsches GeoForschungsZentrum—GFZ). The project was co-supervised by the Universidad Nacional de Tucumán, Argentina (CUAA-DAHZ binational doctorate program).

Signed: _____

Date: _____

Acknowledgements

Firstly, I would like to thank my family and my wife for supporting me during this long trip. Their help is priceless; without it, I would not be able to finalize this study. Additionally, I would like to thank my supervisors, Prof. Dr. Bodo Bookhagen and Prof. Dr. Jens Wickert. They were always willing to assist me, and this thesis was accomplished with their guidance. I would also like to thank Prof. Dr. Alejandro de la Torre for his valuable comments and his assistance during my stays in Argentina. Without Dr. Markus Ramatschi's assistance, I would not have been able to complete this study. He patiently spent a lot of time working with me to address challenges and gave me access to helpful equipment. The campaign for the installation of the stations in Argentina was only possible with the cooperation with Prof. Dr. Fernando Hongn and Luis Alvarado. Finally, I want to thank my friends for supporting me and helping me get through all of the challenges I had in life.

Nikolaos Antonoglou

GNSS-based remote sensing: Innovative observation of key hydrological parameters in the Central Andes

Nikolaos Antonoglou

Submitted for the degree of *Dr. rer. nat.*
Potsdam, January 2024

Abstract

The Central Andean region is characterized by diverse climate zones with sharp transitions between them. In this work, the area of interest is the South-Central Andes in northwestern Argentina that borders with Bolivia and Chile. The focus is the observation of soil moisture and water vapour with Global Navigation Satellite System (GNSS) remote-sensing methodologies. Because of the rapid temporal and spatial variations of water vapour and moisture circulations, monitoring this part of the hydrological cycle is crucial for understanding the mechanisms that control the local climate. Moreover, GNSS-based techniques have previously shown high potential and are appropriate for further investigation. This study includes both logistic-organization effort and data analysis. As for the prior, three GNSS ground stations were installed in remote locations in northwestern Argentina to acquire observations, where there was no availability of third-party data.

The methodological development for the observation of the climate variables of soil moisture and water vapour is independent and relies on different approaches. The soil-moisture estimation with GNSS reflectometry is an approximation that has demonstrated promising results, but it has yet to be operationally employed. Thus, a more advanced algorithm that exploits more observations from multiple satellite constellations was developed using data from two pilot stations in Germany. Additionally, this algorithm was slightly modified and used in a sea-level measurement campaign. Although the objective of this application is not related to monitoring hydrological parameters, its methodology is based on the same principles and helps to evaluate the core algorithm. On the other hand, water-vapour monitoring with GNSS observations is a well-established technique that is utilized operationally. Hence, the scope of this study is conducting a meteorological analysis by examining the along-the-zenith air-moisture levels and introducing indices related to the azimuthal gradient.

The results of the experiments indicate higher-quality soil moisture observations with the new algorithm. Furthermore, the analysis using the stations in northwestern Argentina illustrates the limits of this technology because of varying soil conditions and shows future research directions. The water-vapour analysis points out the strong influence of the topography on atmospheric moisture circulation and rainfall generation. Moreover, the GNSS time series allows for the identification of seasonal signatures, and the azimuthal-gradient indices permit the detection of main circulation pathways.

GNSS-gestützte Fernerkundung: Innovative Beobachtung grundlegender hydrologischer Parameter in den Zentralanden

Nikolaos Antonoglou

Vorgelegt zur Erlangung des akademischen Grades *Dr. rer. nat.*
Potsdam, Januar 2024

Zusammenfassung

Die Zentralanden sind eine Region, in der verschiedene Klimazonen nur durch kurze Übergänge gekennzeichnet sind. Der geographische Schwerpunkt dieser Arbeit liegt in den südlichen Zentralanden im Grenzgebiet zwischen Argentinien, Bolivien und Chile, und der wissenschaftliche Schwerpunkt ist in der Überwachung der Bodenfeuchtigkeit und des Wasserdampfs mit Fernerkundungsmethoden des Globales Navigationssatellitensystem (Global Navigation Satellite System - GNSS) angesiedelt. Wegen der raschen zeitlichen und räumlichen Schwankungen des Wasserdampfs und den damit häufig verbundenen Niederschlägen und der Feuchtigkeitszirkulation ist die Beobachtung dieses Teils des hydrologischen Zyklus von entscheidender Bedeutung für das Verständnis des lokalen Klimas. Darüber hinaus haben GNSS-gestützte Techniken in anderen Studien bereits ein hohes Potenzial gezeigt, erfordern aber in einigen Bereichen weitere Untersuchungen. Diese Studie umfasst sowohl logistischen Aufwand als auch Datenanalyse. Dazu wurden drei GNSS-Bodenstationen in abgelegenen Orten im Nordwesten Argentiniens installiert, um Beobachtungen zu sammeln, da dort keine externen Daten verfügbar waren.

Die methodische Entwicklung für die Beobachtung der Klimavariablen Bodenfeuchtigkeit und Wasserdampfs ist unabhängig voneinander. Die Messung der Bodenfeuchte mit Hilfe der GNSS-Reflektometrie ist eine Annäherung, die vielversprechende Ergebnisse erbracht hat, aber bisher noch nicht operationell eingesetzt wurde. Daher wurde ein fortschrittlicherer Algorithmus entwickelt, der Beobachtungen von mehreren Satellitenkonstellationen nutzt und unter anderem Daten von zwei Pilotstationen in Deutschland verwendet. Außerdem wurde dieser Algorithmus leicht modifiziert und in einer Meeresspiegelmesskampagne eingesetzt. Obwohl diese Andwendung nicht direkt mit der Überwachung hydrologischer Parameter zusammenhängt, basiert die Methodik auf denselben Prinzipien und hilft bei der Bewertung des entwickelten Algorithmus. Auf der anderen Seite ist die Überwachung des Wasserdampfs mit GNSS-Beobachtungen eine anerkannte Technik, die in der Praxis bereits seit mehreren Jahren eingesetzt wird. Diese Studie befasst sich daher mit der Durchführung einer meteorologischen Analyse der Luftfeuchtigkeitswerte entlang des Zenits und der Entwicklung von klimatischen Indizes, die sich auf den azimutalen Gradienten beziehen.

Die Ergebnisse der Experimente zeigen, dass die Qualität der Bodenfeuchtebeobachtungen mit dem neuen Algorithmus vielversprechend und besser sind. Darüber hinaus zeigt die Analyse anhand der Stationen im nordwesten Argentiniens die Grenzen dieser Technologie aufgrund der sehr unterschiedlichen Bodenbedingungen auf und gibt mögliche zukünftige Forschungsrichtung an. Die Wasserdampfanalyse verdeutlicht den Einfluss der Topographie auf die Luftfeuchtigkeit und der Regenmenge. Außerdem ermöglichen die GNSS-Zeitreihen die Identifizierung der jahreszeitlichen Signaturen, und Messungen der azimutal Gradienten erlauben die Erkennung der wichtigsten Zirkulationswege.

Contents

List of Figures

List of Tables

List of Abbreviations

asl	**a**bove **s**ea **l**evel
C/A	**C**oarse/**A**cquisition
C/N$_0$	**c**arrier-to-**n**oise density
CDMA	**C**ode **D**ivision **M**ultiple **A**ccess
CHAMP	**Cha**llenging **M**inisatellite **P**ayload
CRNS	**C**osmic-**R**ay **N**euron **S**ensing
DDM	**d**elay-**D**oppler **m**ap
EPOS	**E**arth **P**arameter and **O**rbit **S**ystem
ESA	**E**uropean **S**pace **A**gency
EU	**E**uropean **U**nion
EVI	**e**nhanced **v**egetation **i**ndex
E-W	**e**ast-**w**est
FDMA	**F**requency **D**ivision **M**ultiple **A**ccess
FDR	**F**requency-**D**omain **R**eflectometry
GFZ	Deutsches **G**eo**F**orschungs**Z**entrum - ger (German Research Centre for Geosciences)
GLONASS	**Glo**balnaya **Na**vigazionnaya **S**putnikovaya **S**istema -rus (Global Navigation Satellite System)
GNSS	**G**lobal **N**avigation **S**atellite **S**ystem
GNSS-R	**G**lobal **N**avigation **S**atellite **S**ystem **R**eflectometry
GPS	**G**lobal **P**ositioning **S**ystem
GPS/MET	**G**lobal **P**ositioning **S**ystem/**Met**eorology
GRACE	**G**ravity **R**ecovery **a**nd **C**limate **E**xperiment
IGN	**I**nstituto **G**eográfico **N**acional - sp (National Geographic Institute)
IRNSS	**I**ndian **R**egional **N**avigational **S**atellite **S**ystem
LEO	low **E**arth **o**rbit
LLJ	low-**l**evel **j**et
MCS	**M**esoscale **C**onvective **S**ystem
MEO	**m**edium **E**arth **o**rbit
NASA	**N**ational **A**eronautics and **S**pace **A**dministration
NAVIC	**Nav**igation **I**ndian **C**onstellation
NAVSTAR GPS	**Nav**igation **S**ystem with **T**ime **a**nd **R**anging **G**lobal **P**ositioning **S**ystem
NDVI	**n**ormalized **d**ifference **v**egetation **i**ndex
NGL	**N**evada **G**eodetic **L**aboratory
N-S	**n**orth-**s**outh
P-code	**P**recise code
PR China	**P**eoples **R**epublic of **China**
PRN	**p**seudo-**r**andom **n**oise
QZSS	**Q**uasi-**Z**enith **S**atellite **S**ystem
RO	**R**adio **O**ccultation
RINEX	**R**eceiver **In**dependent **Ex**change
RMSE	**r**oot-**m**ean-**s**quare **e**rror
SAMS	**S**outh **A**merican **M**onsoon **S**ystem
SAOCOM	**S**atélite **A**rgentino de **O**bservación **co**n **M**icroondas -sp (Argentine Microwaves Observation Satellite)

SEVIRI	**S**pinning **E**nhanced **V**isible **I**nfra-**R**ed **I**mager
SMAP	**S**oil **M**oisture **A**ctive **P**assive
SMOS	**S**oil **M**oisture and **O**cean **S**alinity
SMMR	**S**canning **M**ultichannel **M**icrowave **R**adiometer
SNR	**s**ignal-to-**n**oise **r**atio
STD	**S**lant **T**otal **D**elay
TDR	**T**ime-**D**omain **R**eflectometry
TG	**T**ide **G**auge
TRMM	**T**ropical **R**ainfall **M**easuring **M**ission
UP	**U**niversity of **P**otsdam
USA	**U**nited **S**tates of **A**merica
ZHD	**Z**enith **H**ydrostatic **D**elay
ZTD	**Z**enith **T**otal **D**elay
ZWD	**Z**enith **W**et **D**elay

Chapter 1

Introduction

The Central Andes extend between the Gulf of Guayaquil in Ecuador at 15S and the Gulf of Penas in Chile at 30S, and they exemplify the impacts of the tectonic evolution on the climate of South America (Allmendinger et al., 1997). The climate conditions in the Central Andean Plateau (also referred as Altiplano-Puna Plateau), the eastern and western flanks of the Andean Cordillera, the intermontane valleys and gorges, the Sierras Pampeanas, and the low plains constitute a diverse environment. In combination with the complex topography, the circulation

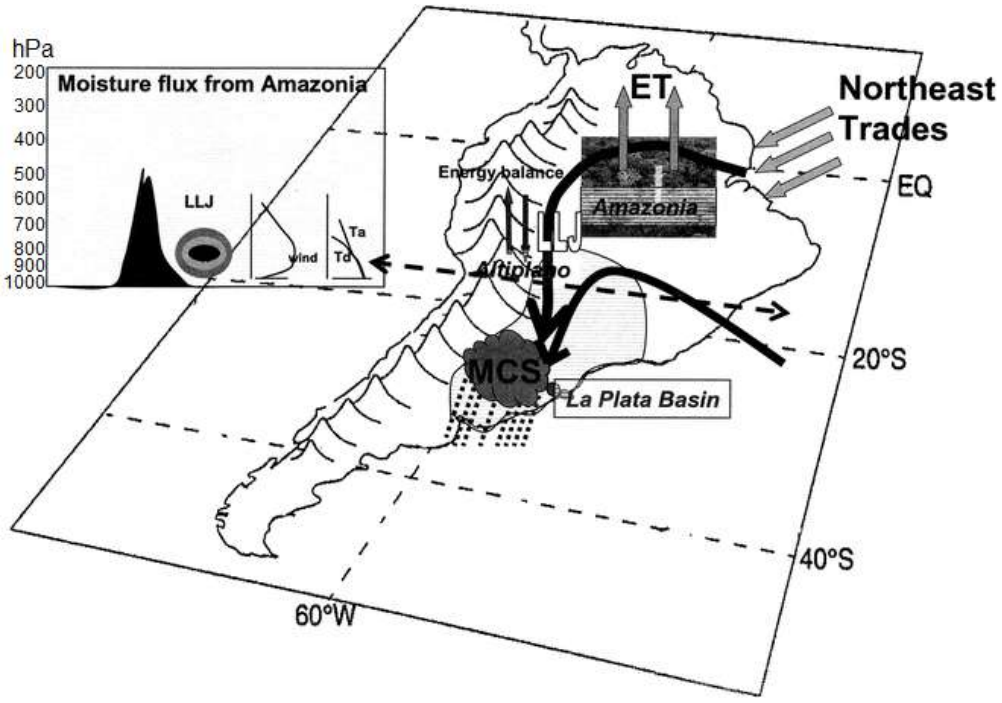

Figure 1.1: Schematic representation of the low-level jets along the eastern flank of the Central Andes. The trade winds transport moisture from the Atlantic Ocean and the surface flow is deflected once it encounters the mountain range. The evapotranspiration above the Amazonia boosts the moisture delivery (Reprinted from Marengo et al., 2004).

of moist air masses in the area results in sharp climatic changes in the temporal and spatial domains that separate the Central Andes in distinct zones (e.g., Brush, 1982; Strecker et al., 2007; Bookhagen and Strecker, 2008; Garreaud et al., 2009). Even though this zonification is aligned with the geomorphology and the elevation, there are still climatic contrasts within similar topography and altitude clusters. For example, the northern part of the Central Andean Plateau, where the Titicaca Lake is found, is more humid than the southern part, characterized by arid zones and salars (Roche et al., 1992; Alonso et al., 2006).

The understanding of those processes involves detailed knowledge of key hydrologic variables. The availability of water in the atmosphere (water vapour) and the soil (soil moisture) are two unknown parameters that play a significant role in the water cycle. The water vapour feeds soil moisture via precipitation, but the relation is not straightforward because the discharge occurs only when certain atmospheric conditions are satisfied (Chahine, 1992; Oki et al., 2004). Dynamic water fluxes are often related to extreme events (e.g. Boers et al., 2014; Poveda et al., 2020). In order to improve the knowledge about this metric, innovative Global Navigational Satellite Systems (GNSS) methodologies can be employed. Although this approach is relatively new, its potential has been shown in several studies (e.g. Larson et al., 2009; Yu et al., 2014; Wickert et al., 2020; Vaquero-Martínez and Antón, 2021; Ramezani Ziarani et al., 2021). The objectives of this study are: (1) the evaluation of the existing GNSS remote sensing techniques for monitoring the hydrological parameters; (2) the improvement of those methodologies to achieve more accurate results for different environmental conditions; and (3) the interpretation of the results for better understanding the dynamics that control local climate.

1.1 Motivation

This research study is part of the International Research Training Group StRATEGy), which consists of projects lead by several institutions from Potsdam, Germany, and Argentina. The area of interest is the South-Central Andes, with the primary focus on climatic and geologic dynamics at various time scales in northwestern Argentina. This study belongs to the work package “Climate-tectonic impacts on surface processes”, and it builds on the project presented in (Ramezani Ziarani, 2020). A subset of the results of this study has already been evaluated in a peer-reviewed journal and published in Antonoglou et al. (2022b).

Motivated by the necessity of predicting intense hydro-meteorological events, this study utilizes state-of-the-art methodologies to monitor the atmosphere. Previous studies have pointed out the relation between heavy precipitation and natural hazards in mountainous environments (e.g., Bookhagen, 2010; Castino et al., 2016, 2020; Jones et al., 2021). The study area lies between the extremely arid Central Andean Plateau, the second-largest orogenic plateau in the world, and the Yungas rainforest in the eastern Cordillera. It extends more than 500 km and 700 km in longitude and latitude, respectively, and the elevation range exceeds the 5000 m. The local economy is based on mining, oil and gas exploitation, agriculture, livestock farming, and tourism. Maintaining the human infrastructure in this area is critical, yet the seasonal South American Monsoon System (SAMS) has a significant influence on it. This results in extended damages owing to the emergence of landslides and floods (Boers et al., 2014; Castino et al., 2016; Poveda et al., 2020). Furthermore, the frequency-magnitude ratio of extreme events has been altered in the past years as a result of global warming. Several studies have depicted the rise of the magnitude against the frequency of the discharge episodes (Boers et al., 2015b; Castino et al., 2017, 2020).

The accurate monitoring of soil moisture and water vapour is a tool of crucial importance for civil protection. The prior is an index that can be used for flood (e.g. Komma et al., 2008; Wanders et al., 2014; Massari et al., 2015) and landslide (e.g. Brocca et al., 2012; Ponziani et al., 2013; Marino et al., 2020) forecasting because it provides information about the saturation state of the soil. On the other hand, the availability of precipitable water in the atmosphere can be used to forecast intense precipitation (e.g. Shi et al., 2014; Priego et al., 2017; Benevides et al., 2019). All this underlines the potential of employing and further developing GNSS remote sensing techniques for monitoring vital hydrological parameters in the Central Andes.

1.2 Methodological Development

GNSS-based remote sensing consists of several independent techniques (Figure 1.2). Ground-based atmospheric sounding was the first methodology established in the 1990s (Bevis et al., 1992). On the contrary, even though the first experiments related to the exploitation of GNSS multipath signals were held during the same period (Martin-Neira, 1993), GNSS Reflectometry (GNSS-R) was later established (Zavorotny et al., 2014). From the methodological point of view, this study aims at improving the existing techniques for the more efficient observation of soil moisture and water vapour.

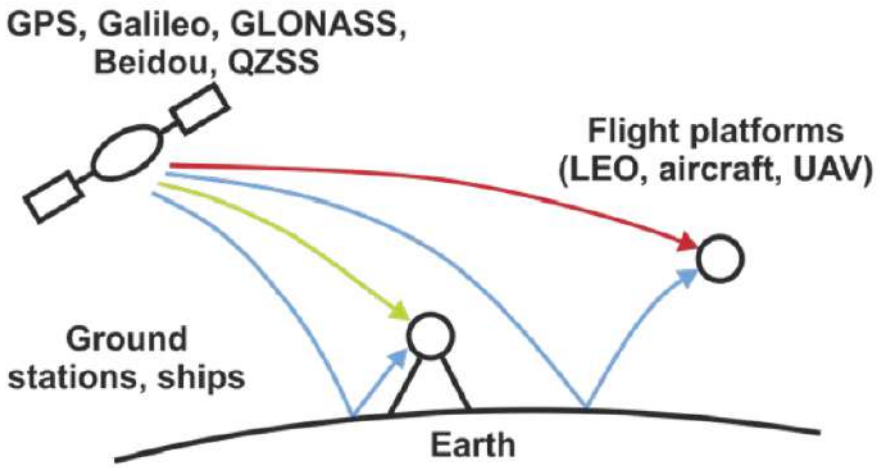

Figure 1.2: Basic concept of observation for GNSS remote-sensing methods. For direct-signal reception, the antenna may be installed on the ground (green), or on an air- or space-borne platform (red). Alternatively, the receiver may record the reflected signal (blue) (Reprinted from Wickert et al., 2020).

Soil-moisture observation with ground-based, single-antenna GNSS multipath belongs to the broad family of GNSS-R techniques that has yet to reach operational applications. The existing approaches only exploit signals from the Global Positioning System (GPS) (e.g. Larson et al., 2008a,b, 2009; Larson and Small, 2013), and there are just a few examples of incorporating different constellations (e.g. Roussel et al., 2016; Yang et al., 2019). This motivates development of a comprehensive system that uses the Global Navigation Satellite System (Globalnaya Navigazionnaya Sputnikovaya Sistema - GLONASS), Galileo, and BeiDou. Because of the different

satellite-position repetition cycle of each constellation, which is translated to temporal resolution, it was impossible to utilize the existing algorithm. Thus it was decided to develop an entirely new application that employs all signals and estimates soil moisture via a least-squares adjustment. This approximation is evaluated using data from two pilot stations in Germany, and it is finally tested in three newly-installed stations in northwestern Argentina.

Ground-based Atmosphere Sounding is a well-established methodology where high-quality commercial and/or research software packages estimate the tropospheric GNSS-signal delays. Therefore, there is little to no room for improvement in that applications. This study focuses on processing the software outputs to gain a better understanding of the atmospheric circulation in northwestern Argentina. While many studies utilize GNSS-derived water-vapour information for weather or climate analysis.

1.3 Thesis Chapters

Chapter 2 delineates the hydrological cycle and explains the mechanisms that dictate the Central-Andean climate.

Chapter 3 gives information about the conventional methods for monitoring the hydrological cycle. It only refers to commonly-used technologies in operational applications.

Chapter 4 describes the basic concept of GNSS remote sensing. It provides general information about the GNSS and all remote-sensing methodologies.

Chapters 5 and 6 are related to the methodological development of GNSS-R techniques for measuring soil moisture and sea level, respectively. Unlike previous versions, this methodology simultaneously exploits all available carrier signals and constellations.

Chapter 7 is related to the evaluation of the developed soil-moisture algorithm in three stations in northwestern Argentina that were specifically installed for this study. The facilities are characterized by different-intensity arid conditions. Chapter 8 is complementary to Chapter 7 and discusses a water-vapour analysis over the same area using a network of 23 stations.

Chapter 9 provides a summary of the experiments and suggests potential applications with operational orientation.

Appendix A includes the photos of the hardware that was employed in the campaign for installing the ground stations in northwestern Argentina.

Appendix B provides information on all time series related to the experiments in Chapter 5.

Chapter 2

The Water Circulation and its Influence on the Central-Andean Climate

Deep knowledge of the hydrological cycle is essential for understanding the processes that dominate the weather and climate. The water circulation within the atmosphere is ruled by some de facto mechanisms. Additionally, there are some climate patterns observed in similar-latitude zones. This chapter focuses on explaining those general global trends and connecting them with the regional climate characteristics of the Central Andes.

2.1 The Hydrological Cycle

Water is the most vital component on Earth for supporting life. Without its presence, it would be impossible for life to develop in the form we know it so far. Water can be found everywhere from the Deep Earth (Ohtani, 2020) to the atmosphere in all three phases; solid, liquid, and gas, and its total amount form the Hydrosphere. Life is based on water's existence, and unlimited mechanisms depend on its biological and physical properties.

The hydrological cycle has a wide range of effects on the climate. It has no origin and end and is a continuous exchange of mass and energy through the Earth's system. Considering the interactive and controversial processes of the hydrological cycle, one can not examine them separately (cf. Figure 2.1). In order to achieve this, several scientific disciplines (e.g. meteorology, oceanography, chemistry, biology, etc.) have to be combined. Understanding the hydrological cycle is based on integrating observations and theoretical models. This coupling is challenging because the hydrological processes take place in different spatial and temporal scales in diverse environments (Chahine, 1992; Oki et al., 2004).

The main stages of the hydrological cycle are evapotranspiration, condensation, precipitation, and run-off. The prior consists of two sub-processes that yield the same result, evaporation and transpiration. Evaporation is when ocean, lake, and stream water turns into vapour (gas) due to heating, while transpiration is when the plants release water in gas form because of oversaturation. Condensation is the transformation of gas water in the atmosphere into liquid water and the subsequent formation of clouds. Precipitation is the release of water from the clouds

through rain, sleet, hail, ice crystals, and snow. Lastly, run-off is the water flow in larger water bodies. This process occurs both on the surface of the Earth and underground.

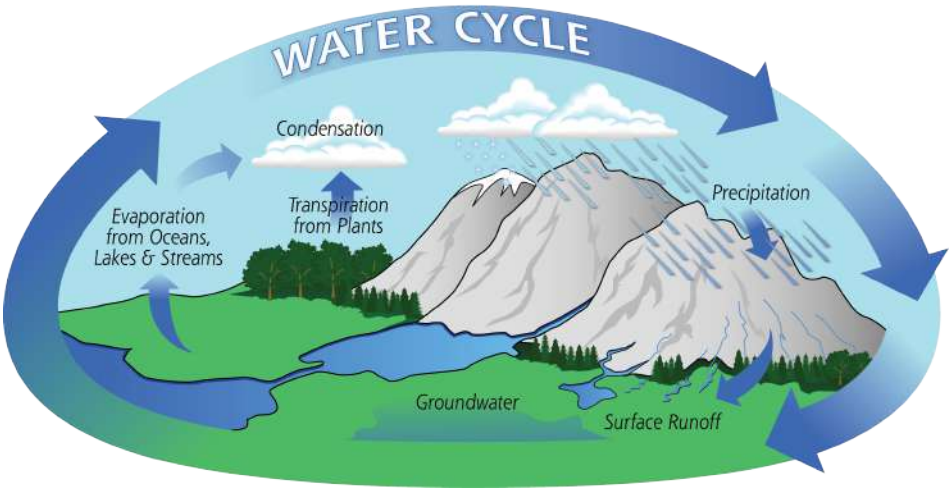

Figure 2.1: Hydrological cycle diagram, showing the water reservoirs and the main mechanisms that are engaged in the circulation (Reprinted from NASA[1]).

According to Anderson (2005), the vast majority of the Hydrosphere consists of water in liquid form. In particular, more than 96.5 % of the world's water is stored in the oceans, and it cannot be directly used because of the concentration of salts. Apart from some minor exceptions, the rest of the liquid water is fresh, and it is used for human activities. In general terms, this form is the least dynamic, and its residence time usually lasts thousands of years. Water in frozen form is the second biggest reservoir in the world. It is essential for the environment and human populations because it dictates the albedo of the Earth, is the most prominent tank of fresh water, and influences the sea-level state; therefore, minor changes would result in chain reactions in the global climate with hazardous effects. Even though there are various exceptions, this reservoir is stable, and its average residency time is several decades. The most steady counterparts are the ice caps in the poles, the glaciers, and the snow accumulated in high altitudes. On the other hand, snow and frozen bodies in lower altitudes and/or mid-latitudes are recycled on a seasonal basis. Finally, water in gas form is the smallest reservoir. Despite this fact, it is very dynamic and plays a significant role in the environment. The troposphere holds 99 % of its mass, but it is not evenly distributed inside this layer. The density of gas water decreases with the altitude and towards the poles.

Form	**Total Volume** (km)	**Share** (%)	**Residence Time**
Oceans	1 338 000 000	96.539	2500 years
Ice and snow	24 364 000	1.757	50 years
Ground water	23 400 000	1.688	1400 years
Lakes	176 400	0.013	5 years
Soil moisture	16 500	0.0012	1 year
Water vapour	12 900	0.0009	8 days

Table 2.1: Water reservoirs and their residence time (Data retrieved from Anderson 2005).

[1]https://gpm.nasa.gov/education/water-cycle. Accessed: 15.11.2021

2.1.1 Water Vapour

Water vapour is characterized by its dynamic nature. Its residence time is up to ten days, which results in a continuous circulation in the atmosphere that transports mass and energy. This behaviour is the main reason that there is no possibility of making accurate long-range weather forecasts. The mechanism that brings water vapour into the atmosphere is evapotranspiration. Its cycle is followed by the formation of clouds via condensation and the release of water from the clouds via precipitation.

The motion of water vapour is very complex because it is subject to a sequence of vertical and horizontal oscillations of the air masses (Figure 2.2). Along the latitude, it circulates the six cells, which occupy almost 30° and are spread from the Equator to the Poles. Those motion patterns are closed wind systems, and they exist both in the northern and the southern Hemisphere. The Hadley cells occur due to the greater solar heating in the equatorial zone (cf. Figure 2.2). This fact forces the air masses to rise, forming a low-pressure environment. The hot air in the troposphere travels towards the poles because of the temperature gradient, but it does not manage to reach them. The air masses start to lose temperature, and they are cool enough to descend at ±30° latitude. This cycle is completed by replacing the rising air at the Equator. The mechanisms that generate the Polar cells are similar. At ±60° latitude, the air gains sufficient heat to start ascending. Consequently, it moves towards the poles due to the temperature difference. This loop is closed by substituting the rising masses. The formation of the Ferrel (Mid-latitude) cells is indirect. In the vertical direction, the air motion coincides with the motion of the neighbouring cells. In the latitudinal direction, the flow is opposite to replace the rising and sinking masses. It is essential to note that there is higher precipitation in the zones of upward motion because the clouds lose their ability to hold moisture when they cool down. Along the longitude, the atmospheric circulation is dictated by the Coriolis effect. The particles moving towards the Equator are deflected westwards, forming the trade wind along the Intertropical Convergence Zone and the polar easterlies. In contrast, the polewards-moving air masses are deflected eastwards. In any case, this overview demonstrates the global trends of the atmospheric circulation. On a local scale, various individual parameters substantially impact the motion of water vapour.

Water vapour is a greenhouse gas that acts similarly to carbon dioxide, methane and nitrous oxide, and it contributes to the global warming by absorbing infrared radiation. It accounts for almost 60 % of the entire greenhouse effect, while the more-criticized carbon dioxide has less than half of this impact (Maurellis and Tennyson, 2003). However, there should be no doubt regarding the negativity of the two compounds because the prior is due to the evolution of the planet Earth, and life is based on it. In contrast, the latter is a product of human activity during the last centuries. With the increase of the Earth's temperature, the capacity of the atmosphere to hold water increases, too. Suppose the Earth system had not developed balancing mechanisms; this could potentially trigger an infinite loop that would lead to a runaway greenhouse effect, similar to what happened in the Venus (Pierrehumbert, 1995; Liu, 2020). An indirect method to quantify the content of water vapour in the atmosphere is the measurement of the tropopause height (Sinha and Harries, 1995; Hu and Vallis, 2019). Recent investigations have shown an increasing trend that contributes to climate variability and, possibly, change (Schmidt et al., 2008; Meng et al., 2021).

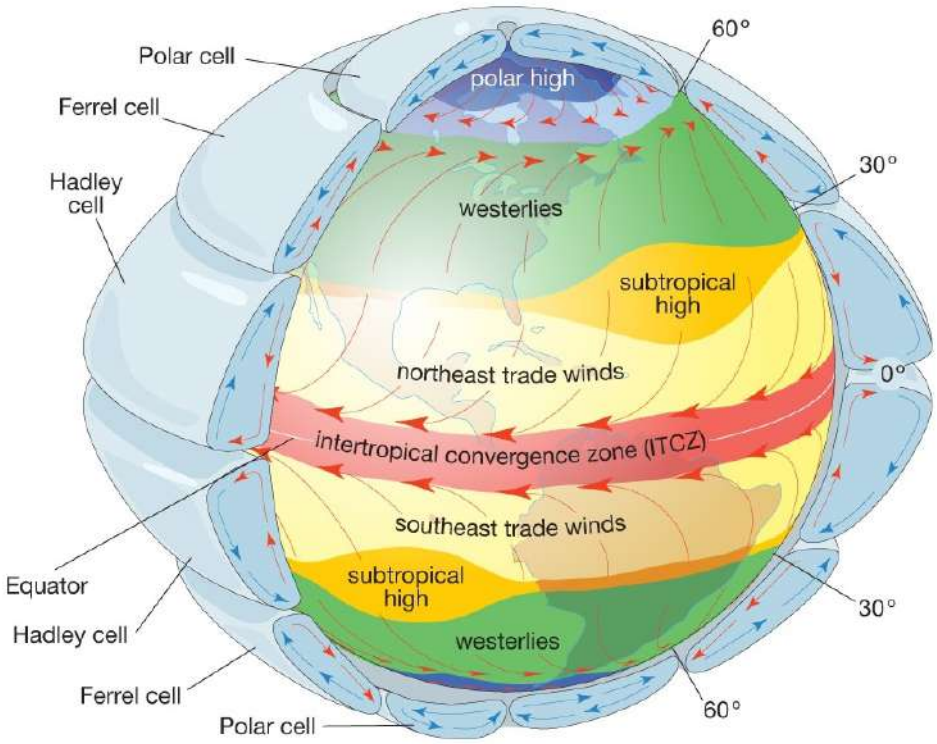

Figure 2.2: Global atmospheric circulation along the latitude and the longitude (Reprinted from Encyclopaedia Britannica[2]).

Water vapour influences the climate in another way; it is a means of latent heat transportation via evaporation and condensation (Chahine, 1992). The storage capacity of water vapour is very high because heating of 1 g of water by 1 K requires 4.18 J of energy. However, the evaporation of the same quantity consumes 2260 J. During the evaporation, thermal energy is absorbed from the surface of the Earth, and it is released via condensation to the clouds (Lange and Speight, 2005; Bengtsson, 2010). This mechanism is critical for the development of life because it decreases the surface temperature and it stabilizes the climate.

2.1.2 Soil Moisture

Soil moisture is the water content of the soil, which originates from the chemically or mechanically weathered bedrock. Additionally, biological weathering is another mechanism that occurs due to the activities of the animals, the plants, the microbes, and it includes both chemical and mechanical processes. Depending on their functionality, the soil profile is separated into various horizons (layers) (Figure 2.3). The topmost is the organic horizon, which mainly consists of partially decomposed plant residues. The second layer is the A horizon, which contains both organic and inorganic material. The subsequent layer is the E horizon, appearing only in well-developed soils. It is made up of mineral deposits but is not rich in organic matter. The B horizon is the underlying layer where all minerals are accumulated. The first three layers structure the

[2]https://www.britannica.com/science/Ferrel-cell#/media/1/204996/107938. Accessed: 17.11.2021

solum, which indicates that they have been subjected to the same soil-forming processes. The C and D horizons are situated beneath, and they consist of lightly-weathered rock. Both layers together form the regolith; the only difference between them is the origin of the material. Lastly, the R horizon is a continuous rock mass on the top of the bedrock that has started to weather. In any case, those rules are general, and they do not always apply (e.g. sand dunes, exposed bedrock, etc.) because soil formation is a slow and continuous process, where the clear separation between the horizons is not achieved instantaneously (Shukla, 2013). It is essential to mention that for the needs of this study, soil moisture is regarded as the water content of only the Organic horizon. This is because the methods used to acquire measurements only in this stratum.

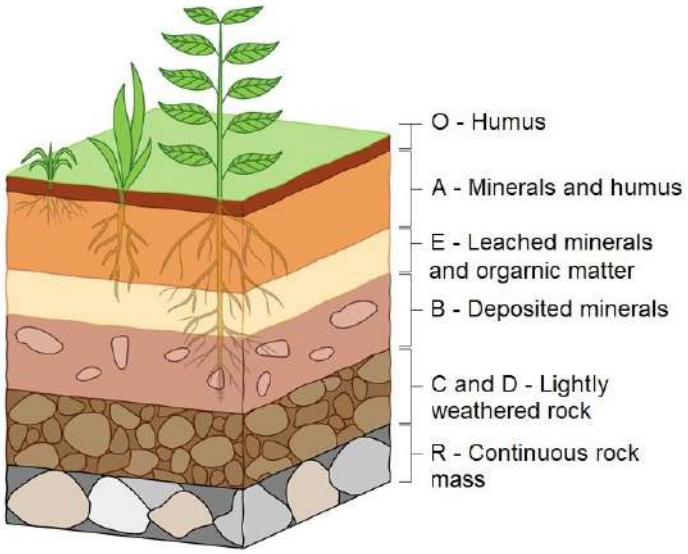

Figure 2.3: Diagram of the soil horizons and their consistency (Reprinted from ScienceFacts[3]).

The state of soil moisture depends on mechanisms of the hydrological cycle, the soil's properties, and the landscape's topography. It is mainly augmented via precipitation, but some secondary processes contribute to this. More specifically, soil moisture can increase via horizontal precipitation (or direct water condensation) and surface run-off. Even though it seems to have an insignificant contribution, it is a crucial source in arid climates (Hildebrandt and Eltahir, 2008; Jia et al., 2019). On the other hand, mechanisms that decrease soil moisture are evaporation and gravity-driven infiltration to lower layers. Moreover, plants absorb water from the soil through their roots to support their functions. In terms of soil properties, the critical factor that regulates soil moisture is porosity. Porous earth is capable of storing water, but when the soil gets saturated, the excess water permeates lower layers. This motion is usually vertical, but the inclination of the surface leads to horizontal flows that create soil moisture inhomogeneities, even in very small areas.

Soil moisture plays a significant role in the climate because it influences the interaction between the surface of the Earth and the atmosphere by regulating the interchange of water and thermal energy. Moreover, soil moisture contributes to decreasing the surface temperature because it is proportional to the albedo. Several studies have shown that the introduction of soil

[3]https://www.sciencefacts.net/soil-horizons.html. Accessed: 18.11.2021

moisture measurements in numerical weather-prediction models remarkably improves their performance (e.g., Drusch, 2007; de Rosnay et al., 2014; Dirmeyer and Halder, 2016). Soil moisture is also a critical factor in agriculture. It is the primary ingredient of growing plants because it dissolves the soil's nutrients, functions as a moisture enhancer, and is the primary component in photosynthesis. The highest normalised difference vegetation index (NDVI) values occur in the zones where water vapour rises and there is high precipitation (cf. Figures 2.2 and 2.4). Additionally, water is involved in both chemical and mechanical weathering processes leading to soil formation. Finally, high soil moisture can trigger landslide events because it alters the stability of the equilibrium of the slopes.

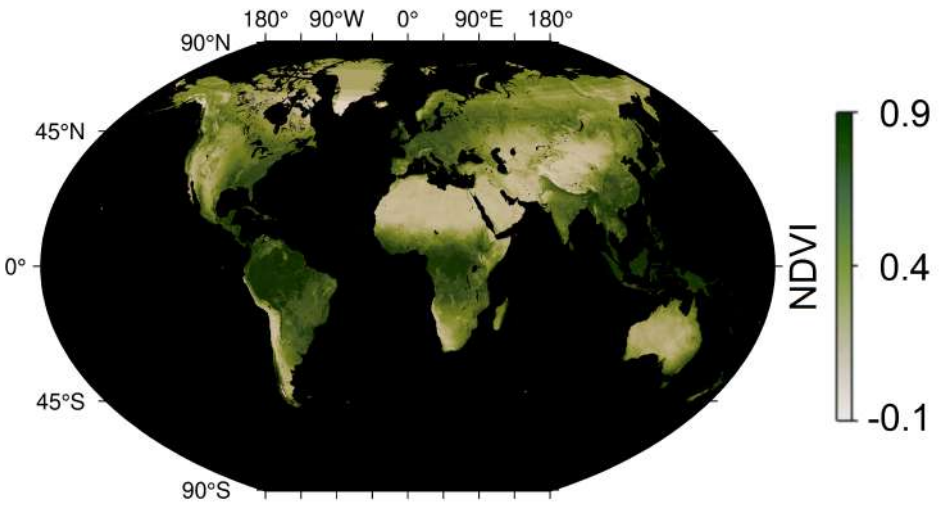

Figure 2.4: World normalised difference vegetation index (NDVI) map for 2020 (Vegetation index information retrieved from Didan 2015).

2.2 The Central-Andean Climate

On a continental scale, the climate of South America is dictated by two key factors, the SAMS and the Andean orographic barrier. The prior is a source of moist air masses near the equator, and the latter triggers forced precipitation on the foothills. This section provides some basic information about the two parameters and focuses on their impact on the climate conditions in northwestern Argentina.

2.2.1 The South American Monsoon System

The monsoon systems are characterized by distinct seasonal low-level wind patterns (or low-level jets - LLJs). They always occur across continent-ocean boundaries in the tropics and cause wet summers and dry winters. This phenomenon takes place because the land has a smaller heat capacity than the water and warms up faster during the spring and summer seasons. Subsequently, the air over the land has a higher temperature than over the ocean. This fact generates a pressure gradient between the continental and the oceanic regions, where the lowest values occur over the land. This process chain results in the transportation of moist masses and the generation of frequent precipitation events over the ground surface. This phenomenon is reversed during the fall and winter seasons because the oceans cool down slower.

Even though the SAMS does not belong among the largest monsoon systems in the world (e.g. the Indian, the East Asian, and the West Sub-Sahara African), it is the most critical climatic impact factor in South America. As mentioned in Silva and Kousky (2012), the circulation of the LLJs is concentrated over the Brazilian Planalto, the origin of the most important rivers of the Amazon, the La Plata, and the São Francisco basins. In those basins, various activities (e.g. agriculture, energy production, logistics, etc.) are crucial for the region's economy. Moreover, the existence of the Amazon rainforest, which has developed because of the enormous water supply, is vital for the entire Earth. It has the richest biome in the world regarding animal species diversity (Turner, 2001), it is estimated to host about 16000 tree species (Ter Steege et al., 2013), and it stabilizes the global climate due to the absorption of carbon dioxide.

Each monsoon system has its features depending on the location, topography, and land-ocean distribution. The facts that characterize the SAMS are the contrast in precipitation between winter and summer and the persistent easterly wind patterns over the northern segment of the continent and the tropical Atlantic throughout the year. In order to clearly observe the inversion of the atmospheric circulation, one has to subtract the annual mean (de Carvalho and Cavalcanti, 2016). In addition, some more features describe the SAMS. As indicated in Silva Dias et al. (1983), an anticyclone in the upper troposphere over the Bolivian Altiplano (Bolivian High) is observed. Marengo et al. (2004) suggests LLJs in the eastern flank of the North-Central and North Andes, and Kodama (1992) and Silva and Kousky (2012) have discussed the South Atlantic Convergence Zone. Lastly, a low-pressure system is found in the borders between Argentina, Bolivia and Paraguay (Chaco Low) (Gandu and Silva Dias, 1998).

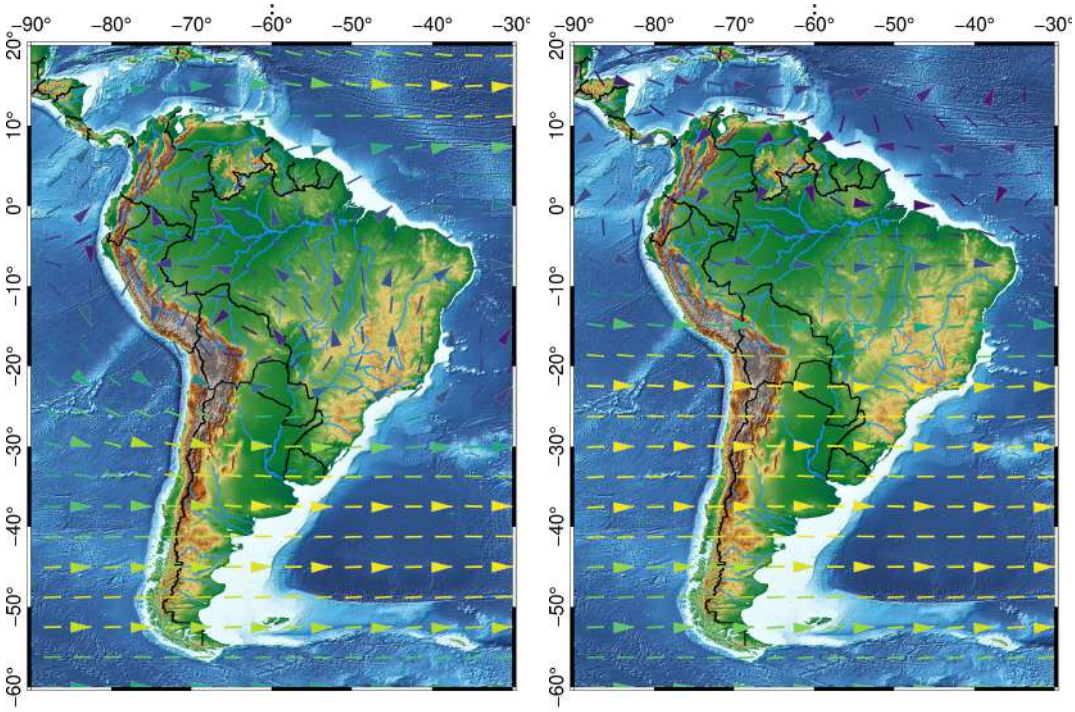

Figure 2.5: cont.

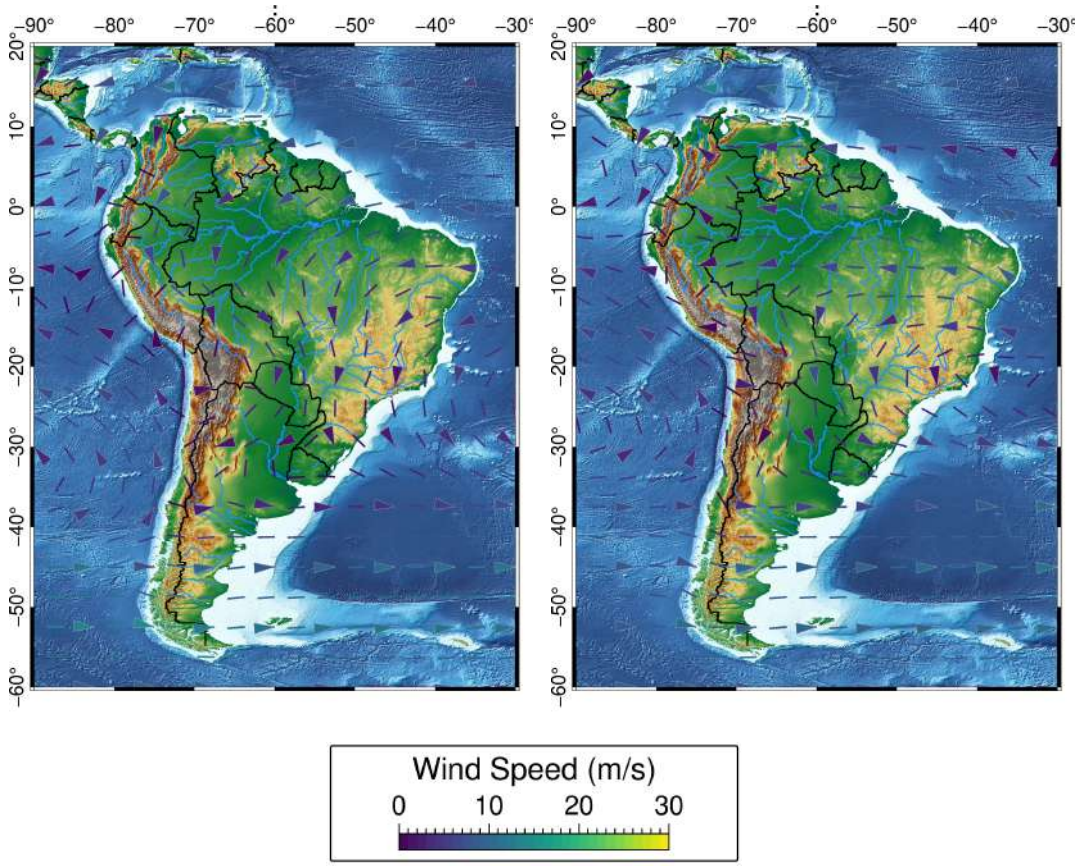

Figure 2.5: Average wind patterns over South America between 1980-2020. The upper pair of maps is referred to the pressure level of 200 hPa, and the lower one is referred to the level of 850 hPa. The left side corresponds to December, January, and February, while the right side corresponds to June, July, and August (Climatological information retrieved from Hersbach et al. 2020, topographic gradient information retrieved from Amante 2009).

2.2.2 Climate Conditions in Northwestern Argentina

Northwestern Argentina belongs to the South-Central Andes. It extends between 22° and 32 °S latitude, and it is made up of the provinces of Jujuy, Salta, Catamarca, Tucumán, Santiago del Estero, and La Rioja. The climate conditions in this area are controlled by the southerly moisture flow from the tropics; the interplay of tropical and subtropical fronts that lead to atmospheric instability; the interaction with polar fronts from the south; and the Andean barrier that causes forced rainfall on the slopes.

The Chaco Low is a low-pressure system on the border between Argentina, Bolivia, and Paraguay. This feature yields a meridional flow of rich-in-moisture air masses from the north through LLJs (Marengo et al., 2004; Montini et al., 2019). However, the LLJs do not take place randomly in time. They are characterized by a diurnal cycle (Salio et al., 2002), and they are more active in summer than in the winter (Seluchi and Marengo, 2000). The seasonal variability occurs due to the SAMS and the pressure gradient between the ocean and the adjacent continent (Vera

et al., 2006; Marengo et al., 2012; Silva and Kousky, 2012). As cited in Alonso et al. (2006), Bianchi and Yañez (1992) suggests that the precipitation in northwestern Argentina during the hot season (austral summer), November-February is four times greater in quantity than the rest of the year. This fact results in distinct wet summers and dry winters (e.g., Castino et al., 2017). Finally, the El Niño Southern Oscillation significantly influences the inter-annual variability of the LLJs (Salio et al., 2002; Vernekar et al., 2003).

Northwestern Argentina is also subject to rainfall events from Mesoscale Convective Systems (MCSs) (e.g., Durkee et al., 2009; Boers et al., 2015a). Additionally, (Salio et al., 2007) shows an interaction between the MCSs and the LLJs during summer, while there is no evidence for connection during fall. Because of the diverse landscape and the atmospheric instability, several severe rainfall events and cloudbursts have occurred. Those events are notable among the continent, and they have led to natural disasters (e.g., Boers et al., 2014, 2015b; Carvalho et al., 2012; Castino et al., 2020). Thus, the MCS's contribution to the area's total rainfall is substantial.

A second parameter that is responsible for the development of cloudbursts is the interaction of the moisture-rich LLJs with cold fronts that originate in the polar region that yield steep temperature drops (e.g., Boers et al., 2015a; Castino et al., 2020). This mechanism is essential for the formation of widespread heavy rainfall, which causes catastrophic floods in the eastern flank of the Central Andes and the corresponding basins. Furthermore, this process often leads to high-magnitude events. A time series analysis between 1979-2016 reveals that 80 % of the 40 most prominent discharge occurrences were linked with the migration of cold air masses (Castino et al., 2020).

The topography of the study area contributes substantially to shaping the climatic conditions. The steep topographic gradient between the low-elevation plains and the Central Andean Plateau, in combination with the excessive moisture in the atmosphere, results in orographic uplift and focused rainfall on the eastern slopes (e.g., Bookhagen and Strecker, 2008, 2012; Ramezani Ziarani et al., 2021). The area is separated into three climate sectors: a low-elevation zone with smooth topography, a high-elevation zone with extended smaller-scale topographic features, and a transition zone with steep slopes (cf. Figure 2.6). This division is in accordance with the topographic and the rainfall gradient Castino et al. (2017). Bookhagen and Strecker (2008) examines the precipitation disparity with satellite data, while Bianchi and Yañez (1992) evaluates it with terrestrial measurements. The latter suggests that the foreland regions receive more than 1500 mm annual precipitation, whereas this scalar reduces to less than 200 mm in the mountainous zone. Furthermore, the orographic uplift takes place in the medium-elevation zone, where the convective cells lose their ability to hold moisture, and they release it through rainfall (e.g., Romatschke and Houze, 2013; Boers et al., 2014; Schumacher et al., 2020). Evidence of the importance role of the Andean orogenesis on the local climate is the discovery of fossils of exotic species, such as Caiman cf. Latirostris, in high-altitude dry areas, where it would be impossible to survive under the current conditions (Bona et al., 2014).

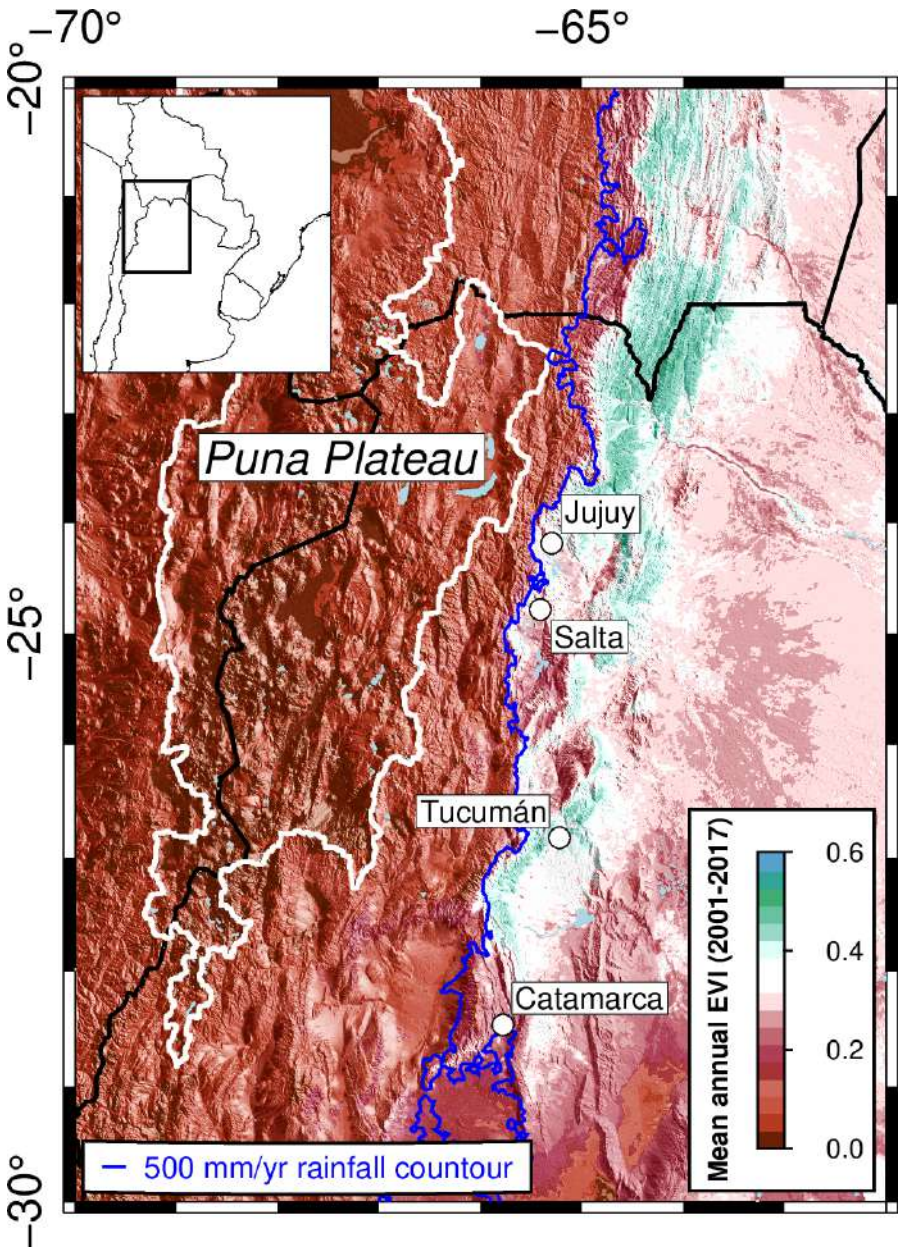

Figure 2.6: Enhanced vegetation index (EVI) information for the study area in the South-Central Andes between 2001-2017. The white line delineates the extremely arid Central Andean Plateau. The blue contour line indicates 500 mm/yr mean rainfall, separating the humid and the semi-arid zones. The white dots show the area's major cities, and the black lines show international borders. (Topographic data obtained from ETOPO1 (Amante, 2009), EVI data obtained from MODIS/Terra (Didan, 2015), rainfall information retrieved from Tropical Rainfall Measuring Mission (TRMM) (2011), as cited in Bookhagen and Strecker (2008)).

Chapter 3

Conventional Techniques for Monitoring the Hydrological Cycle

Over the past few centuries, scientists have invented several experimental and conventional methods to monitor the hydrological cycle. Those techniques differ in spatial and temporal resolution, spatial coverage, and accuracy. Moreover, there are always trade-offs between the first three indices. The subject of this chapter is the operationally-used techniques for measuring water vapour and soil moisture.

3.1 Precipitable Water Vapour

3.1.1 Radiosounding

Radiosounding is a telemetry monitoring method that enables acquiring meteorological variables along the atmosphere. The first attempts of this technique took place in the 19^{th} century when meteographs attached to kites recorded the temperature and the pressure. At the same time, the observations were later recovered on the ground. The biggest challenge was that the kites were anchored to the ground, and it was difficult to handle them in windy situations. In addition, there was no possibility of acquiring observations in high altitudes (Ewen et al., 2008). The most modern ensembles include a radiosonde attached to a weather balloon (Figure 3.1), which may record the position, temperature, pressure, relative humidity, wind speed, and wind direction. The sensors hang several meters below the balloon to prevent erroneous

Figure 3.1: Vaisala RS41 radiosonde (Reprinted from Vaisala[1]).

[1] https://www.vaisala.com/en/products/weather-environmental-sensors/upper-air-radiosondes-rs41. Accessed: 15.09.2022

temperature measurements. Moreover, the observations are transmitted in real-time mode via radio frequency signals, and the radiosondes can typically reach an altitude of 35 km. The quality and the weight of the balloon determine the maximum ascending height. Since the pressure decreases with the altitude, the balloon expands until its skin raptures. At this point, the radiosonde descends safely with a parachute. Depending on the wind speed, a typical trajectory may deviate more than 300 km in the horizontal component; hence the observations are not recorded along the zenith direction. The fundamental advantage of this method is the excellent accuracy and vertical resolution of the measurements. On the other hand, the trade-off is balanced due to the high operational costs and the low horizontal resolution (National Weather Service, 2021). On a global scale, about 1300 terrestrial stations launch radiosondes at least once per day, and approximately 15 ships are equipped with automated shipboard upper-air sounding systems. This high-quality data is exchanged in real-time and utilised in regional and global numerical weather prediction models (World Meteorological Organization, 2021a).

3.1.2 Water Vapour Radiometers

The radiometers are passive remote sensing instruments that measure the emitted thermal energy by bodies. In the case of water vapour estimation, those instruments may be employed in terrestrial as well as in space applications (Figure 3.2). As for the prior, the radiometers utilize the microwave spectrum. More specifically, they are tuned in the K- and the Ka-Band to be sensitive to the water molecules both in vapour and liquid form. The separation of the two forms is achieved because the prior dominates the K-Band, while the latter dominates the Ka one (Morris, 2006). Moreover, water-vapour radiometers are usually installed on rotating mounts and scan the atmosphere by taking measurements along several azimuths and elevation angles. Thus, they provide information about the water vapour in the zenith direction and its gradients. Additionally, they can provide atmospheric profiles similar to the radiosondes (Foth and Pospichal, 2017). Regarding the space applications, the Scanning Multichannel Microwave Radiometer

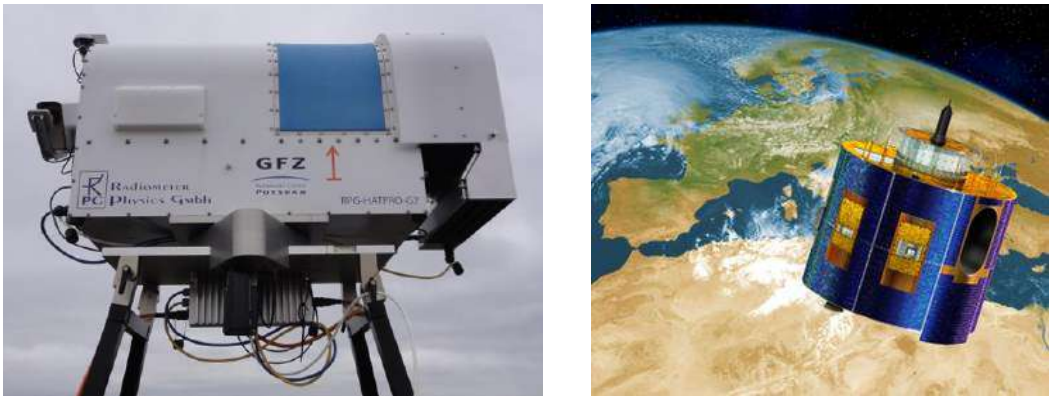

Figure 3.2: **Left:** Ground-based RPG-HATPRO-G2 microwave radiometer (Courtesy of the German Research Centre for Geosciences: Section 1.1[2]) **Right:** Meteosat second-generation satellite, including the Spinning Enhanced Visible Infra-Red Imager (SEVIRI) radiometer (Acquired from ESA[3]).

[2]https://www.gfz-potsdam.de/en/section/space-geodetic-techniques/overview. Accessed: 12.02.2023
[3]https://earth.esa.int/eogateway/missions/meteosat-second-generation/description. Accessed: 12.02.2023

(SMMR) from the National Aeronautics and Space Administration (NASA) operates at five different frequencies, including the K- and Ka-Bands, similar to the terrestrial instruments. It was used in Seasat and Nimbus-7 satellite missions, and it could operate independently of almost all weather conditions (Njoku et al., 1980). A more modern version of space-borne instruments is the infra-red radiometer of Meteosat satellites that were developed by the European Space Agency (ESA). The first generation of this program included seven geostationary satellites that were equipped with the Meteosat Visible and Infra-Red Imager instrument. This device could monitor water vapour via the thermal infra-red channel, centred at around 6.3 μm wavelength. The second generation, which is now operational, consists of four geostationary satellites, which are outfitted with the more-advanced Spinning Enhanced Visible Infra-Red Imager (SEVIRI) radiometer. This sensor is more accurate, and it can acquire observations both at 6 3 and 11 μm wavelengths. In addition, the supplementary low Earth orbit (LEO) ESA-designed Metop satellites are equipped with the Infra-red Atmospheric Sounding Interferometers instrument, which monitors water vapour similarly to the SEVIRI one. Unlike the microwave spectrum, the primary disadvantage of the observations at the infra-red one is their sensitivity in the clouds (World Meteorological Organization, 2021b,c,d). Finally, multiple wavelengths allow separation between the upper and the lower troposphere (Zinner et al., 2008).

3.2 Soil Moisture

3.2.1 The Gravimetric Technique

The gravimetric technique is a low-technology method that is used for the measurement of soil moisture. It is based on extracting soil samples from the area of interest using metal cases of known volume (Figure 3.3). The weight of the soil sample is measured in two phases, immediately upon extraction and after being dried slowly in ovens over a period between 24 and 48 hours. Considering that the sample was unaltered, the mass loss reflects the amount of water that evaporated (Robock et al., 2000). Provided that the density of water is known, the weight difference can be translated into the volumetric water content of the fresh sample. The gravimetric method is straightforward, does not require special equipment, and is very accurate because the measurement is direct. However, possible errors may occur either by not weighing the sample directly after the extraction and letting soil moisture evaporate or by compacting more soil in the metal cassette. In the second case, the porosity would reduce, and the volumetric water content would be biased. The main disadvantages of this method are its extensive use of human resources and its limited spatial representability.

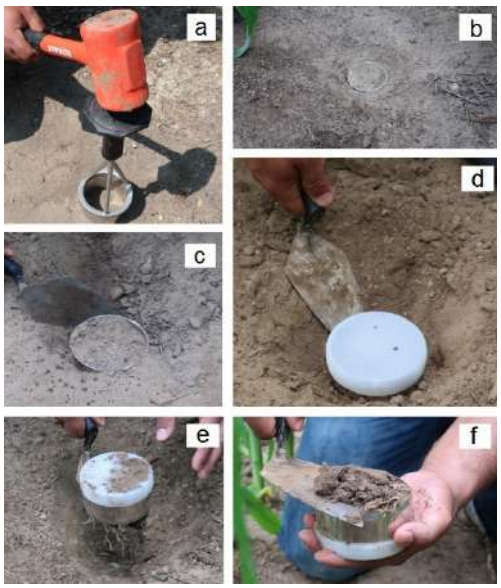

Figure 3.3: Soil-sampling process. A metal case is inserted in the soil, and it is extracted smoothly in order not to destroy the natural structure of the sample. Next, the surface is flattened to align with the ring's lower and upper edges (Reprinted from Shokrana and Ghane 2020).

3.2.2 Time- and Frequency-Domain Reflectometry

Time-Domain Reflectometry (TDR) and Frequency-Domain Reflectometry (FDR) are two methods for measuring soil moisture that require the installation of similar-in-view probes in the ground. Despite certain commonalities, both methods are founded on different principles. TDR estimates the soil's dielectric constant (or permittivity) by measuring the travel time of emitted electromagnetic pulses that propagate through the medium. This technique is considered advantageous because it is highly independent of the soil texture, salinity, and temperature (Rossel et al., 2011). On the other hand, FDR also estimates the dielectric constant, but it is based on the frequency change of the electromagnetic wave that is reflected on the soil. This method is more precise and lower cost, but it requires calibration for different soil types (Veldkamp and O'Brien, 2000). Roth et al. (1990) suggests an equation that additionally requires the permittivity of the water, air, dry soil, and porosity, whereas Topp et al. (1980) proposes an empirical formula that does not require additional information. Lastly, some sensors combine the advantages of TDR and FDR methods merging both technologies (Figure 3.4). This approximation is more efficient, and it can achieve an accuracy of 3 vol % (Truebner GmbH, 2021).

Figure 3.4: Truebner SMT 100 TDR-FDR probe connected with a Campbell CR800 data logger.

3.2.3 Space-borne Soil-Moisture Radiometers

Soil moisture is also measured from passive and active space-borne sensors that are tuned at the microwave spectrum. In the past, it was attempted to estimate this scalar using the visible and the infra-red spectrum, but the results were not always satisfying (Srivastava, 2017). Similarly with water vapour, the first sensor that measured soil moisture was SMMR utilizing observations at the C- and X-Band. NASA's research program continued with the development of the Special Sensor Microwave/Imager and the more-advanced Tropical Rainfall Measuring Mission's Microwave Imager that were tuned at the Ku-

Figure 3.5: SAOCOM satellite (Reprinted from INVAP[4]).

[4]http://saocom.invap.com.ar/. Accessed: 08.12.2021

and X-Band, respectively (Owe et al., 2008; Vrije Universiteit Amsterdam, 2021). The most modern and technologically improved missions are Soil Moisture and Ocean Salinity (SMOS) from the ESA and Soil Moisture Active Passive (SMAP) from NASA. The prior is equipped with the Microwave Imaging Radiometer using an Aperture Synthesis L-Band interferometric spectrometer which is sensitive to moisture levels in the top few-centimetres layer of the soil. Its temporal resolution is less than three days, the measurement accuracy is 4 vol %, and the spatial resolution is 50 km (Kerr et al., 2010). The SMAP mission combines an L-Band radiometer with active radar. Its primary goals are observing soil moisture globally and detecting frozen or thawed land pieces. The measurement accuracy and temporal resolution are similar to SMOS, but the as-designed spatial resolution is a big difference. The radar was incorporated in the instrumentation in order to reduce the spatial resolution from 36 to 9 km (Entekhabi et al., 2010). Unfortunately, the radar failed three months after the mission launch, and the observations were limited to the radiometer. Purely active radars are installed in meteorological satellites (e.g. the Advanced Scatterometer in Metop) or synthetic aperture radar ones. The latter yield very high spatial resolution, but their revisit time is higher. Additionally, most of the sensors operate in the C-Band, the radio waves of which are difficult to penetrate vegetation (Mohanty et al., 2017). The Argentine Microwaves Observation Satellite (Satélite Argentino de Observación con Microondas - SAOCOM, Figure 3.5) (Giraldez, 2003) and the future Tandem-L mission (Moreira et al., 2015) are very promising because they are designed to employ the L-Band, which is less sensitive to vegetation. The combination of two, or more, such constellations would yield a high-quality product with sufficient temporal resolution.

Chapter 4

GNSS Remote Sensing

GNSS was initially designed to serve military applications. Its primary purpose is to provide position, velocity and time information for military applications and, later on, for civilian ones. Access to this data had to be possible anywhere on, or around, the Earth and regardless of weather conditions (Bauer et al., 2006; Hofmann-Wellenhof et al., 2008). In order to achieve high precision, all systematic and random errors need to be isolated (Langley et al., 2017). On the contrary, in GNSS remote-sensing applications, one has to isolate the errors and extract helpful information according to their magnitude and/or behaviour (Jin et al., 2014a,b,c; Yu et al., 2014).

All remote sensing techniques can be either active or passive. The prior are based on their own sources to emit electromagnetic signals at an object, and they measure the backscattered reflection. This concept is advantageous because it does not depend on other -natural- sources and operates autonomously, according to the needs. The drawback is that such systems demand a large amount of energy to operate. On the other hand, passive systems detect backscattered radiation emitted by natural energy sources. This set-up is more straightforward, but the human factor cannot totally control it (Campbell and Wynne, 2011; Khorram et al., 2012).

4.1 Basic Aspects of GNSS

Even though GNSS is treated as one system, it is not fully unified; it is made up of independent counterparts that belong to various organizations and function autonomously. The four main constellations operate globally: Navigation System with Time and Ranging Global Positioning System (NAVSTAR GPS or GPS) - USA, GLONASS - Russian Federation, Galileo - EU and BeiDou - PR China. On the other hand, some regional systems, such as the Quasi-Zenith Satellite System (QZSS) - Japan and the Navigation Indian Constellation (NAVIC) - India (Johnston et al., 2017).

The navigation, independent of the constellation, is based on calculating the distance between the satellite and the receiver by comparing the time of flight and the time of arrival. Provided that the coordinates of the satellites are known anytime, one can calculate the coordinates of the receiver using the trilateration method (cf. Figure 4.1). Since the unknown parameters in the 3D space are three (X, Y, and Z or ϕ, λ, and h), an equal number of synchronous range observations between the satellites and the receiver is sufficient for the calculation of its position. However, strict synchronization cannot be achieved in practice because the transmitters

are equipped with clocks of significantly higher quality than the receivers. As a result, an extra undefined parameter should be introduced into the equation. This unknown is the time correction; therefore, the minimum number of visible satellites must be four rather than three (Fang, 1986; Hofmann-Wellenhof et al., 2008).

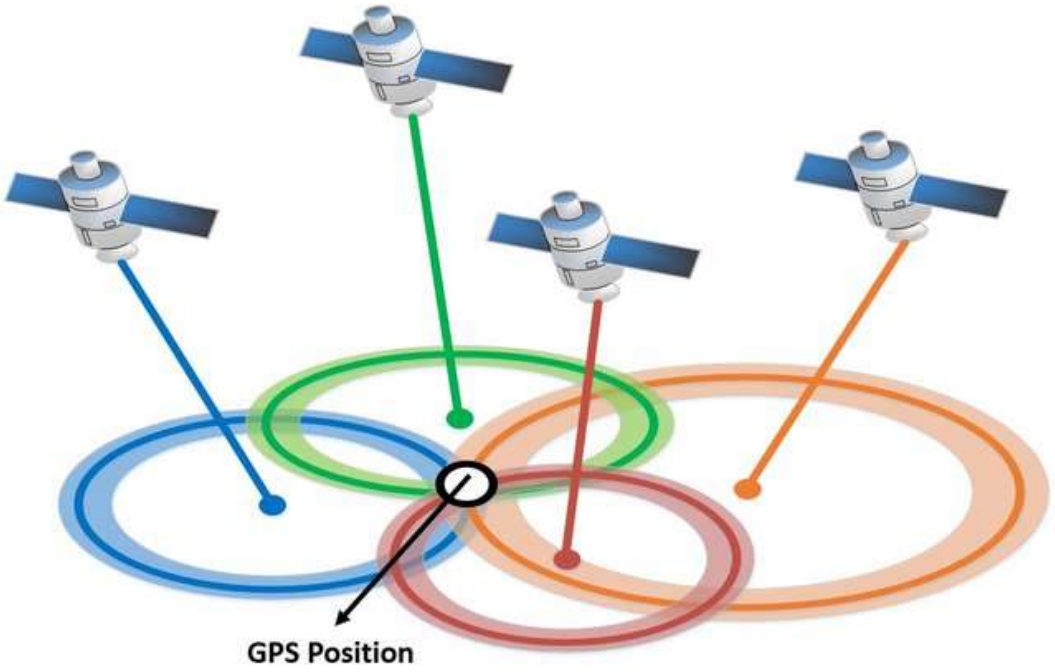

Figure 4.1: GPS satellites trilateration considering only the desynchronization of the clocks (Reprinted from Elazab, 2015).

4.1.1 Segments

Each constellation consists of three major operational components: the space, the control, and the user segment (Figure 4.2). The space segment compromises the active satellites that transmit navigation signals to the users. Provided that each constellation is designed to be functional independently, the satellites are homogeneously distributed to provide position, velocity and time information over the coverage area at any moment. This area is extended over all latitudes, including the poles. The control segment is a network of ground facilities responsible for the system's harmonic function. The most critical counterpart of this segment is the master station which is in charge of the overall operation of the system. More specifically, the orbits and the stabilization parameters of the clocks are calculated and uplinked, along with other commands, to the satellites. Lastly, the user segment includes all equipment that receives and exploits GNSS signals for military and civilian purposes (Hofmann-Wellenhof et al., 2008; Langley et al., 2017). One receiver can be compatible with multiple constellations, but only one is used as the primary. Although GPS dominates the market, there are many cases in Russia and PR China where the primary constellation is either GLONASS or BeiDou (Navipedia, 2018a,c).

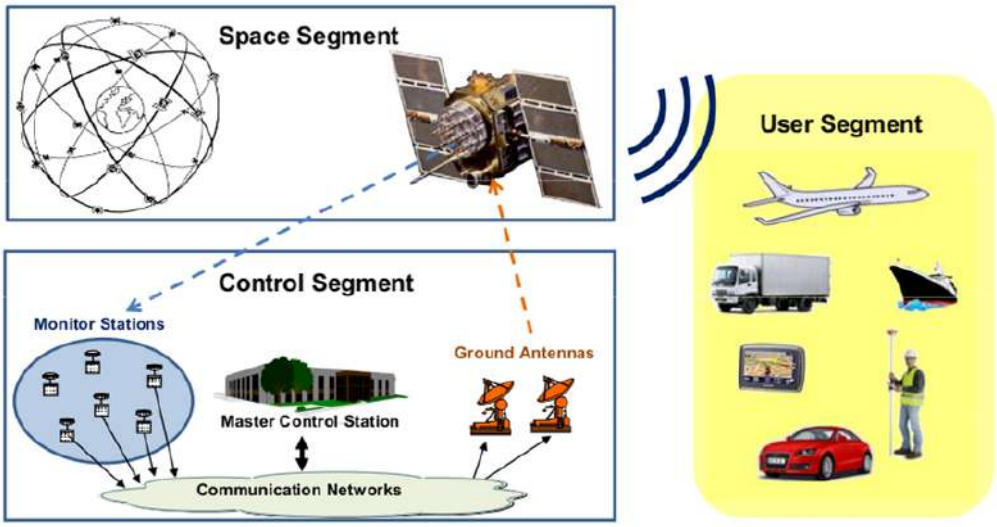

Figure 4.2: GPS segments. The space segment solely broadcasts information to the user segment, but the control and the space segments communicate in two directions (Reprinted from Subirana et al., 2013).

4.1.2 Constellations

GPS

GPS is the first navigation system designed by the U.S. Department of Defense. Its initial goal was to operate only for the military, but later on, it expanded its services to civilian users. The first satellite was launched in 1978, and the system has been fully operational since 1995. During those years, many updates were done in the space segment; the first generation was BLOCK I, and the last was BLOCK IIIA (Figure 4.3). Since GPS started to function completely, 24 satellites have been split into six orbital planes. Each plane has an inclination of 55°; this fact limits the number of visible satellites on the poles without restricting the global coverage. The eccentricity of the orbits is less than 0.02, and the length of the semi-major axis is 26 560 km (or 20 189 km above the Earth's surface), which results in an orbital period of half sidereal day. In the beginning, GPS satellites would broadcast carrier signals in two individual frequencies (L1 - 1575.42 MHz and L2 - 1227.60 MHz). After the launch of the first BLOCK IIF, an additional frequency was introduced (L5 - 1176.45 MHz). The channel access method of GPS is Code Division Multiple Access (CDMA); hence all satellites transmit signals of exactly the same frequencies (Hegarty, 2017; Steigenberger et al., 2020).

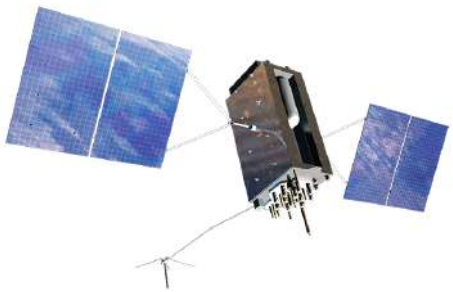

Figure 4.3: GPS BLOCK IIIA satellite (Rendered from Lockheed Martin[1]).

[1] https://www.lockheedmartin.com/en-us/products/gps.html. Accessed: 04.05.2021

GLONASS

The Russian Aerospace Defence Forces are responsible for the operation of GLONASS nowadays, but it was initially designed in the Soviet Union. In the same manner as GPS, the original application of the system was military, but it was later expanded into civil use as well. Although the first launch in 1982 was unsuccessful, the constellation started to develop and became fully operational in 1996. Later on, the system was not sustained due to financial issues, and by 2001, only a few satellites were in orbit (Hofmann-Wellenhof et al., 2008). After the decay period, several launches took place, and the system achieved global coverage in 2011. In GLONASS, 24 satellites are split into three orbital planes. Each plane has an inclination of 64.8°, which increases the number of available satellites in the polar regions with respect to GPS. The semi-major axis has a length of 25 440 km which yields an orbital period of 11 h 15 min 44 s (Navipedia, 2018b; Hofmann-Wellenhof et al., 2008). This constellation was originally using only Frequency Division Multiple Access (FDMA). Each satellite was broadcasting signals of slightly different frequencies. However, the most modern version (GLONASS-K1, Figure 4.4) utilizes both CDMA and FDMA, and they transmit the following carrier signals: L1OC (FDMA - centred at 1602 MHz), L2OC (FDMA - centred at 1246 MHz), and L3OC (CDMA - 1202.025 MHz). In the future, the satellites will additionally use CDMA to broadcast L1OC and L2OC signals (Revnivykh, 2011; Revnivykh et al., 2017; Navipedia, 2018b).

Figure 4.4: GLONASS-K satellite (Rendered from Information Satellite Systems Reshetnev[2]).

Galileo

Galileo is the most modern constellation, and it was developed by the ESA with the funds of the EU. Unlike GPS and GLONASS, the primary use of the system is civilian. The program's evolution consists of three stages; the in-orbit validation, the initial operational capability and the fully operational capability phase (Figure). The first launch was held in 2005 in the Guiana Space Centre, and nowadays, 24 fully functional satellites are orbiting around the Earth with better than expected performance (Navipedia, 2021a). Similar to GPS, the inclination of the orbital planes is 56°, and the length of the semi-major axis is 29 994 km. This altitude results in an orbital period of approximately 14 h (Navipedia, 2020a,c).

Figure 4.5: Galileo full operational capability satellite (Rendered from ESA[3]).

[2]http://www.iss-reshetnev.com/spacecraft/spacecraft-navigation/glonass-k. Accessed: 04.05.2021

[3]https://www.esa.int/Applications/Navigation/Galileo_satellite_recovered_and_transmitting_navigation_signals. Accessed: 05.05.2021

The architecture of the signal plan has many similarities with GPS, CDMA is exclusively used, and the signals are broadcast in three frequencies; E1 (1575.42 MHz), E6 (1278.75 MHz) and E5 (1176.45 MHz) (Navipedia, 2020b).

BeiDou

BeiDou-2 is the second-generation satellite navigation system of PR China. The first generation was BeiDou-1, and it provided its services regionally. The first launch was held in 2000, and the system stopped its operations in 2012. The system's set-up was exceptional because one needed observations of only two satellites to achieve a positioning solution. This was possible because there was two-way communication between the control station, the satellites and the receiver, and the clock errors were eliminated. Additionally, the system used a digital elevation model to eliminate one unknown parameter and convert a 3D geometrical problem to a 2D one. The drawbacks of this concept are the necessity of uninterrupted estimation of the control's centre and the satellites' positions and the accuracy reduction due to the low spatial resolution of the elevation model (Hofmann-Wellenhof et al., 2008).

Figure 4.6: BeiDou-3 satellite (Rendered from Shanghai Engineering Center for Microsatellites[4]).

BeiDou-2 is a global satellite navigation system whose architecture approximates the structure of other global constellations. The first satellite was launched in 2007, and after a series of successful operations, the system was fully functional in 2020. The extension of this system is BeiDou-3 (Figure 4.6), and it started to develop in 2015. The difference between BeiDou and the other constellations is that the prior does not use only medium Earth orbit (MEO) satellites, but also geostationary and inclined geosynchronous ones. In fact, five geostationary, three inclined geosynchronous, and 27 MEO satellites comprise the constellation. The inclination of the MEOs is 55°, and they are split into three orbital planes. The system uses CDMA exclusively, and after the new developments, it broadcasts the signal in five carrier frequencies: B1C (1575.42 MHz), B1I (1561.098 MHz), B2I (1207.140 MHz), B2a (1176.45 MHz) and B3I (1268.52 MHz) (Yang et al., 2017; China Satellite Navigation Office, 2019; Lu et al., 2020).

Other Regional Constellations

The QZSS (Figure 4.7 - left) is the satellite navigation system of Japan, and it covers the entire territory of the country. This constellation provides corrections to the signals of other GNSS, and it does not operate autonomously. More precisely, it is compatible with L1, L2, and L5 signals from GPS and with E6 from Galileo. The QZSS consists of one geostationary and three inclined geosynchronous satellites. This set-up allows observation of at least one satellite in elevation angle over 70° anytime and anywhere in Japan (Navipedia, 2018d). This augments navigation in areas with poor sky visibility, such as deep canyons.

The NAVIC, formerly known as Indian Regional Navigational Satellite System (IRNSS, Figure

[4]http://english.microsate.cas.cn. Accessed: 24.07.2022

4.7 - right), is India's regional satellite navigation system that covers the country's wider territory. The constellation consists of seven satellites, three geostationary and four inclined geosynchronous. The first launch was held in 2013, and the last satellite was set into orbit in 2016. The system broadcasts signals in two frequencies; L5 (1176.45 MHz) and S-band (2492.08 MHz), a fact that makes it unique because all other constellations exclusively utilize the L-Band (Navipedia, 2021b). The advantage of this setup is the reduction of the interference effects on GNSS signals (Sun et al., 2017).

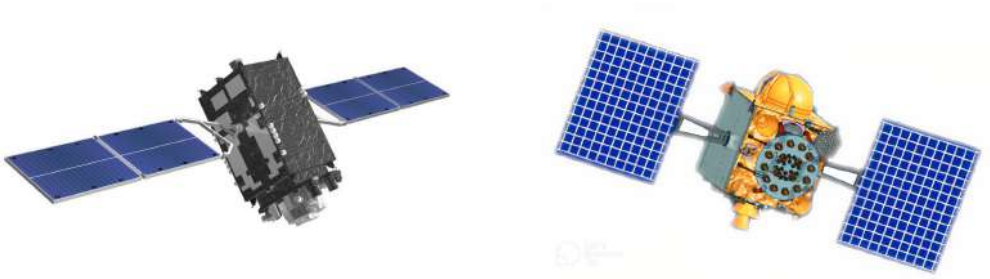

Figure 4.7: **Left:** QZSS satellite (Reprinted from Cabinet Office, Government Of Japan[5]). **Right:** IRNSS-1A satellite (Rendered from Indian Space Research Organisation[6]).

4.1.3 Signals and Multiplexing Techniques

Carrier Signal

The most important components of each navigation satellite are its atomic oscillators which operate at a fundamental frequency (f_0). For GPS, Galileo, and BeiDou this frequency equals 10.23 MHz, while for GLONASS it is 5.11 MHz (Ellingson et al., 2000; Hein et al., 2001; Qin et al., 2019). The carrier signal is generated by scaling the fundamental frequency. The satellites of all constellations that use CDMA transmit their carrier signals on the same frequencies. On the other hand, each GLONASS satellite, which uses mainly FDMA, utilizes slightly different frequencies to distinguish. Finally, each satellite uses at least two frequencies to eliminate the ionospheric error (Hofmann-Wellenhof et al., 2008).

Ranging Code

The ranging code is a chain of alternating bits (chips) superimposed in the carrier signal. This sequence of zeros and ones is also called pseudo-random noise (PRN). The term "random" is used because the PRNs seem arbitrary, but they are generated with an algorithm. On condition that CDMA is utilized, each PRN is unique for every satellite and is used for identification. The ranging code is realized by shifting the initial phase of the carrier signal, and the ranges are easily measured by cross-correlating the replica of the code that is stored in the receiver with the recorded signal. There are always up to two PRNs in each signal, the primary and the secondary. In GPS, the prior is the Precise code (P-code), and the latter is the Coarse-Acquisition (C/A) one (Figure 4.8). Even though the secondary code is not very accurate, it is very useful because it allows fast identification of the satellites in view and acceleration of the cross-correlation process with the P-code. Thus there is no necessity to include the secondary code in all signals

[5]https://qzss.go.jp/en/technical/qzssinfo/index.html. Accessed: 06.05.2021
[6]https://www.isro.gov.in. Accessed: 06.05.2021

of one constellation but in a fraction of them. Lastly, the ranging code is characterized by its orthogonality which means that it always yields a high correlation between a single-code replica and a bundle of received signals (Hofmann-Wellenhof et al., 2008; Gebre-Egziabher and Gleason, 2009).

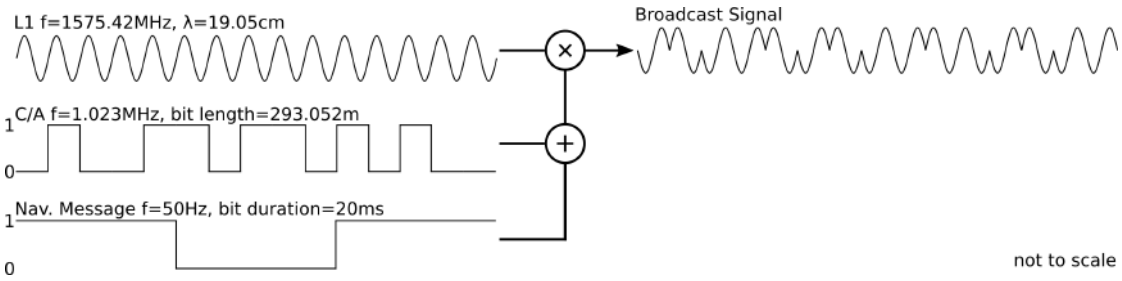

Figure 4.8: Main components of GPS L1 Coarse-Acquisition (C/A) signal.

Navigation Message

Similarly to the ranging code, the navigation message is also superimposed in the carrier signal. This message characterizes each satellite and is implemented to provide orbital and clock corrections information in real-time mode mainly. Even though these data are not highly accurate, they are sufficient for two-three centimetre-level positioning applications. Additionally, the navigation message provides information about the troposphere, the ionosphere, the status of the satellite and the orbits of further satellites of the constellation. The last one is called almanac, and it is used for the recognition of the satellites in view and the prompt position estimation. The navigation message in GPS contains 25 pages. Considering that each page consists of 1500 bits, and the transmission rate is 50 bits/s, the repetition period of the message is 12.5 min (Hofmann-Wellenhof et al., 2008).

Signal Multiplexing

Each signal is designed to include either one or two ranging codes. In the first case, the set-up is simple, while in the second case, both ranging codes are incorporated using a modulation method. The most traditional technique is binary phase-shift keying, and the first generations of GPS and GLONASS use it. However, a more modern and efficient approximation is binary offset carrier modulation, and the later generations of the GNSS utilize it. This transition was primarily done because the spectral efficiency of binary offset carrier allows for inter-constellation compatibility (Falcone et al., 2017; Hegarty, 2017; Revnivykh et al., 2017; Yang et al., 2017). Other advantages of this modulation are the augmentation of signal tracking and multipath mitigation capability (Juang et al., 2020).

4.1.4 Observables

The observables used mainly in geodetic applications are the pseudo-ranges and the carrier phases. In addition, auxiliary information is obtained by analysing the Doppler shift and the signal strength. Each manufacturer of GNSS receivers has its own configuration to export the observations. Nevertheless, all format types can be converted into Receiver Independent Exchange (RINEX) files (Gurtner and Lou, 2018), a format which is commonly accepted by the GNSS community.

Pseudo-ranges

The pseudo-ranges are directly associated with the ranging codes. They are calculated by measuring the travelling time of the signal Δt between the transmitter and the receiver, and as explained previously, this is achieved with cross-correlation. The accuracy of the correlation depends on the chip duration. In the case of the P-code, this is almost 1 µs, while in the C/A code, this is ten times longer. Provided that the instrumental noise of the receiver (or receiver noise) is 1 % of the chip duration (Rankin, 1994; Krawinkel and Schön, 2016), the resulting error is 29.3 cm and 2.93 m, respectively. Additionally, the term "pseudo" is used because the transmitter and receiver clocks are not totally synchronized, and the measured range is highly biased. Unlike correlation accuracy, this uncertainty can be eliminated. The main disadvantage of the P-code is that it is not fully available to civilian users. When anti-spoofing mode is enabled, the secret W-code is mixed with the P-code yielding to the broadcasted Y-code (Hofmann-Wellenhof et al., 2008). Because W-code has a 20 times lower frequency than the P-code, there are techniques to omit it, but the pay-off is higher instrumental noise. Finally, when both primary and secondary codes are available, the provided observation is always the primary one (Woo, 2000). Although there are many versions of the mathematical model of the P-code observations (e.g., Xu and Xu, 2016; Langley et al., 2017; Navipedia, 2020d), a generalized form of this formula between a satellite s and a receiver r is:

$$P_r^s = \rho_r^s + (u_r - u^s)c + I_r^s + Z_r^s + \beta_r - \beta^s + \epsilon_P \tag{4.1}$$

where:

ρ	geometric distance
u	clock corrections
c	the speed of light
I	ionospheric delay
Z	tropospheric delay
β	hardware delays
ϵ_P	instrumental noise

Carrier Phases

The carrier phases are measured after restoring the phase shifts of the carrier signal. Since the receiver cannot count the full signal cycles between the satellite and the antenna, an uncertainty called initial-phase ambiguity (or ambiguity) is inserted. This is estimated by integrating the phase changes over two, or usually more, epochs (Hofmann-Wellenhof et al., 2008). On the other hand, the phase measurements of the last incomplete cycle at a certain epoch and the relative changes between two epochs are more accurate because the quality of the observations depends on the instrumental noise, which is related to the wavelength of the signal (Rankin, 1994). The carrier signals have short wavelengths between 19 and 25 cm, while the chip length of P-code is 29.3 cm. Similarly with the previous equation, there are several variants of the mathematical model of the carrier observations (e.g., Langley et al., 2017; Navipedia, 2020d). A generalized form of this observable is:

$$L_r^s = \rho_r^s + (u_r - u^s)c - I_r^s + Z_r^s + \lambda(N_r^s + \alpha_r - \alpha^s) + \epsilon_\Phi \tag{4.2}$$

where:

λ	wavelength
N	ambiguity
α	hardware delays
ϵ_Φ	instrumental noise

The most notable distinction between Equations 4.1 and 4.2 is the absence of the ambiguity. Additionally, the ionospheric delay has an equal magnitude but opposite sign. This occurs because the carrier signal propagates with its natural phase velocity, and the pseudo-ranges propagate with the group velocity (Figure 4.9). In non-dispersive media (e.g. troposphere), both velocities have the same magnitude, while in dispersive ones (e.g. ionosphere), one can assume that the phase delay has the same magnitude, but an opposite sign of the group delay (Meurer and Antreich, 2017).

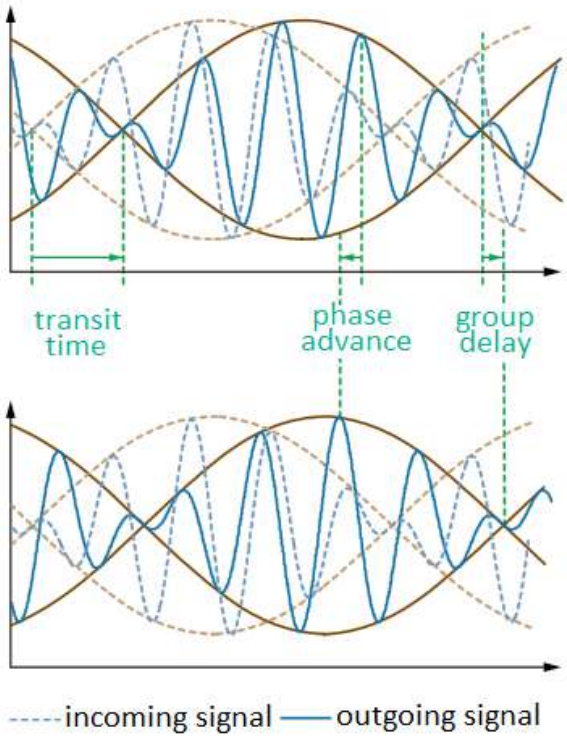

Figure 4.9: Propagation of a modulated signal in a non-dispersive (top) and a dispersive (bottom) medium (Rendered from Meurer and Antreich, 2017).

Doppler Shift

The Doppler effect occurs due to the relative motion between the transmitter and the receiver. Due to this effect, the receivers on the Earth record different frequency waves than the transmitted ones. In GNSS, this variation can be $\pm 5\,\text{kHz}$ in static mode, and it can be greater if the receiver is in motion (Zhang et al., 2017). Each GPS receiver calculates its velocity at every epoch, and according to security regulations, it stops operating after exceeding the limit of 1000 kn (Stansbury et al., 2013). As mentioned in Xu and Xu (2016), the mathematical model of the Doppler shift between a satellite s and a receiver r for the carrier phases is:

$$D_r^s = \frac{d\rho_r^s}{\lambda dt} - f\frac{d(u_r - u^s)}{dt} + \epsilon_\Phi \tag{4.3}$$

where:
ρ geometric distance
λ wavelength
f frequency
u clock corrections
ϵ_Φ instrumental noise

Signal Strength

The signal strength provides information about the reliability of the signal, and the measure is the ratio between its theoretical power and its noise level. All satellites yield stronger signals when they are directed in the zenith direction with respect to the receiving antenna. This is due to the minimization of the signal propagation distance. There are two measures for the signal strength, the signal-to-noise ratio (SNR) and the carrier-to-noise density (C/N_0), while the measurement provided by the RINEX files is always the C/N_0 (Gurtner and Lou, 2018). As given in INSIDE GNSS (2010), the mathematical models of the signal strength are:

$$SNR\,(\mathrm{dB}) = S - N \tag{4.4}$$

$$C/N_0\,(\mathrm{dB-Hz}) = C - N_0 \tag{4.5}$$

where:
S signal power in dB W
N noise power in dB W
C carrier power in dB W
N_0 noise power density in dBW − Hz

4.1.5 Error Sources in the Observations

The errors that are included in the observations can be either systematic (biases) or random, and they are separated into three main categories; the errors related to the satellites, the receivers, and the propagation of the signal.

Errors Related to the GNSS Satellites

Two error sources are associated with the satellites, the orbital and the satellites' clock error, and they include both systematic and random components (Yunck et al., 1996; Griffiths and Ray, 2009; Beard and Senior, 2017).

The orbital error occurs due to the inaccurate calculation of the satellites' position. As mentioned in Section 4.1.1, the control segment is responsible for estimating the orbital parameters of the satellites, which are uploaded several times per day to keep the accuracy below the sub-meter level. In post-processing mode, there is the possibility to achieve significantly better accuracy that approximates the 5 cm error (Johnston et al., 2017; Langley et al., 2017). For differential GNSS applications in real-time mode, the information obtained from the navigation message is sufficient because two or more stations are utilized, and the error is differentiated and minimized. On the other hand, in high-precision single-station applications, such as Precise Point Positioning, accurate orbits are necessary. Lastly, in the recent years, several developments have been made for the accurate prediction of the position of the satellites (e.g., Yang and Gao, 2017).

All GNSS satellites are equipped with high-quality atomic clocks, which are used to record

the time of transmission of the signal from the satellite to the receiver. Similar to the orbits, the atomic clocks are coordinated by the control segment. Each constellation has a master clock, according to which all satellites are synchronized. Additionally, since every navigation system operates independently, intra-constellation compatibility requires strict synchronization between all master clocks. The error of the GPS satellites is typically 0.1-0.2 ns, which leads to a range miscalculation of 3-6 cm (Zhang et al., 2011). Likewise the orbits, the clock errors are minimized either by differentiating synchronous observations that contain the same bias or by predicting the clocks' drift.

Errors Related to the Receivers

There are three error sources associated with the receivers, the clock error of the receiver, the instrumental noise, and the error from the estimation of the antenna phase centre. The nature of the prior is both random and systematic (Krawinkel and Schön, 2016), but some publications consider it only systematic (Yeh et al., 2009). The second error source is random (Hauschild, 2017a), while the third is systematic (Schmid et al., 2016).

The clock errors of the receivers are identical in nature to those of the satellites, but they differ in magnitude. This occurs because the receivers are usually equipped with quartz oscillators and not with atomic ones, which are significantly higher quality. In fact, it would be impossible to equip every receiver with an atomic clock due to budget reasons. Each receiver adjusts its time constantly, but the drift rate is too high to keep it stable. Even after synchronization, a realistic value for the clock error is 200 ns (Krawinkel and Schön, 2016), which leads to a range inaccuracy of 60 m. Finally, this bias is either resolved with differentiation or is estimated as an unknown parameter (Langley et al., 2017).

The instrumental noise occurs due to the imperfect correlation of the recorded modulated signal. This error is expected because all GNSS receivers consist of analogue circuits with limited functional capabilities (Hauschild, 2017a). As explained in Section 4.1.4, the magnitude of this error is typically 1 % of the correlator width and is considered as Gaussian white noise (Rankin, 1994; Krawinkel and Schön, 2016). Lastly, it is essential to mention that this error level refers to the raw measurements; in linear combinations, the noise increases according to the propagation of uncertainty (Hauschild, 2017b).

The antenna-phase-centre-uncertainty is different for each carrier frequency (Maqsood et al., 2017). Additionally, the position of the phase centres changes slightly depending on the elevation angle and the azimuth. Those changes are at the millimetre level and are required only for high-precision applications (Wübbena et al., 2006). The antenna calibration can be either relative or absolute. In the first case, the corrections are determined with respect to an other calibrated antenna (e.g., Mader, 1999; Wübbena et al., 2006). In the second case, the corrections are determined by transmitting signals to the antenna from known locations (e.g., Görres et al., 2006). Moreover, in network solutions, the errors are minimized if all receivers are equipped with the same antenna model and all antennas are oriented to the same direction (Commins and Janssen, 2012).

Errors Related to the Propagation of the Signal

The GNSS signals are electromagnetic waves propagating through different media; hence, they are expected to experience delays due to refraction. The media that alter the velocity of the

signal are the neutral atmosphere and the ionosphere. Even though the magnitude of those delays changes dynamically, there are regarded as systematic errors because they consistently alter the measurements in the same direction. Furthermore, the antenna does not receive only direct signals but reflected ones too. This phaenomenon is called the multipath effect, and its nature is also systematic (Wübbena et al., 2010; Braasch, 2017).

The neutral atmosphere consists of the gases and particles which surround the Earth. It is formed by four sublayers, the troposphere (0-10 km), the stratosphere (10-50 km), the mesosphere (50-85 km), and the thermosphere (85-500 km) (Figure 4.10). The vast majority of the meteorological events take place in the troposphere because this layer holds 75 %-80 % of the atmospheric mass and 99 % of the water vapour and aerosols; hence the delay occurred due to the Earth's neutral atmosphere is often called tropospheric delay. Moreover, the air density is minimal in the thermosphere, and this layer is treated as a part of the outer space (UCAR, 2011, 2015). This error is independent of the frequency for L-band signals, and consequently, it cannot

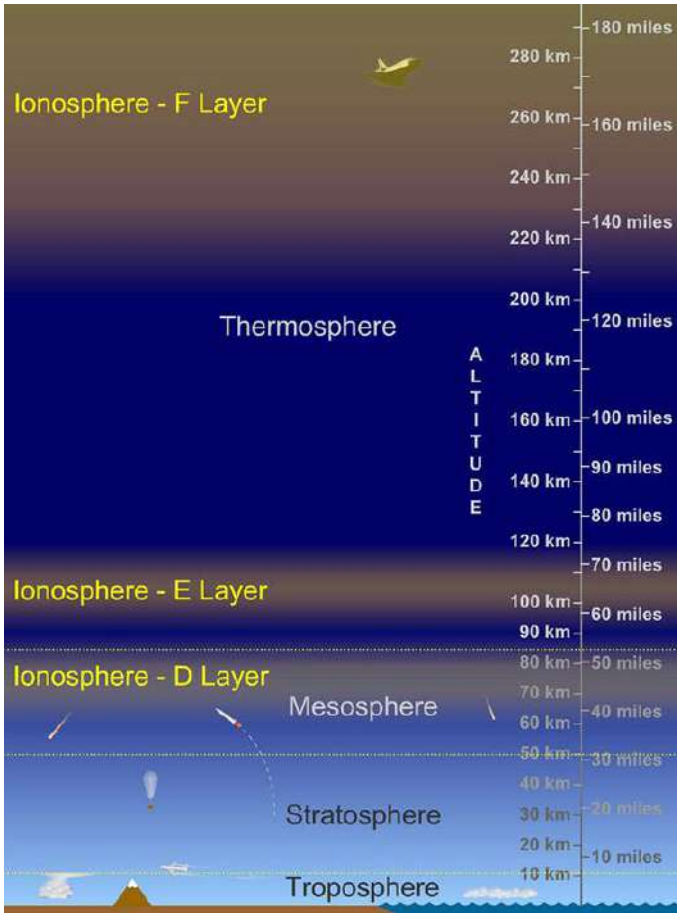

Figure 4.10: Schematic presentation of the layers of the neutral atmosphere and the ionosphere (Reprinted from University Corporation for Atmospheric Research[7]).

[7]https://scied.ucar.edu/learning-zone/atmosphere/ionosphere. Accessed: 02.08.2022

be determined from measurements with dual-frequency receivers (Hobiger and Jakowski, 2017). In differential GNSS applications, where the distance between the stations is short, the error is regarded as equal and minimized through differentiation (Hauschild, 2017b). In other cases, the error is either estimated as an unknown parameter or calculated from numerical weather prediction or reanalysis data. Moreover, it is possible to combine both techniques mentioned above (Yang and Gao, 2017; Yang et al., 2020).

The ionosphere consists of charged particles (ions); it starts in the upper atmosphere and can reach up to the height of 1000 km above the Earth's surface (Hobiger and Jakowski, 2017). Its thickness changes dynamically, and it depends on the Earth's rotation and solar activity, which occurs at an 11-year cycle (Hathaway, 2015). The ionosphere is formed by three main layers; the D-layer (60-90 km), the E-layer (90-150 km), and the F-layer (150-500 km) (Figure 4.10). The heights mentioned above are not fixed, and they can change significantly. During the day, the F-layer is split into two counterparts, and the D-layer is heavily ionized. During the night, the F-layer is unified, and the D-layer vanishes (UCAR, 2014). Unlike the atmosphere, the ionospheric error depends on the frequency of the carrier signal, and it can be estimated by combining two or more frequencies. Two signals are sufficient for calculating the first-order ionospheric effect, which is usually enough to achieve high accuracy. In the case of too high ionization, a third frequency has to be introduced to calculate the second-order ionospheric effect. The disadvantage of this approximation is the increase of the noise (Liu et al., 2016; Hobiger and Jakowski, 2017). On condition that a multi-frequency receiver is not available, the ionospheric error can be minimized in a network solution by differentiating synchronous observations of nearby stations (Hauschild, 2017b).

The multipath effect is caused by the interference between the direct and the reflected signal. It only depends on the position of the obstacles around the antenna and can affect both the pseudo-ranges and the carrier phases. In kinematic mode, the reflection points are irregular, and the effect is difficult to model. In static mode, if the station's vicinity does not change, the antenna receives the same reflections every time a satellite repeats its orbit. In this case, the multipath can be easier mitigated. The simplest way to minimize this error is the proper position of the antenna away from obstacles. Additionally, it can be reduced with mechanical means and/or software tools. For example, choke-ring antennas block the reflected signals, and special software packages detect the interferences using SNR measurements (Braasch, 2017).

4.2 GNSS Remote-Sensing Techniques

Taking advantage of the global coverage and the accessibility of the GNSS, it was first proposed in the 1990s to expand the use of navigation systems and exploit the L-band signals for remote sensing applications. Over the last decades, this concept has been broadly investigated and has been established as a reliable methodology (Jin et al., 2014a,b,c; Yu et al., 2014). There are three basic categories for the GNSS remote-sensing techniques: Space-based Atmosphere Sounding (Kursinski, 1997; Hajj et al., 2002); Ground-based Atmosphere Sounding (Bevis et al., 1992); and GNSS-R (Zavorotny et al., 2014). The first two focus on the propagation of the signal through the atmosphere and the ionosphere, while the latter examines the impact of the signal reflections.

4.2.1 Space-Based Atmosphere Sounding

Space-based Atmosphere Sounding (or GNSS Radio Occultation - RO) is a technique based on observing GNSS measurements from an LEO satellite. The critical times are the rise and the set of the LEO with respect to the observed GNSS satellite. Due to the refraction, the signal path bends, and it is possible to achieve communication between the satellites, even if one is slightly beyond the horizon of the other (Figure 4.11). At near-surface altitudes, the bending angle is generally 1°, but it reduces exponentially at higher heights. One receiver monitors hundreds of occultations in a single day that are well distributed over the globe (Gleisner et al., 2022). Each event yields high-quality vertical profiles of the neutral atmosphere (e.g., Wickert et al., 2001b; Schreiner et al., 2020) and the ionosphere (e.g., Jakowski et al., 2002; Arras et al., 2008).

Similarly to any terrestrial receiver, the observations of the LEO satellite can be described by Equation 4.2. At first, the clock desynchronization needs to be taken into account. Initially, this was achieved by introducing double-differentiated observations between two GPS satellites and two receivers, one deployed on an LEO satellite and a second installed on a ground station (Wickert et al., 2001a). The termination of the selective availability on 02.05.2000 marked the beginning of a new era in this technique. The GPS clocks became free of intentionally inserted fluctuations, allowing single-differentiated observations to be used (Wickert et al., 2002). Moreover, if the LEO satellite is equipped with a high-accuracy clock, zero differencing is possible (Wickert et al., 2005; Bai et al., 2018). After extracting the delays due to the atmosphere and the ionosphere for every individual frequency, the second step is determining the bending angle, which is a function of the Doppler shift and the relative motion between the receivers. This retrieval is not straightforward and requires several steps, some of which are solved iteratively. More information about this step is given in Hajj et al. (2002) and Elgered and Wickert (2017). After calculating the bending angles for every frequency, they must be corrected for the ionospheric effect. Similarly to the phase correction, the adjusted bending angle is given by the equation:

$$\alpha_c = \frac{f_1^2}{f_1^2 - f_2^2}\alpha_1 - \frac{f_2^2}{f_1^2 - f_2^2}\alpha_2 \tag{4.6}$$

where:
f carrier frequencies
α bending angles in every frequency

Consequently, the refractive index can be extracted by inserting the bending angle in Abel's inversion model.

$$n = \exp\left(\frac{1}{\pi}\int_a^\infty \frac{\alpha}{\sqrt{x^2 - a^2}}dx\right) \tag{4.7}$$

where a is the impact parameter (cf. Figure 4.11). The atmospheric refractivity in Equation 4.8 is associated to the pressure (P), the temperature (T), and the water vapour pressure (P_w) (Smith and Weintraub, 1953). In the case water vapour is absent, the dry temperature and pressure are obtained from the general gas and the hydrostatic equation (Melbourne et al., 1994; Kursinski et al., 1997). On the contrary, additional meteorological information has to be inserted (Gorbunov and Sokolovskiy, 1993).

$$N = (n-1)10^6 = 77.6\frac{P}{T} + 3.73\frac{P_w}{T^2}10^5 \tag{4.8}$$

The first mission, during which GNSS RO was introduced, was Global Positioning System/Meteorology (GPS/MET) in 1995 (Rocken et al., 1997; Schreiner et al., 1999). Additionally, Challenging Minisatellite Payload (CHAMP) and Gravity Recovery and Climate Experiment (GRACE)

were two missions that contributed positively to advancing this methodology (Wickert et al., 2001b, 2005). COSMIC-1 and the follow-up COSMIC-2, which is operational (as of August 2022), are two pioneering missions specially designed for RO (Liou et al., 2007; Schreiner et al., 2020). The results showed that one could achieve very high accuracy and vertical resolution with this method; thus, the output data is used for weather prediction (e.g., Healy et al., 2005; Kuo et al., 2000; Cucurull et al., 2014), and atmospheric and climate change studies (e.g., Steiner et al., 2009, 2011; Wickert et al., 2001b; Ho et al., 2009). GNSS RO is considered very robust and has been used to provide commercial data in the recent years (Borowitz, 2016; E. Bowler, 2020).

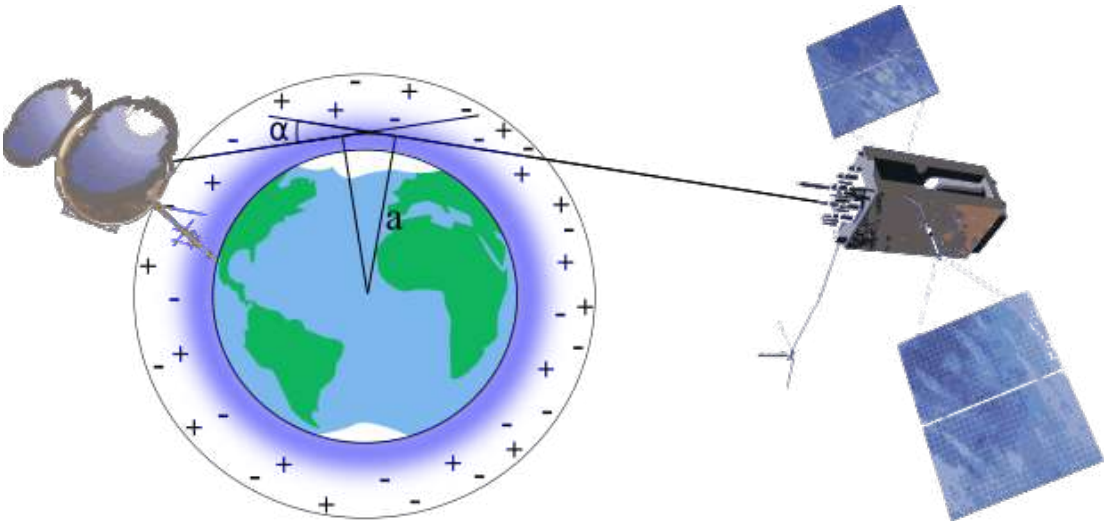

Figure 4.11: Propagation path through the atmosphere and the ionosphere Between a GPS and a COSMIC-1 satellite, showing the bending angle (α) and the impact parameter (a) (COSMIC-1 satellite rendered from the National Space Organization of the Republic of China[8], GPS satellite rendered from Lockheed Martin[9], Earth's shape taken from freesvg.org)[10].

4.2.2 Ground-Based Atmosphere Sounding

Ground-based Atmosphere Sounding (or GNSS Meteorology) is a technique that provides information about the atmosphere's water vapour with GNSS measurements. As shown in Equation 4.2, GNSS signals are delayed due to the propagation through the atmosphere. In accordance with Section 4.1.5, the atmospheric delay can be estimated, in network and single-station solutions during the data processing. The delay due to the atmosphere in the zenith direction (or Zenith Total Delay - ZTD) consists of two counterparts: the Zenith Hydrostatic Delay (ZHD) and the Zenith Wet Delay (ZWD). As explained in Elgered and Wickert (2017), the mathematical models of the zenith delays are:

$$Z_{total} = Z_{dry} + Z_{wet} \tag{4.9}$$

[8]https://www.nspo.narl.org.tw/history_prog.php?c=20030401&ln=en. Accessed: 08.05.2021
[9]https://www.lockheedmartin.com/en-us/products/gps.html. Accessed: 08.05.2021
[10]https://freesvg.org. Accessed: 08.05.2021

$$Z_{dry} = 10^{-6} \int_{h_{GNSS}}^{h_\infty} N_{dry}(z)dz \tag{4.10}$$

$$Z_{wet} = 10^{-6} \int_{h_{GNSS}}^{h_\infty} N_{wet}(z)dz \tag{4.11}$$

where:

Z_{total}	Zenith Total Delay
Z_{dry}	Zenith Hydrostatic Delay
N_{dry}	hydrostatic refractivity
Z_{wet}	Zenith Wet Delay
N_{wet}	wet refractivity
h_{GNSS}	height of the GNSS antenna
h_∞	height where atmosphere ends

A typical value for the ZTD is 2.5 m, the dominant component is the dry one, and it is 90 % of the entire delay (Hopfield, 1969), while the rest is the wet. The prior is very stable because it changes less than 1 % over a few hours (Navipedia, 2013), and it can be easily calculated with in-situ meteorological or weather model data. As explained in Saastamoinen (1972), the ZHD can be calculated by the equation:

$$Z_{dry} = \frac{0.00227768 P_0}{1 - 0.00266 \cos 2\phi - 0.00028 H} \tag{4.12}$$

where:

P_0	surface pressure
ϕ	latitude
H	orthometric height (in km)

On the other hand, the calculation of the ZTD and the ZWD is not straightforward; GNSS software packages primarily estimate the delay to the slant direction (or slant total delay - STD), which is later projected to the zenith direction. This process is achieved with the mapping functions (Figure 4.12), which are equations that show the dependency of the hydrostatic and wet delays on the elevation angle and -sometimes- the time (m_{dry} and m_{wet}, respectively). The first model is described in Marini (1972):

$$m = \frac{1}{\sin(e) + \frac{a}{\sin(e) + \frac{b}{\sin(e) + \frac{c}{\sin(e) + \ldots}}}} \tag{4.13}$$

where e is the elevation angle and a, b, c, ... are coefficients that need to be defined. Since then, similar functions have been developed. Niell's mapping function is relatively simple, and it does not require meteorological data (Niell, 1996), while Vienna mapping function 1 also depends on the day of year (Böhm et al., 2006b; Kouba, 2008). Moreover, a second category of mapping functions is utilized to compensate for the atmosphere's azimuthal asymmetry (m_{grad}). This approximation greatly improves the results because the atmosphere is not homogeneous in all directions. There are two main implementations of this mapping function; the prior (m^{ch}_{grad}) is described in Chen and Herring (1997), and it is dependent only on the elevation angle, while the latter (m^{bs}_{grad}) was introduced in Bar-Sever et al. (1998), and it also relies on the mapping function for the wet component.

$$m^{ch}_{grad} = \frac{1}{sin(e)tan(e) + 0.0032} \tag{4.14}$$

$$m^{bs}_{grad} = m_{wet} * cot(e) \tag{4.15}$$

According to Kačmařík et al. (2019), a complete expression of the observation equation of the STD can be written as follows:

$$S_{total} = m_{dry}Z_{dry} + m_{wet}Z_{wet} + m_{grad}(G_{NS}cos(a) + G_{EW}sin(a)) \tag{4.16}$$

where:

a	azimuth
Z_{dry}, Z_{wet}	Zenith Hydrostatic and Wet Delays
m_{dry}, m_{wet}	mapping functions for the dry and wet components
m_{grad}	mapping function of the gradient parts
G_{NS}, G_{EW}	gradients in the north-south and east-west directions

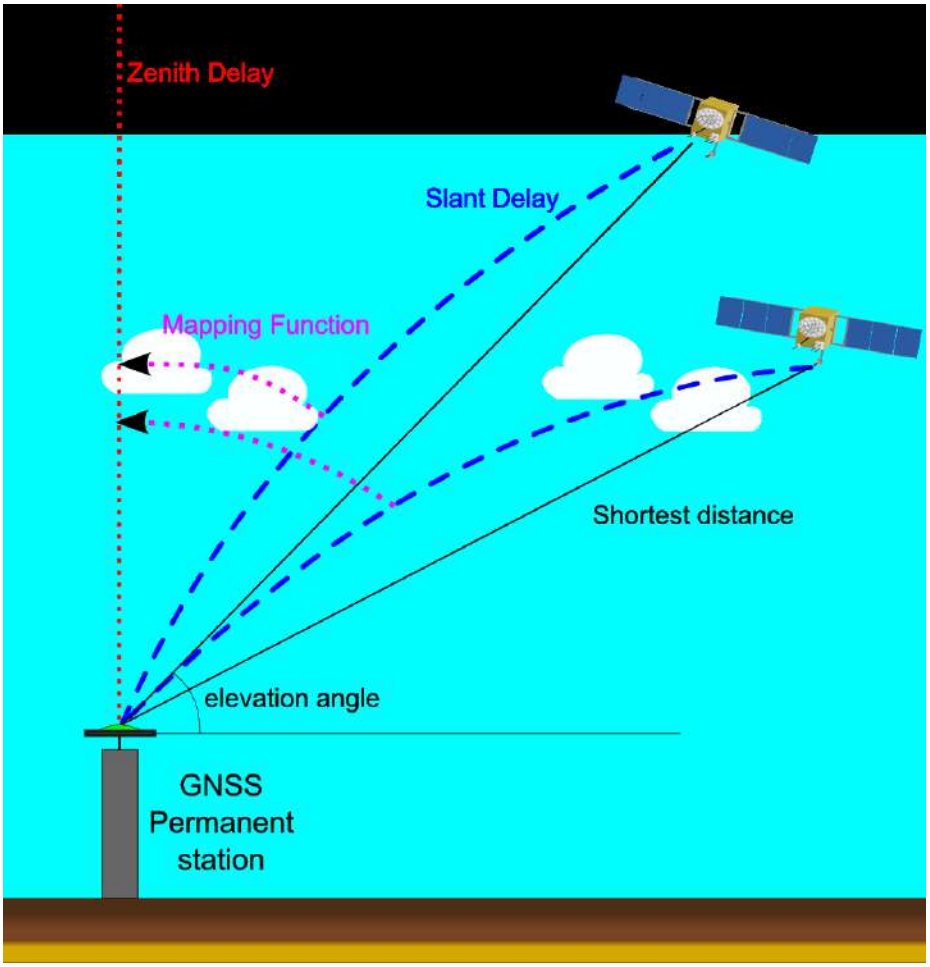

Figure 4.12: Propagation path of the electromagnetic signals. The slant observations are projected to the zenith direction with the use of the mapping functions (Reprinted from Simeonov, 2021).

The unknown parameters of Equation 4.16, are estimated by importing simultaneous observations in a least-squares adjustment. The last step of this process includes the calculation of the Total Precipitable Water (TPW), which represents the total amount of water along a vertical column. According to Bevis et al. (1994), this quantity can be derived from the ZWD as follows:

$$TPW = Z_{wet}\Pi \tag{4.17}$$

$$\Pi = \frac{10^6}{\rho R_u[(k_3/T_m) + k_2^{'}]} \tag{4.18}$$

$$k_2^{'} = k_2 - mK_1 \tag{4.19}$$

where:

ρ	density of liquid water
R_u	specific gas constant of water vapour
T_m	weighted mean temperature of the atmosphere
m	ratio of molar masses of water vapour and air
k_1, k_2, k_3	physical constants

It is important to mention that function Π yields unitless values; hence the water vapour is calculated in a length unit. In order to calculate the integrated water vapour (IWV), one has to omit the density of liquid water, due to which the unit conversion is very simple. As a reference, $1\,\mathrm{mm}\,TPW \approx 1\,\mathrm{kg\,m^{-2}}\,IWV$.

Ground-based Atmosphere Sounding is a very robust technique. The outcome can be used either individually (e.g., Priego et al., 2017; Jones et al., 2019) or for comparison with weather model data (e.g., Li et al., 2015; Wilgan et al., 2015; Alshawaf et al., 2017), or it can be inserted to weather models (e.g., Zus et al., 2011; Bennitt and Jupp, 2012; Rohm et al., 2019). Additionally, the STD can be used directly to create water vapour tomography. This technique is computationally intensive, and it requires a dense GNSS network, but it is very interesting because it provides continuous and not station-referred point data (e.g., Bender et al., 2011; Rohm, 2013; Möller, 2017).

4.2.3 GNSS Reflectometry

GNSS-R is a multistatic technique that examines the signal reflections and acquires physical properties from the reflection point/zone. There are various set-ups in which the antenna of the receiver is placed on a ground station, on an aeroplane, or a satellite (Rius and Cardellach, 2017). Unlike the previous GNSS remote sensing techniques, GNSS-R is very diverse, allowing calculations of multiple parameters depending on the set-up.

Sea-surface altimetry was the first GNSS-R application to be suggested through the Passive Reflectometry and Interferometry System concept in 1993 (Martin-Neira, 1993). This method requires two strongly attached antennas. The first one point upwards and receives the direct signals, while the second antenna is directed downwards and records the reflections. The distinction is made because of the antennas' orientation and polarization. By default, GNSS signals are right-hand circular polarized; hence the zenith-looking antenna is designed accordingly. On the contrary, the reflections may be both right- and left-hand circular polarized. Thus there are different set-ups with one or two kinds of antennas (Cardellach et al., 2011; Rius et al., 2012;

Camps et al., 2017; Semmling et al., 2014). The time delay due to the longer path of the reflected signal (cf. Figure 4.13) is derived by cross-correlating the observations. This procedure is similar to the internal cross-correlation of the receiver for calculating the distance between the antenna and the satellite (cf. Section 4.1.4). In this case, the reflection is correlated against either the direct signal or a local replica (Martin et al., 2014). GNSS-R altimetry can be achieved both with code and phase measurements. The prior are easy to use because they provide direct results, but the accuracy is limited due to the increased instrumental noise (Carreno-Luengo et al., 2014). On the other hand, phase measurements are more accurate, but the ambiguity has to be solved (Beckheinrich et al., 2012; Semmling et al., 2014). A simplified equation for the antenna height estimation is given as follows (Liu et al., 2017):

$$h = \frac{\Delta\rho}{2\sin\theta_d} + \delta b \tag{4.20}$$

where:
$\Delta\rho$ path delay of the reflected signal
θ_d elevation angle
δb corrections for the geometry of the antennas

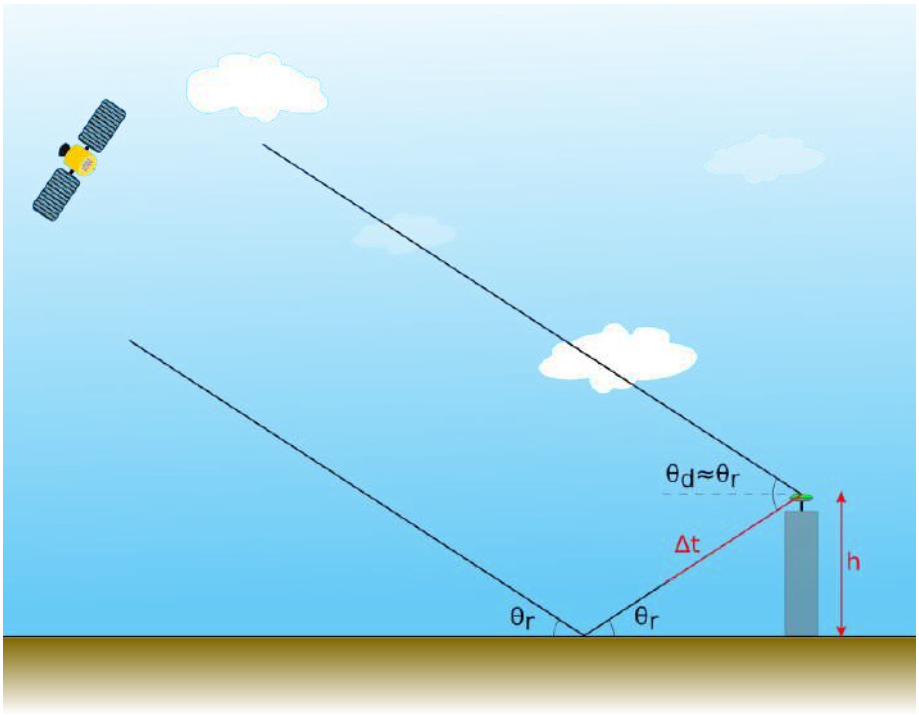

Figure 4.13: Multipath signal propagation in a ground-based GNSS station. The height (h) is analogous to the time difference (Δt). For low height differences, the atmospheric and ionospheric delays and the elevation (θ_d) and incidence (θ_r) angles are treated as identical.

An other set-up occurs when a single antenna receives both direct and reflected signals at the same time. This fact impacts all observables, but GNSS-R particularly exploits the signal strength.

More specifically, the direct and the reflected signals have a phase difference. When combined together, the interference results in a periodic pattern of the SNR measurements because the satellite changes its position, and the reflection geometry and the phase changes (Larson et al., 2008a; Rodriguez-Alvarez et al., 2009). Next, each satellite pass is split into the rising and setting counterparts. The measurements that coincide with the lower elevation angles are isolated, and the polynomial term is removed (cf. Figure 4.14). Finally, the readings are modelled into a cosine function with the following equation Larson et al. (2008b):

$$SNR\,(volt/volt) = 10^{\frac{C/N_0}{20}} \tag{4.21}$$

$$SNR\,(volt/volt) = A\cos(2\pi f \sin e + \phi) \tag{4.22}$$

$$f = \frac{2h}{\lambda} \tag{4.23}$$

where:

C/N_0	signal strength measurement, as given in Equation 4.5
e	elevation angle
λ	wavelength

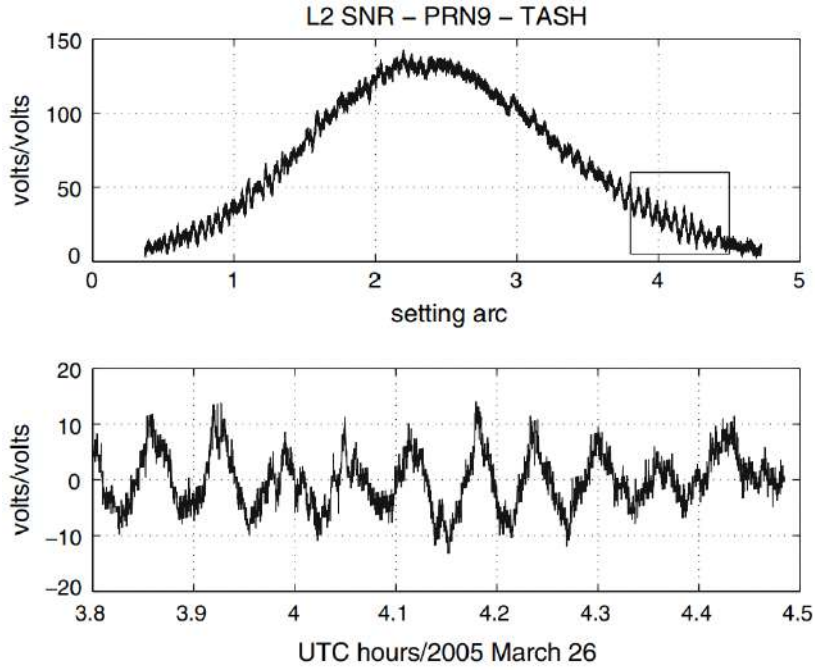

Figure 4.14: **Top:** SNR observations for the satellite with PRN 9 at the TASH station on 26.03.2005. **Bottom:** SNR observations for the setting arc. The polynomial term is removed in order to model the observations in a cosine wave (Reprinted from Larson et al., 2008a).

The amplitude (A), the antenna height (h), and the phase offset (ϕ) are unknown, and they are estimated in a least-squares adjustment. Each parameter provides different-kind information; the

amplitude is related to the a-priori signal power and decreases if the reflection area is covered with vegetation, the height depends on the geometry of the antenna (Bilich et al., 2008; Chew et al., 2016), and the initial phase provides information about the soil moisture (Larson et al., 2008a). In fact, relative changes in soil moisture are derived by comparing several initial phases of the same satellite pass that occurred during different epochs. This happens because the initial phase is dependent on the reflection depth, which is related to the dielectric properties of the soil. Considering that the dielectric constant of dry soil is around 3.5 and the dielectric constant of water is roughly 80 (Chew et al., 2016), a slight change in the ground's water content will directly alter its dielectric properties. The processing algorithm includes a combination of multi-temporal and -satellite phase offset estimations. A more detailed description of the methodology is provided in Chapter 5. Lastly, several studies have demonstrated that this technique has great potential and can contribute positively to the water cycle measurement (Larson et al., 2008b, 2009; Larson and Small, 2013; Vey et al., 2016a).

Apart from the applications described above, GNSS-R can provide information about texture and the nature of the reflection surface. Two novel missions that utilize small satellite technology were TechDemoSat-1 (ESA, 2021) and Cyclone Global Navigation Satellite System (CYGNSS) (NASA, 2019). In both cases, the satellites are equipped with nadir-looking antennas, and the primary outputs are the delay-Doppler maps (DDMs, Figure 4.15), which are the backscattered signal spreading in the time and frequency domain. The basic concept of this method is that reflections on smooth surfaces will be specular, and they will provide narrow spreading, while reflections on rough surfaces will be diffuse and provide wide spreading (Gleason and Ruf, 2015).

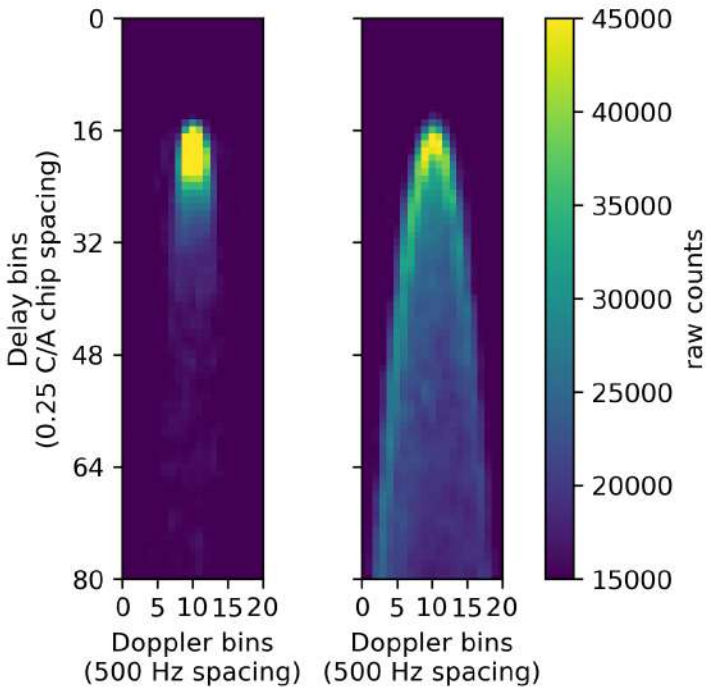

Figure 4.15: Cyclone Global Navigation Satellite System (CYGNSS) specular (left) and diffuse (right) reflection (delay-Doppler maps (DDMs) information retrieved from GYGNSS, 2020).

The preliminary scope of TechDemoSat-1 and CYGNSS missions was the measurement of the wind speed over oceans (Foti et al., 2015; Unwin et al., 2016; Ruf et al., 2017; Ruf and Balasubramaniam, 2018). The prior consists of only one small satellite, mainly designed for demonstration purposes (ESA, 2021), while the latter is composed of eight small satellites, and it was designed to study the inner core processes of the cyclones and enhance extreme weather predictions. CYGNSS focuses on reflections between $-38°$ and $38°$ latitude, where cyclones occur. Each satellite is able to track up to four reflections simultaneously, and the average revisit time is 4 h (NASA, 2019). Besides wind speed, DDMs may also be used for other applications. In Asgarimehr et al. (2018) is shown that rain over the ocean can be retrieved, whereas various studies specialize in spotting wetland areas and floods that might also alter dynamically (e.g., Chew et al., 2018; Morris et al., 2019; Loria et al., 2019). Furthermore, the DDMs can be alternatively employed for the estimation of the soil moisture (e.g., Chew and Small, 2018; Clarizia et al., 2019; Senyurek et al., 2020).

Chapter 5

Development and Evaluation of Methods for Estimating Soil Moisture

The main principles for soil-moisture estimation using multipath reflections were initially demonstrated in Larson et al. (2008a) and Larson et al. (2008b). Since then, it has been shown that this technique is effective, especially when vegetation is absent (Rodriguez-Alvarez et al., 2009; Vey et al., 2016a). In a further step, numerous research has been held for the removal of the vegetation noise (Chew et al., 2016; Small et al., 2016). This chapter demonstrates a new approximation for estimating soil moisture that simultaneously employs all carrier frequencies and constellations in a least-squares adjustment.

5.1 Software for Estimating Soil Moisture

This software was developed in the German Research Centre for Geosciences (Deutsches GeoForschungsZentrum - GFZ) and is compared against the previously-developed version of the same institute. Although the basic concept remains the same, several changes are implemented in the mathematical model to achieve better results.

5.1.1 Existing Software in the German Research Centre for Geosciences

All software packages developed for soil-moisture estimation with GNSS multipath are based on Equation 4.22. In addition, the GFZ is an analysis centre that has developed its own set of algorithms written in MATLAB programming language (MATLAB, 2018). The most prominent results are provided in Vey et al. (2016a) and Simeonov (2021).

As described in Simeonov (2021), this software exclusively uses GPS signals, namely L1, L2 and L5. As explained in Section 4.1.2, GPS orbits are very convenient to use because the satellites repeat a pass over the same position every sidereal day (23 h 56 min 4 s). Due to this fact, one can retrieve soil moisture from a single reflection path almost daily. On the other hand, GLONASS, Galileo, and BeiDou satellites have a repetition period of eight, ten and seven sidereal days, respectively. Thus the time series would have significant gaps in between. Moreover, due to the orbital period of GPS, each satellite completes two passes over the same point during

the day, one ascending and a second descending. Provided the effective elevation angles are between 0° and 30° during the rise and the set, one satellite can provide at most four independent reflection paths. This number decreases in some cases because of masking due to natural obstacles (e.g. mountain ranges) and low signal reception. Those tracks are positions where reflections occur when a satellite appears on the horizon. Since the satellites always pass from the same position and the landscape's topography remains constant, the geometry of the reflections does not change either. The only parameter that affects them is the dielectric constant of the soil, which alters due to its moisture.

The first step of this process is to check the version of the RINEX files and convert them into version 2 format if needed. This is achieved with GFZRNX, a GNSS data conversion and manipulation software package (Nischan, 2016). The second step is the extraction of the signal strength measurements and the satellite's orientation (elevation and azimuth) for every epoch by employing the application introduced in Roesler and Larson (2018). Then the observations from the desired frequency are selected; L2 is preferred to L1, while L5 provides the best reflections, but its availability is limited.

Follow-up, the SNR observations are inserted in Equation 4.21, and they are separated into reflection sets modelled into cosine waves. During the modelling process, the polynomial trend is removed from the converted SNR measurements, and the dominant frequency of the time series is calculated. This estimation is achieved with the Lomb-Scargle periodogram (Lomb, 1976; Scargle, 1982; Press and Rybicki, 1989). The next step is related to estimating the amplitude and the initial phase of the cosine wave in a least-squares adjustment, the mathematical model of which is described in Equation 4.22. Afterwards, the reflection sets that occur at the same position are grouped into individual reflection paths. This is done by dividing the station's vicinity into four zones depending on the azimuth (north-west, north-east, south-west, south-east) and associating the reflection paths with them. Each zone is 100° wide, and there is always an overlap of 10° in order not to split the reflections that occur on the borders. This fact is not problematic because the azimuthal distance between GPS orbits is sparse, and there is no chance for two reflection paths to take place in the same zone. In order to couple the changes in the soil conditions with the phase variations, the antenna height has to be fixed; hence the mean value is calculated for every reflection path, and the amplitude and initial phase are estimated again with the new averaged height.

All steps described above yield several reflection paths, up to four for each satellite, each linked to a series of initial phases and amplitudes that are referred to a particular epoch. Subsequently, soil-moisture time series are derived for each reflection path individually. More specifically, this estimation is described by the equation below:

$$sm_n\,(vol.\,\%) = S(\phi_n - \phi_0) + sm_{res} \tag{5.1}$$

ϕ	initial phase of certain reflection set
S	constant that connects phase and soil-moisture change
sm_{res}	residual soil moisture

The reference initial phase ϕ_0 can be the initial phase of any epoch, and the constant S is a value close to 1.48 v/v %/deg (Chew et al., 2014). This equation measures relative changes in soil moisture without considering the residual soil moisture. Thus the data series is shifted so that the lowest 5 % of all estimates are allocated to a specified minimum value. This value depends on the climatological conditions. For mid-latitude climates a reference value is 3.5 v/v %

(Simeonov, 2021). It is important to mention that reflection sets, which yield very low amplitudes or extreme initial phases, are excluded. As the last step, the reflection paths that provide non-noisy results are merged, and the final soil-moisture estimation is done by averaging the estimations on a daily basis.

In the case of multi-year observations, they are separated on a yearly basis, and they are processed individually. In order to have a transparent estimation, the selection of the reflection paths to be used during the entire period is made using data from only one year. If the selected reflection paths alter to align the estimation with external data, then the entire procedure would not be independent.

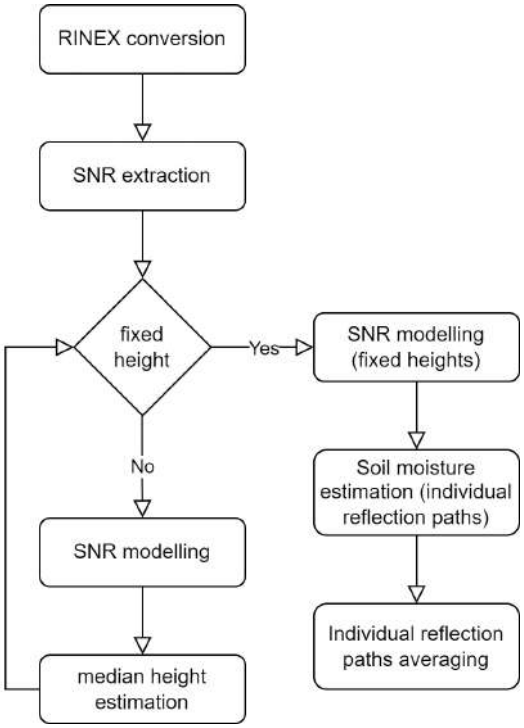

Figure 5.1: Flowchart for GNSS-R soil-moisture retrieval (existing version).

5.1.2 Software Improvement and Modernization

It has been shown that one can retrieve soil moisture with the already-developed software of the GFZ. However, there are some limitations, namely the incapability of processing multiple frequencies and constellations simultaneously and the empirical resampling of all estimations on a daily basis. Those facts were a motivation to write new modernized software. The programming language that is chosen is Python (Python, 2018) because it is open-source, and there is a plethora of libraries and documentation available.

The basic principles of soil-moisture derivation remain untouched, and the first steps are identical between the two software packages (cf. Figures 5.1 and 5.2). The RINEX files are converted with the GFZRNX tool (Nischan, 2016), and the rest of the process is held independently by the Python application. More specifically, the initial step of this procedure is related to the

extraction of the SNR observation and the calculation of the position of the satellite. In this case, the modification lies in the fact that satellites from all available constellations are considered. Similarly to the previous algorithm, Equation 4.21 is used to convert the observations, which are then split into reflection sets. Considering that the azimuthal distance between the reflection paths is not regular, the grouping methodology of the reflection sets has to change. The criterion for their clustering is the spatial pattern of the curve, which is a function of their elevation and azimuth. After the classification, the range of the effective elevation angles is calculated for each reflection path. A-priori, this is between 0° and 30°, but in the case of an uneven landscape, the quality of the cosine modelling would decrease. Thus a search for consecutive elevation angles, where the frequency does change significantly, is held. After defining this interval for every reflection path, the dominant frequency is calculated with the Lomb-Scargle periodogram for each set of reflections. Next, the characteristic frequency, and subsequently height, for each reflection path is derived by averaging. Following that, the SNR observations are modelled in a cosine wave using least-squares adjustment.

The most challenging part of this algorithm is using independent series of reflection sets with different sampling intervals. Since GPS provides four independent reflection paths with one-day temporal resolution and the other constellations provide tenths of reflection paths with temporal resolution between seven and ten days, it is impossible to process each series independently. As a result, all initial phases need to be inserted into a least-squares adjustment. The matrix of the unknowns (x) and the observation equation (δsm) are given in the following equations:

$$x = \begin{bmatrix} sm_1 \\ sm_2 \\ \vdots \\ sm_n \end{bmatrix} \tag{5.2}$$

$$\delta sm_{m-n}^{i-j-k} = sm_n^{i-j-k} - sm_m^{i-j-k} = S(\phi_n^{i-j-k} - \phi_m^{i-j-k}) \tag{5.3}$$

m, n epoch indicator
i satellite PRN (e.g. G01, R01, E01, C01)
j independent reflection path for each satellite (j=1 for i=G01 $\neq$ j=1 for i=G02)
k carrier signal (L1, L2, L5)
S constant that connects phase and soil moisture change

If no absolute soil-moisture observation is inserted into the system, it cannot be solved due to rank deficiency. In this case, six external measurements, three during the summer and the winter months are inserted into the system as observations. Thus the matrix of the observations (b) and the design matrix (A) have the following form:

$$b = \begin{bmatrix} \delta sm_{1-2}^{G01-1-L1} \\ \delta sm_{1-3}^{R01-2-L2} \\ \delta sm_{1-4}^{E01-3-L5} \\ \vdots \\ \delta sm_{m-n}^{i-j-k} \\ sm_1 \\ \vdots \\ sm_n \end{bmatrix} \tag{5.4}$$

$$A = \begin{bmatrix} -1 & 1 & 0 & 0 & \dots & 0 & 0 \\ -1 & 0 & 1 & 0 & \dots & 0 & 0 \\ -1 & 0 & 0 & 1 & \dots & 0 & 0 \\ \vdots & \vdots & \vdots & \vdots & \ddots & \vdots & \vdots \\ 0 & 0 & 0 & 0 & \dots & -1 & 1 \\ 1 & 0 & 0 & 0 & \dots & 0 & 0 \\ \vdots & \vdots & \vdots & \vdots & \ddots & \vdots & \vdots \\ 0 & 0 & 0 & 0 & \dots & 0 & 1 \end{bmatrix} \tag{5.5}$$

The weight matrix is created by applying the error propagation law on Equation 5.3 and using the a-posteriori standard deviations of the initial phases from the least-squares estimation. Since the signals are not equal in quality, the weights are scaled by a factor to be more realistic (L1 has a lower influence than L2, and L5 is the most trustworthy). Additionally, the soil-moisture observations from the external source are given significant weight because they are treated as errorless.

Similar to the previous approximation, there is a one or two-year training period when the appropriate reflection paths are selected. Finally, an other improvement is that blunders are detected through iterative data snooping.

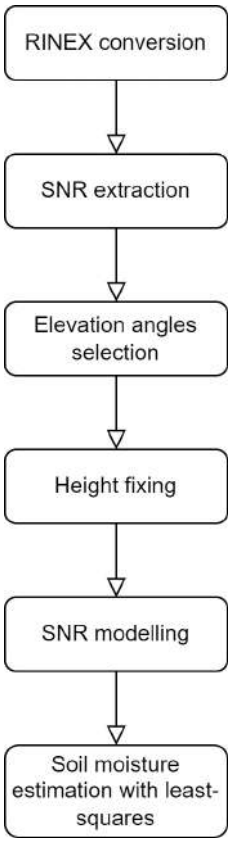

Figure 5.2: Flowchart for GNSS-R soil-moisture retrieval (modernized version).

5.2 Soil-Moisture Software Evaluation Using Data from Pilot Stations in Germany

5.2.1 Stations Description

Two pilot stations in northeastern Germany are used to test the software to be developed. Those stations operate for many years, and there are available solutions from previous research that could be used as reference (Simeonov, 2021). Different-quality sensors are installed in each station, and it is possible to compare their performance. Moreover, the GNSS measurements are always directly accessible, and there is no time delay between the data acquisition and the processing.

Marquardt Station

The facilities of this station are located in the Marquardt research site (Figure 5.3), which is administrated by the Leibniz Institute for Agricultural Engineering and Bioeconomy, and it is close to the homonym village in Brandenburg, Germany. This site provides secure equipment storage, and any experiment can be held under stable and traceable conditions. The landscape is ideal for reflectometry experiments because there are no obstacles, and all reflections occur on the ground. Moreover, the area is flat, and the vegetation is always kept low; hence the modelling of the reflections is simplified (Heistermann et al., 2023). Lastly, the field to the south is seasonally ploughed. Even though this generates noise to the observations, those periods are easily identified, and the impact of rough surfaces is further investigated.

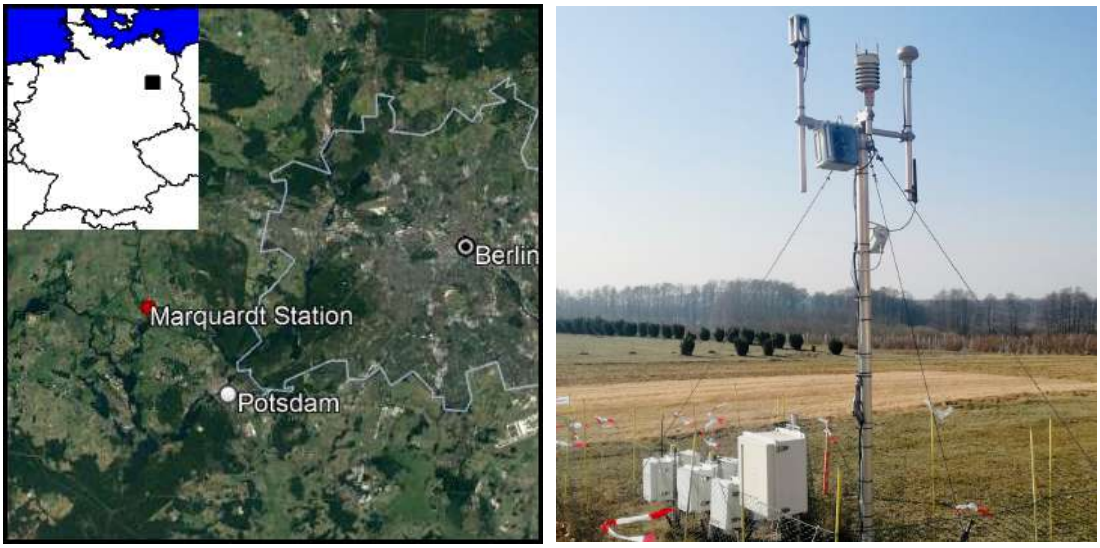

Figure 5.3: **Left:** Bird's eye view of the wider area of Marquardt, close to Berlin and Potsdam, Germany (Acquired from Google Earth[1]). **Right:** GNSS and meteorological equipment installed on a 3 m mast. The white boxes are utilized for storing the TDR-FDR loggers (Viewing angle in the south-east direction).

[1] https://www.google.com/intl/en/earth/. Accessed: 03.06.2021

The first GNSS receivers were installed in 2014, and since then, several hardware upgrades have been done. Unfortunately, there are some short periods when the operations are interrupted, but generally, the provided data are sufficient for the experiments. In addition to this equipment, the precipitation is monitored with a meteorological station, and multiple TDR-FDR sensors are installed at various depths to control and calibrate the reflectometry results. The data used for this experiment is taken from two GNSS receivers connected with a splitter to the same antenna. The primary device is a Javad Delta TRE-G3T multi-frequency and -constellation geodetic receiver and has operated since the first moment. It is a robust and pricey receiver used mainly for high-precision applications, and it can record signals from GPS, GLONASS and Galileo. The second device is a Swift Navigation Piksi Multi low-cost receiver which is also capable of recording multiple frequencies and constellations, except GLONASS in this case. It was installed in 2020, and its performance has yet to be evaluated. Its cost is significantly lower, but its capabilities are similar in theory. Lastly, the antenna to which all receivers are connected is an Antcom S67. This set-up allows direct comparison because there is no variation in the geometry, and all differences are subject to the signal acquisition quality. The naming of each receiver is given in the table below:

Abbreviation	**Type**
MARQ	Javad Delta TRE-G3T
MAR2	Swift Navigation Piksi Multi

Table 5.1: GNSS receivers set-up in Marquardt research site.

Fürstensee Station

Fürstensee station (Figure 5.4) is located next to the homonym lake, which is close to Neustrelitz, Mecklenburg-Vorpommern, Germany. Unlike Marquardt station, all equipment is installed in a grass field of a farm plant, and no other experimental activities are held around. This infrastructure has been originally established due to the needs of the Terrestrial Environmental Observatories project (Itzerott et al., 2018), and it has operated since 2011. The station's landscape is challenging because the receivers are installed on a small hill, and the reflection height varies dynamically. Finally, the entire region around the facility is very humid because of several lakes and water channels.

The general concept of the equipment set-up is similar to Marquardt station, but there are two minor differences. First, the Swift Navigation Piksi receiver is upgraded, and it is additionally compatible with GLONASS. Second, there is a third Geostar GeoS-5M low-cost receiver installed. Even though this device can record only one frequency, it is exciting to test because it may record all three constellations mentioned above, and it provides signal strength measurements with very high numerical resolution (0.002 instead of 0.25 $\mathrm{dB-Hz}$). The primary geodetic receiver was installed in 2013, while the low-cost ones were installed in 2020. Moreover, all receivers are connected to a Javad GrAnt-G3T antenna with a splitter.

It is important to mention that the TDR-FDR sensors are located at the bottom of the hill, similar to where the reflections occur. Even though they are co-located, the soil moisture is expected to differ because the landscape is generally inhomogeneous, and the water tends to follow the topographic gradient. The characteristic abbreviations of the GNSS receivers are given in the table below:

Abbreviation	Type
TRFS	Javad Delta TRE-G3T
TRF1	Swift Navigation Piksi Multi
TRFG	Geostar GeoS-5M

Table 5.2: GNSS receivers set-up in Marquardt research site.

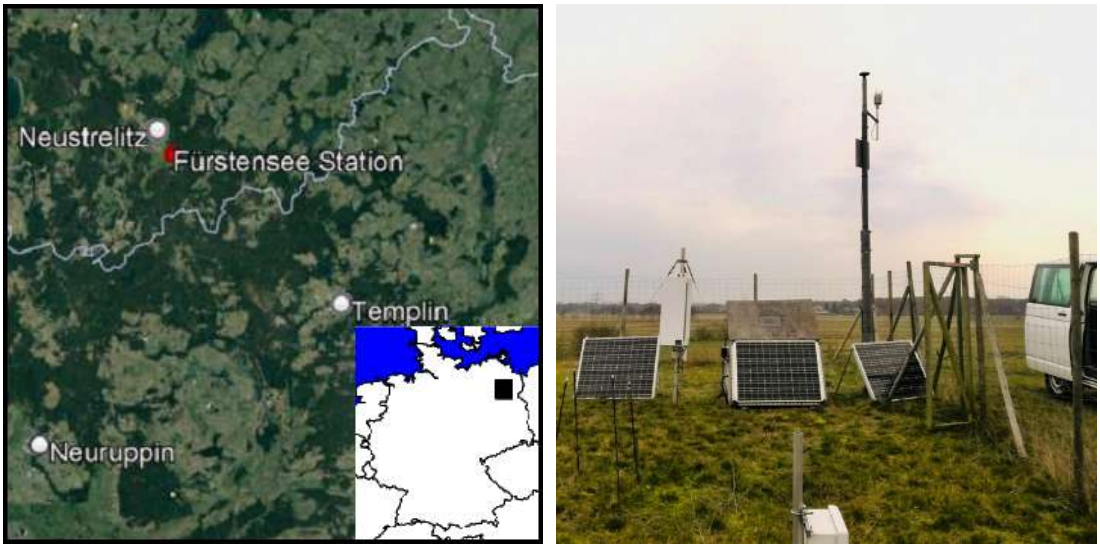

Figure 5.4: **Left:** Bird's eye view of the wider area of Fürstensee lake, in the borders between Mecklenburg-Vorpommern and Brandenburg, Germany (Acquired from Google Earth[2]). **Right:** GNSS and meteorological equipment attached on a 4 m mast, as well as solar panels installed for energy supply (Viewing angle in the north direction).

In addition, soil moisture is measured at this site with other non-conventional methods. More specifically, a cosmic-ray neutron-sensing (CRNS) method measures the incoming and outgoing energy range of the neurons generated by cosmic radiation interacting with the ground (Figure 5.5). Provided that there is an energy loss due to the collision with the hydrogen, water concentration can be mapped and quantified (Zreda et al., 2012; Köhli et al., 2015). This technique was initially introduced in Zreda et al. (2008) and in Desilets et al. (2010), and some applications are demonstrated in Fersch et al. (2020) and Rasche et al. (2021). This sensor has operated since 2015, and the results are inter-compared with the rest of the solutions.

Figure 5.5: Cosmic-ray sensor installed in Fürstensee station. The device is some metres away from the GNSS receivers (Looking angle in the south direction).

[2]https://www.google.com/intl/en/earth/. Accessed: 03.06.2021

5.2.2 Experiment Results and Discussion

The algorithm is validated using measurements from both stations, and the time series are compared against both the TDR-FDR observations, which are used as a reference, as well as the previous algorithm, according to availability. Additionally, all plots include precipitation and temperature information from the meteorological stations. The prior is useful because it triggers soil-moisture upraise, and the latter indicates frost and drought periods. The evaluation indices are the correlation and the root-mean-square error (RMSE). Since soil moisture and precipitation are not measured with the same units, there is no RMSE between those quantities. The selected reflections occur during the rise and the set of the satellites for elevation angles between 0° and 30°. Moreover, the constant S in Equation 5.1 is initially set to $1\,\mathrm{v/v}$ %/deg, as suggested in Simeonov (2021). Lastly, six fixing values for each year are inserted as observations to solve the rank deficiency problem. Those values are taken from the TDR-FDR sensors and correspond to the monthly highs and lows during winter and summer, respectively.

GNSS-R Soil-Moisture Estimation from Geodetic Receivers

The geodetic receivers provide the most extended time series because they were the first to be installed. In both stations, soil moisture is retrieved between January 2015 and December 2021. The selection of the appropriate reflection paths for the entire time frame could not be made from the first one or two years because the series drift. Moreover, GLONASS and Galileo were modernized during this period. Thus it is decided to split the measurements into three tri-annual windows with an overlapping season each other. The initial year of each window (in this case, 2015, 2017 and 2019) constitutes the training period, and the subsequent ones are referred to as the soil-moisture estimation. Since no observations were utilized before 2015, the initial season is used for training and estimation. The derived soil moisture is compared against the TDR-FDR time series, and the results are obtained using the previous algorithm, depending on availability. The results are compared with the solutions from the initially developed algorithm from the GFZ (Simeonov, 2021). This time series covers the period from 2015 until 2018. Lastly, this section only includes a few seasons, and the complete time series can be found in Appendix B.

The results from the MARQ station show that soil moisture can be effectively derived with GNSS-R measurements. GPS is always kept as the primary constellation due to its temporal resolution, and other combinations are evaluated. The results show good agreement between all GNSS-R solutions throughout the entire period. However, in this particular case, GLONASS and Galileo satellites' limited availability (and impact) should be considered. Moreover, with the examination of each season separately, summer is the most interesting one. Temperature is dominant, and the TDR-FDR sensors hardly spot precipitation events. On the other hand, GNSS-R solutions are more effective in detecting rain. Even though both methods measure the same quantity, they are supposed to provide different results because they do not measure it in the same location. TDR-FDR sensors are located $5-10\,\mathrm{cm}$ below the surface, while the reflections usually take place higher. Although this distance does not seem significant, it influences the measurements because water evaporates faster during the summer season, and it does not always manage to penetrate deeper into the soil. Even though the correlation with the TDR-FDR sensors is better in the winter season, reflectometry time series generally yield higher soil-moisture estimates. This indicates that the frost that accumulates on the ground's surface influences the solutions.

Comparing the results with the previous algorithm, the estimates of the antecedent approximation are predominantly higher during the entire period, but the differences were more prominent in 2018. Those fluctuations occur during the hot and cold seasons, and there is allegedly a parallel shift between the solutions. This difference arises because the anterior algorithm does not utilize absolute soil-moisture measurements to calibrate the time series.

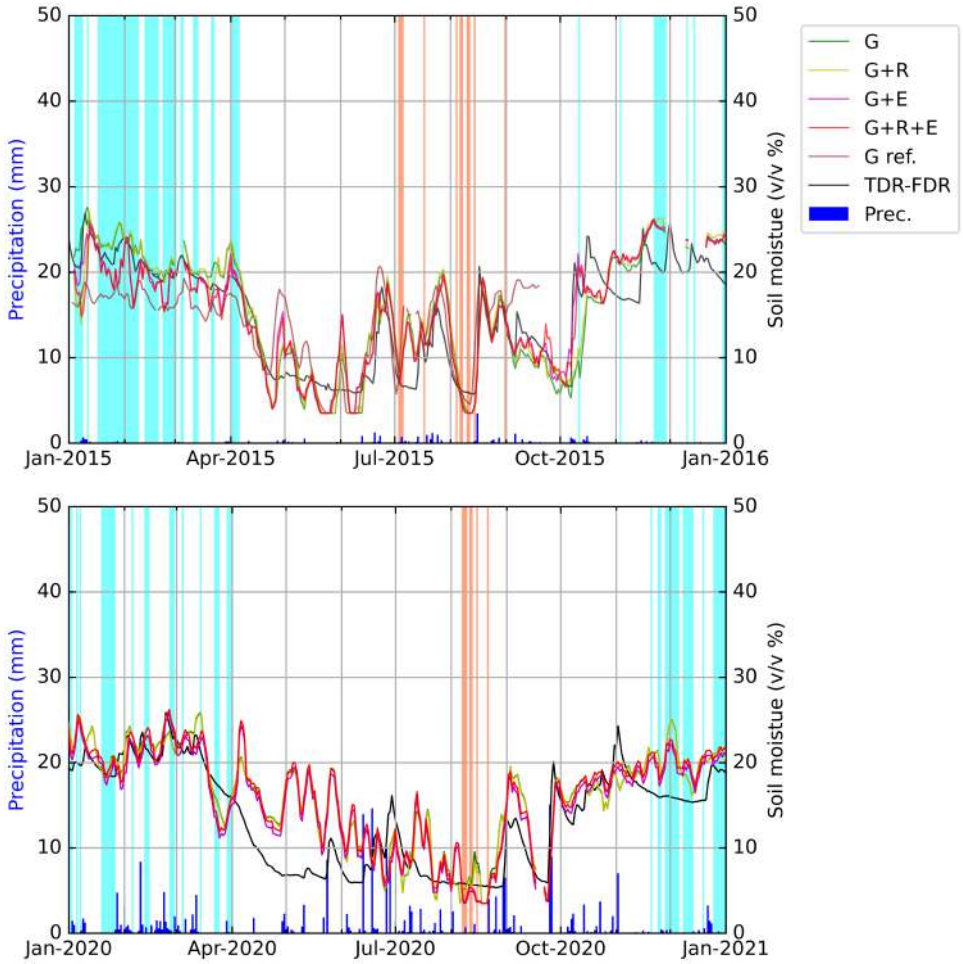

Figure 5.6: Soil-moisture estimation in MARQ station during 2015 (top) and 2020 (bottom). G, R, and E indicate GPS, GLONASS, and Galileo, respectively; in addition, G ref. is associated with the time series derived from the previous algorithm (Simeonov, 2021). Days with temperatures below 4 °C are labelled with a cyan background, whereas days with temperatures over 25 °C have a red background. The vertical blue bars show the precipitation.

Independently of the constellation(s) that is/are used, all solutions are highly correlated with the TDR-FDR time series, and their RMSE is very low. The introduction of redundant information improves the overall quality of the results. More specifically, the combination of GPS, GLONASS and Galileo is marginally superior to using one or two constellations. However, the statistics of the previous algorithm show that it does not perform as well as its modernised version, regardless of the solution that is selected for the comparison. The most intriguing aspect of the findings is

that there is no correlation between the precipitation events and any of the solutions. Although soil moisture and precipitation are strongly linked, they are two mechanisms that act differently. Precipitation occurs instantaneously, while soil-moisture decay is a process that lasts several days.

Correlation							
	G	G+R	G+E	G+R+E	G ref.	TDR-FDR	Prec.
G	1.00	0.99	0.95	0.95	0.80	0.78	-0.04
G+R	0.99	1.00	0.95	0.96	0.79	0.78	-0.04
G+E	0.95	0.95	1.00	0.99	0.78	0.78	-0.06
G+R+E	0.95	0.96	0.99	1.00	0.77	0.78	-0.05
G ref.	0.80	0.79	0.78	0.77	1.00	0.72	0.05
TDR-FDR	0.78	0.78	0.78	0.78	0.72	1.00	0.00
Prec.	-0.04	-0.04	-0.06	-0.05	0.05	0.00	1.00

Table 5.3: Correlation between all soil-moisture estimations in MARQ station for the entire period from 2015 to 2021. The naming conventions for each solution are consistent with those shown in Figure 5.6.

RMSE (v/v %)						
	G	G+R	G+E	G+R+E	G ref.	TDR-FDR
G	0.00	0.77	2.27	2.29	4.63	4.95
G+R	0.77	0.00	2.22	2.11	4.71	4.94
G+E	2.27	2.22	0.00	0.79	4.67	4.71
G+R+E	2.29	2.11	0.79	0.00	4.70	4.62
G ref.	4.63	4.71	4.67	4.70	0.00	5.34
TDR-FDR	4.95	4.94	4.71	4.62	5.34	0.00

Table 5.4: RMSE in v/v % between all soil-moisture estimations in MARQ station for the entire period from 2015 to 2021. The naming conventions for each solution are consistent with those shown in Figure 5.6.

The strategy followed in the TRFS station is consistent for easier comparison; GPS is kept as the primary constellation, and the others are considered auxiliary. The results from this station demonstrate again that the reflectometry method is very competitive. In contrast to the previous case, the introduction of GLONASS and Galileo is critical for developing better solutions. This is more notable in the later years when the availability and, subsequently, the impact of those constellations increases. The most problematic intervals in this station generally occur during the autumn and winter seasons when all GNSS-R results are significantly higher than the TDR-FDR ones. This period is always very cold with extensive frost. As proven in the previous station, the accumulation of ice and/or de-frozen water on the ground's surface creates difficulties in estimating soil moisture. Finally, besides this behavioural similarity, there is also a difference between the stations. The most notable disagreement is that precipitation events during summer are more often detected. As mentioned in the station description and discussed in previous research in Simeonov (2021), the fact that the area's topography is highly variable plays a dominant role in the soil conditions. Even at a small distance, some areas are drained due to surface and sub-surface run-off, whereas other areas experience water accumulation.

With respect to the previous algorithm, the results do not have homogenous behaviour. Even though they are well correlated with the TDR-FDR series, there is a non-negligible amount of cases when they experience both positive and negative shifts. This drift probably occurs due to the lack of absolute calibration and is already mentioned in the MARQ station.

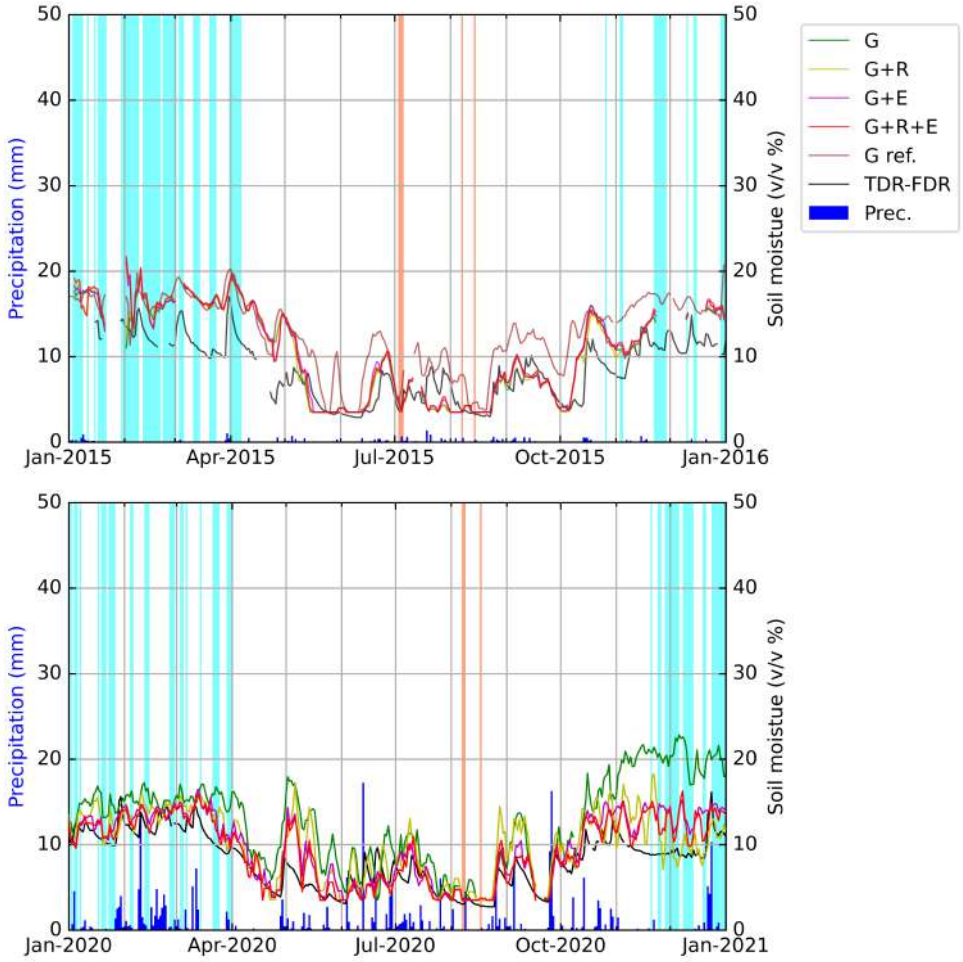

Figure 5.7: Soil-moisture estimation in TRFS station during 2015 (top) and 2020 (bottom). G, R, and E indicate GPS, GLONASS, and Galileo, respectively; in addition, G ref. is associated with the time series derived from the previous algorithm (Simeonov, 2021). Days with temperatures below 4 °C are labelled with a cyan background, whereas days with temperatures over 25 °C have a red background. The vertical blue bars show the precipitation.

The estimations' statistics show that all solutions' performance is satisfying, but there are some noteworthy differences. In this case, the influence of GLONASS and Galileo can be better evaluated because its observations are widely available. The combination of an additional constellation with GPS always increases the performance; subsequently, its influence is always positive. On the other hand, the combination of GPS and Galileo yields better results than the use of all available information. In addition, compared to the results of the previous algorithm, the modernised version always performs better, and the differences range between 0.45 and 1.57 v/v %.

Lastly, there is again minimal correlation between the precipitation and all soil-moisture time series. This behaviour is also noted in the previous station, and it shows that a low correlation between those quantities is to be expected.

Correlation							
	G	G+R	G+E	G+R+E	G ref.	TDR-FDR	Prec.
G	1.00	0.91	0.91	0.89	0.76	0.67	0.03
G+R	0.91	1.00	0.93	0.95	0.77	0.70	-0.02
G+E	0.91	0.93	1.00	0.98	0.79	0.76	-0.01
G+R+E	0.89	0.95	0.98	1.00	0.79	0.75	-0.01
G ref.	0.76	0.77	0.79	0.79	1.00	0.71	0.02
TDR-FDR	0.67	0.70	0.76	0.75	0.71	1.00	0.08
Prec.	0.03	-0.02	-0.01	-0.01	0.02	0.08	1.00

Table 5.5: Correlation between all soil-moisture estimations in TRFS station for the entire period from 2015 to 2021. The naming conventions for each solution are consistent with those shown in Figure 5.7.

RMSE (v/v %)						
	G	G+R	G+E	G+R+E	G ref.	TDR-FDR
G	0.00	2.47	2.54	2.67	4.39	4.75
G+R	2.47	0.00	1.93	1.67	4.40	3.84
G+E	2.54	1.93	0.00	0.90	4.35	3.49
G+R+E	2.67	1.67	0.90	0.00	4.30	3.63
G ref.	4.39	4.40	4.35	4.30	0.00	5.20
TDR-FDR	4.75	3.84	3.49	3.63	5.20	0.00

Table 5.6: RMSE in v/v % between all soil-moisture estimations in TRFS station for the entire period from 2015 to 2021. The naming conventions for each solution are consistent with those shown in Figure 5.7.

GNSS-R Soil-Moisture Estimation from Low-Cost Receivers

The low-cost receivers provide a significantly shorter time series because they had been operational only during the last year of the experiment in 2021. Despite the limited temporal availability, this time frame is long enough to extract initial conclusions about their capabilities. The results are evaluated by comparing them with the TDR-FDR sensors and the geodetic receivers. Provided that the quality of the GNSS-R solutions remains consistent during the entire period (cf. Appendix B), the fact that there is no separation between the training and the estimation period does not affect the integrity of the comparison. Moreover, since the statistics of the experiment with the geodetic receivers in Tables 5.4 and 5.6 show that aggregation of multiple constellations is beneficial, it is decided to directly combine GPS, GLONASS and Galileo, and not to examine the combinations separately.

The reflectometry time series at Marquardt does not depict significant differences between the performance of the geodetic receiver and the low-cost one. They fit well with each other, and they do not vary remarkably from the TDR-FDR sensor. As already noted in the previous experiment, the most problematic period is again the cold season. In addition, one can observe each

solution's individual behaviour in May. During this month, the station experienced excessive precipitation, but this alone cannot be the reason for this irregular attitude. There are other epochs with similar, or higher, precipitation when all series act in agreement. An other parameter that must be taken into account is that the rainy period follows a prolonged season of frost. Additionally, the temperature readings refer to the air and not the soil. This aspect is critical because the heat capacities between the two materials are entirely different, and the transition from the cold to the warm season, or the opposite, occurs at different rates.

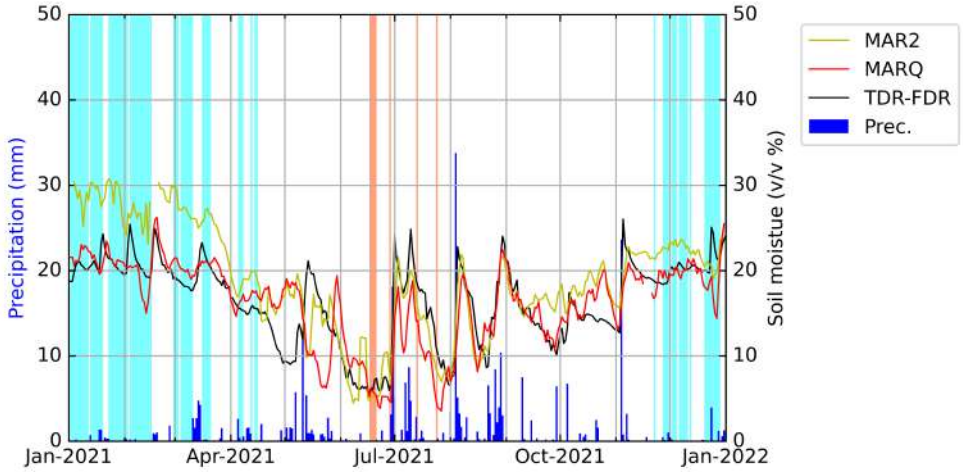

Figure 5.8: Soil-moisture estimation for the geodetic (MARQ) and the low-cost (MAR2) stations in Marquardt during 2021. Days with temperatures below 4 °C are labelled with a cyan background, whereas days with temperatures over 25 °C have a red background. The vertical blue bars show the precipitation.

The statistical analysis reveals a similar-quality correlation compared with the previous experiment. On the other hand, the RMSE levels are different. In absolute terms, the deviation is at the level of 1 v/v %, but in relative terms, it is greater than 30 %. This is feasible because the weather conditions in each season are characterized by distinct frost and heatwave periods, and it is only sometimes possible to achieve the same performance. Furthermore, the station-wise comparison depicts the superiority of the geodetic receiver. Despite this fact, the performance of the MAR2 station is satisfactory, indicating that low-cost receivers could be employed in soil-moisture estimation applications.

Correlation				
	MARQ	MAR2	TDR-FDR	Prec.
MARQ	1.00	0.87	0.74	-0.09
MAR2	0.87	1.00	0.79	-0.10
TDR-FDR	0.74	0.79	1.00	0.02
Prec.	-0.09	-0.10	0.02	1.00

Table 5.7: Correlation between the geodetic and the low-cost stations in Marquardt during 2021. The naming conventions for each solution are consistent with those shown in Figure 5.8.

RMSE (v/v %)			
	MARQ	MAR2	TDR-FDR
MARQ	0.00	4.28	3.54
MAR2	4.28	0.00	4.69
TDR-FDR	3.54	4.69	0.00

Table 5.8: RMSE in v/v % between the geodetic and the low-cost stations in Marquardt during 2021. The naming conventions for each solution are consistent with those shown in Figure 5.8.

Considering the previously mentioned challenging landscape of the Fürstensee site and the examination of a second low-cost receiver, this facility yields fascinating results. Again, in this case, the Swift Navigation receiver (TRF1) yields significantly greater soil-moisture readings than the TDR-FDR sensors, whereas the Geostar receiver (TRFG) is very competitive. Besides this, there are two occurrences in May and July when the precipitation events are not totally detected (cf. Figure 5.9). On the contrary, the rain incidents before and after are well recorded. Even more intriguing is that the receiver with the worst performance (TRF1) acts better during those intervals. According to the form of the time series, one can presume different constants (cf. Equation 5.1) for each receiver.

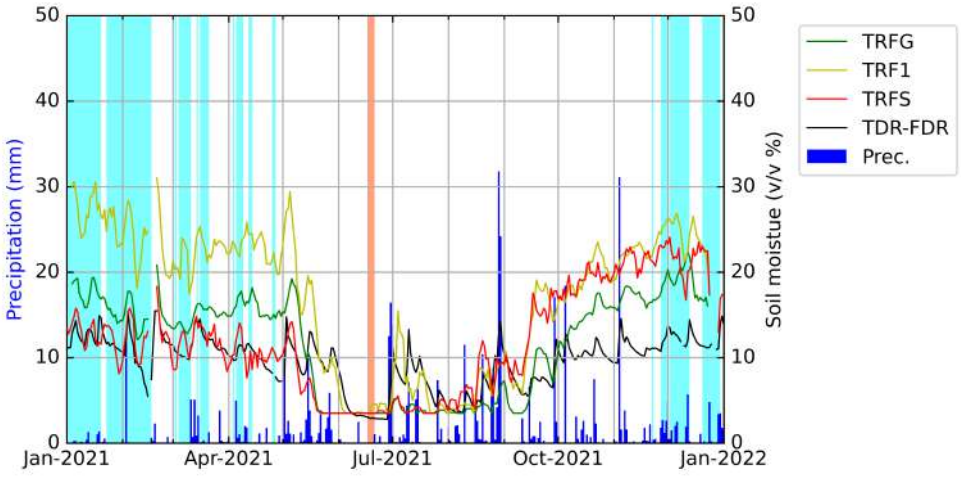

Figure 5.9: Soil-moisture estimation for the geodetic (TRFS) and the low-cost (TRF1 and TRFG) stations in Fürstensee during 2021. Days with temperatures below 4 °C are labelled with a cyan background, whereas days with temperatures over 25 °C have a red background. The vertical blue bars show the precipitation.

The statistics of this experiment indicate the poorer performance of the TRF1 station. The difference in the RMSE between TRFS and TRF1 approaches the 4 v/v %, which suggests that the results for this period as nearly twice worse. Thus this time frame is, in general, challenging to estimate soil moisture. An other parameter that should be taken into account is the better performance of the TRFG station. Even though this receiver is the most inexpensive, it is very effective and shows that it can be employed in future applications.

Correlation					
	TRFS	TRF1	TRFG	TDR-FDR	Prec.
TRFS	1.00	0.71	0.78	0.60	-0.13
TRF1	0.71	1.00	0.95	0.80	-0.14
TRFG	0.78	0.95	1.00	0.76	-0.16
TDR-FDR	0.60	0.80	0.76	1.00	0.04
Prec.	-0.13	-0.14	-0.16	0.04	1.00

Table 5.9: Correlation between the geodetic and the low-cost stations in Fürstensee during 2021. The naming conventions for each solution are consistent with those shown in Figure 5.9.

RMSE (v/v %)				
	TRFS	TRF1	TRFG	TDR-FDR
TRFS	0.00	7.80	4.07	5.50
TRF1	7.80	0.00	6.33	9.66
TRFG	4.07	6.33	0.00	4.63
TDR-FDR	5.50	9.66	4.63	0.00

Table 5.10: RMSE in v/v % between the geodetic and the low-cost stations in Fürstensee during 2021. The naming conventions for each solution are consistent with those shown in Figure 5.9.

Comparison with the Cosmic-Ray Soil-Moisture Method

The CRNS equipment is only available at Fürstensee, and time series were calculated for the period between 2015 and 2020. Additionally, this technique measures soil moisture at a deeper layer, between 10-30 cm. Considering the variation of the soil moisture with the depth, the objec-

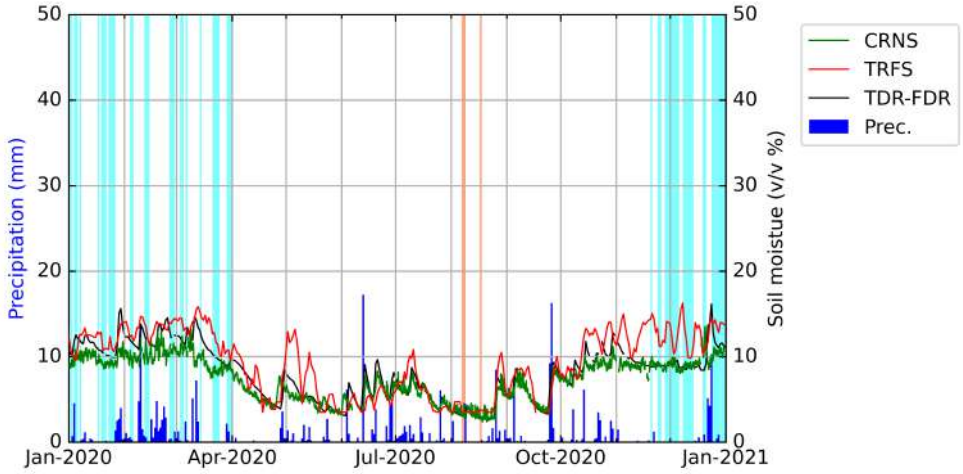

Figure 5.10: Comparison between the GNSS-R (TRFS) and the cosmic-ray neutron sensing (CRNS) soil-moisture time series at Fürstensee for 2020. Days with temperatures below 4 °C are labelled with a cyan background, whereas days with temperatures over 25 °C have a red background. The vertical blue bars show the precipitation.

tive in this experiment is not the detection of the most competitive solution but the evaluation of moisture-depth dependency under various weather conditions. Lastly, according to the previous experiment, the GNSS-R data set refers to the multi-constellation solution.

Despite the fact that the reflectometry time series do not differ considerably from the CRNS ones, some considerable periods depict behavioural variability. Firstly, GNSS-R always yields higher values compared to TDR-FDR and CRNS. This occurs because each method takes measurements at different horizons, pointing out the moisture-depth relationship. Additionally, the fluctuation between the time series is enhanced during winter, and there are some precipitation events to which the reflectometry solution is more sensitive. This outcome is consistent with the prior experiments, showing that GNSS-R is more accurate at detecting rain but can be biased by frost. Lastly, the similarity level between the data series is reflected by the statistics. Considering the TDR-FDR the reference data set, the RMSE of the reflectometry is at the level of 3 v/v %, while the CRNS is closer by 1 v/v %. Furthermore, the correlations are high, ranging between 0.79 and 0.83.

5.2.3 Conclusions

This chapter highlights the potential of the GNSS-R methodology for soil-moisture estimation by employing a modernized algorithm. Three experiments were held using data from two pilot stations in northeastern Germany. Each site includes various-quality receivers, and the datasets span from 2015 to 2021. Furthermore, the reflectometry time series are compared against the solution of the CRNS equipment. Concerning the experiment results, the following key points are derived:

- GNSS-R can be effectively used for measuring soil moisture. This methodology generally yields satisfying results and can be applied using existing infrastructure. Moreover, this technique has some limitations; the observations need to be calibrated and require an obstacle-free and flat environment.
- The modernized algorithm for soil-moisture estimation is more competitive than the older one. The statistics of this version are always better, showing a relative improvement up to 33 %. This is because it utilizes more observations and, most importantly, employs a more sophisticated mathematical model.
- The low-cost receivers show that they may also be used for soil-moisture applications. For example, even though all models do not perform equally well, in the case of the Geostar GeoS-5M model that acquires multiple-decimal-digits observations, the low-cost device outperforms the geodetic one. This fact also points out that the numerical resolution of the measurements is crucial for the integrity of the end result.
- The time series of the CRNS methodology demonstrates a higher level of agreement than the GNSS-R one, when compared to the TDR-FDR reference dataset. Considering that both solutions are high quality, this outcome highlights the soil-moisture decay with the depth and the fact that each technique is expected to yield slightly different outputs.

Chapter 6

Sea-Level Monitoring Campaign

An auxiliary application of single-antenna GNSS-R is estimating the height between the antenna and the reflection area. Consequently, the software that was employed in Chapter 5 can also be utilized for sea-level monitoring. This chapter investigates the capabilities of this approximation using data from two stations in the Netherlands and France.

6.1 Software for Estimating Sea level

Unlike soil moisture applications, where the geometry of the reflections remains constant, in this case, the sea level is constantly affected by the tides and changes dynamically. The software that was used for this application is a modified version of the software for soil moisture estimation. It focuses on the antenna-height estimation and the modelling of the observations to describe the tidal oscillation.

6.1.1 Antenna-height Estimation

There are various applications where height changes are dependent on initial phase changes of modelled SNR measurements, as described by Equations 4.21 and 4.22 (Vey et al., 2016b; Simeonov, 2021). However, those approximations cannot be directly used for sea-level monitoring because they provide relative measurements and require the initial state of the sea level. Additionally, the temporal resolution of the measurements is not sufficient because it usually equals one day, while an oscillation has the main period of approximately 12.5 h. The algorithm that was employed in this case utilizes the frequency of the modelled SNR measurements (cf. Equation 4.23). Therefore, the observations are absolute, and each set of reflections can be individually used to derive sea-level height. Due to this fact, one can utilize any constellation independently to acquire a solution. Moreover, since the tides act dynamically, the reflection sets were split into intervals of ten minutes to monitor height changes with higher temporal resolution. Lastly, the time tag of the estimated height was set according to the central epoch of the reflection set.

6.1.2 Outlier Detection

Provided that each height (or carrier-signal frequency) estimation is independent, the options for outlier detection are limited. Consequently, the evaluation of the results is based on two factors, the a-posteriori standard deviation of the estimated height and the spectral analysis of the time series. More specifically, the values with a low standard deviation that match the resulting

frequency of the tides were selected for the sea-level estimation.

The Solar and Lunar gravitational forces, and the rotation of the Earth influence the level of terrestrial water bodies. Each parameter has a different amplitude and frequency; the most critical factor is the Moon's gravitational pull. In addition, the water-level rise depends on the coastline's structure, the shore's bathymetry, the wind speed and the atmospheric pressure (Reddy and Affholder, 2002). The harmonics that principally describe the tides are given in the following table:

Coef. Name	Period (days)	Description
M_2	0.51752505	Principal lunar semi-diurnal
S_2	0.5	Principal solar semi-diurnal
N_2	0.52743115	Larger lunar elliptic semi-diurnal
ν_2	0.52608355	Larger lunar evectional
2"N_2	0.53772387	Lunar elliptical semi-diurnal second-order
λ_2	0.50924056	Smaller lunar evectional
L_2	0.50798420	Smaller lunar elliptic semidiurnal
K_2	0.49863484	Lunisolar semidiurnal
K_1	23.93447213	Lunar diurnal
O_1	25.81933871	Lunar diurnal
P_1	24.06588766	Solar diurnal

Table 6.1: Semi-diurnal and diurnal harmonics that principally describe the tides, based on their amplitude.

In this case, harmonics that yield more extended periods were excluded because their influence is minor, and the length of the observations is not enough to detect them accurately. The components that were chosen for the initial filtering of the time series were M_2, S_2, N_2, ν_2, K_1 and O_1 , and the unique criterion for this selection was their amplitude.

6.2 Stations Description

Two GNSS stations were selected for the sea-level monitoring campaign. The location of those sites is ideal for this application because they are near the shore, and the antennas are mounted on high monuments, able to record reflections of the full spectrum of the elevation angles. Finally, both stations face the Atlantic Ocean from the central European side, where high-amplitude tides usually occur.

6.2.1 Vlissingen Station

The facilities of this site are located at the entrance of the harbour of Vlissingen in the south-western Netherlands (cf. Figure 6.1). More specifically, they are situated on the north side of the estuary of the Scheldt river, which opens into the North Sea. Consequently, the GNSS receiver records sea-water reflections only from the south, and it is operating under the responsibility of the Active GPS Reference System for the Netherlands organisation. It is co-located with a tide gauge (TG) installed only a few meters away and administrated by the National Institute for the Coast and Sea (Rijks Instituut voor Kust en Zee) of the Netherlands.

Vlissingen station is known under the abbreviation VLIS. The TG started to operate in 1996, and the GNSS receiver was installed later in 2006. Since then, the receiver and the antenna have been replaced multiple times. The most modern version of the assembly includes a double-frequency Leica GR50 receiver and a Leica AR25 antenna, which is installed on a 6.5 m monument. Both devices are high quality and specially designed for high-precision geodetic applications. All equipment is connected to a master computer for real-time status monitoring and data access.

Figure 6.1: **Left:** Bird's eye view of the wider area of Vlissingen, the Netherlands. The yellow line denotes international borders, and the white dots show the major cities. The position of the station is highlighted with a red dot (Acquired from Google Earth[1]). **Right:** GNSS antenna installed in the marina, on a 6.5 m monument (Viewing angle in the southeast direction, rendered from Royal Observatory of Belgium[2]).

6.2.2 Roscoff Station

Roscoff station (Figure 6.2) is situated in the marina of the homonym commune of Brittany in northwestern France. The commune is built on a small cape, and the facilities face the English Channel to the east. The set-up is identical to the Vlissingen station; a GNSS receiver is installed next to the sea and co-located with a TG. The University of La Rochelle is responsible for operating the GNSS receiver. In contrast, the TG is administrated by the Naval Hydrographic and Oceanographic Service (Service Hydrographique et Océanographique de la Marine) of France.

Roscoff station is known under the abbreviation ROTG. The TG was installed in 1973, and the GNSS receiver is significantly newer because it started to operate in 2009. This assembly has been replaced once; the latest version includes a double-frequency Septentrio PolaRx5 receiver and a Trimble Zephyr Geodetic antenna. However, when the measurements were acquired, the

[1] https://www.google.com/intl/en/earth/. Accessed: 05.08.2021

[2] https://www.epncb.oma.be/_networkdata/siteinfo4onestation.php?station=VLIS00NLD. Accessed: 05.08.2021

equipment was a double-frequency Topcon GB-1000 receiver and a Topcon PG-A1 antenna. The antenna was installed on a 3 m steel mast in both cases.

Figure 6.2: **Left:** Bird's eye view of the wider area of Roscoff, France. The light-blue line denotes national borders, and the white dots show the major cities. The position of the station is highlighted with a red dot (Acquired from Google Earth[3]). **Right:** General overview of the marina, where the GNSS receiver and the TG are installed (Viewing angle in the south direction , photo taken by E. Poirier- University of La Rochelle[4]).

6.3 Experiment Results and Discussion

The reflectometry solutions are validated against the time series that the TG obtains. This comparison cannot be performed directly because the measurements from the TG and the GNSS-R method are not provided at the same time intervals. Since the data are not homogeneous in the time domain, the most sophisticated method is to estimate the parameters of the tide coefficients for each data set and calculate new time series at the same time intervals according to them. In this case, RMSE is the only evaluation index. As long as the same mathematical model is used to parametrize all data sets, the correlation is expected to be very high anyway, and it would not be very sensible to use it as a criterion. Lastly, all figures and graphs in this section utilize the same constellation abbreviations with Section 5; G and R indicate GPS and GLONASS, respectively.

The measurements at Vlissingen station were acquired between January 1 and September 30, 2020. This interval is long enough to determine short-period coefficients, but it is insufficient to estimate semi-annual and annual cycle parameters accurately. This station's maximum tidal oscillation does not exceed three meters above or below the mean sea level. This fact allows for comparison between the data sets because the range is significantly greater than the accuracy

[3]https://www.google.com/intl/en/earth/. Accessed: 07.08.2021
[4]https://www.sonel.org/spip.php?page=gps&idStation=1933. Accessed: 07.08.2021

of the measurements. The evaluation of the sea-level monitoring is carried out according to the estimated amplitudes and phases of the major components, as described in Section 6.1 (cf. Table 6.1). The phases of the coefficients that yield high amplitudes, namely M_2, S_2, and N_2, are in good accordance. The phase differences are at the 1-3° level, showing that the reflectometry time solutions coincide with the TG. On the other hand, the variations between the phases of the low-amplitude parameters are significantly higher. In extreme cases, they exceed the 40° (cf. Table 6.2), indicating that the accuracy of the observations is greater in magnitude than the observations' magnitude itself.

Coef.	**Amplitude** (m)				**Phase** (deg)			
Name	TG	G	R	G+R	TG	G	R	G+R
M_2	1.77	1.72	1.75	1.73	31.17	33.82	34.02	33.71
S_2	0.49	0.34	0.41	0.38	86.85	85.93	87.72	86.86
N_2	0.29	0.19	0.25	0.22	5.70	8.33	5.08	6.31
ν_2	0.09	0.06	0.08	0.07	2.50	344.84	354.02	349.26
2"N_2	0.03	0.02	0.01	0.01	163.31	135.64	96.95	120.12
λ_2	0.06	0.04	0.05	0.05	43.16	60.95	53.55	56.84
L_2	0.18	0.10	0.15	0.12	45.36	50.78	51.48	50.74
K_2	0.15	0.10	0.13	0.11	85.27	77.64	81.54	78.61
K_1	0.06	0.04	0.07	0.06	351.67	3.03	342.97	352.36
O_1	0.10	0.01	0.08	0.05	179.11	185.37	173.69	173.80
P_1	0.02	0.04	0.03	0.03	333.91	341.96	350.54	346.11

Table 6.2: Estimated amplitudes and phases of the principal tide harmonics for all solutions at Vlissingen station. TG, G, and R indicate the tide gauge, GPS, and GLONASS, respectively.

The time series are well aligned, but there are some deviations at the decimetre level (cf. Figure 6.3). This behaviour coincides with the harmonics analysis and, more specifically, with the

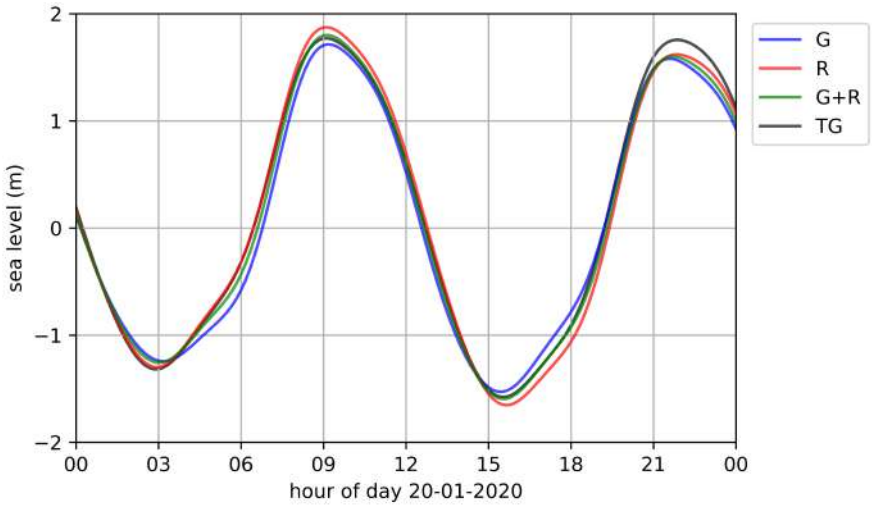

Figure 6.3: Comparison between all sea-level monitoring solutions in Vlissingen station on January 20, 2020. The abbreviations for each solution coincide with those in Table 6.2.

amplitude differences between the coefficients. Furthermore, a quantitative analysis is performed using the RMSE index between the solutions (Table 6.3). The differences between the TG and the other solutions range from 9 to 16 cm. Additionally, GLONASS and the combination of GPS and GLONASS perform better than GPS.

RMSE (cm)				
	G	R	G+R	TG
G	0	21	16	16
R	21	0	18	9
G+R	16	18	0	9
TG	16	9	9	0

Table 6.3: RMSE in cm between all solutions in Vlissingen station. The abbreviations for each solution coincide with those in Table 6.2.

The measurements from the Roscoff station were acquired throughout the entire year of 2002. Although the observations are longer than in the Vlissingen station, they are still insufficient to determine the semi-annual and annual period coefficients accurately. The amplitude of the tidal oscillation exceeds the 5 m; hence it is higher in this station, and the ratio between the sea-level observations and their noise is greater. The greatest agreement in the phace is again achieved between the coefficients with the highest amplitude, and the phase differences fluctuate at the same level (1-3°). The differences in the low-amplitude parameters also show high variability. In this case they range between 10° and 80° (cf. Table 6.4).

Coef.	**Amplitude** (m)				**Phase** (°)			
Name	TG	G	R	G+R	TG	G	R	G+R
M_2	2.69	2.21	2.58	2.42	142.35	142.59	143.57	143.26
S_2	1.00	0.53	0.77	0.67	188.61	185.33	189.22	187.75
N_2	0.53	0.24	0.39	0.32	124.10	122.00	125.76	124.18
ν_2	0.10	0.04	0.07	0.05	114.40	98.86	115.07	135.32
2"N_2	0.08	0.03	0.04	0.03	118.30	68.66	113.14	103.72
$lambda_2$	0.04	0.01	0.08	0.05	117.23	131.65	150.02	146.11
L_2	0.12	0.04	0.11	0.07	131.50	147.84	144.68	146.78
K_2	0.28	0.11	0.19	0.14	186.69	222.51	190.26	197.36
K_1	0.08	0.09	0.07	0.07	82.21	42.18	85.79	67.46
O_1	0.07	0.13	0.04	0.08	333.52	323.55	328.72	325.04
P_1	0.03	0.06	0.02	0.03	72.72	25.28	103.40	46.23

Table 6.4: Estimated amplitudes and phases of the principal tide harmonics for all solutions at Roscoff station. TG, G, and R indicate the tide gauge, GPS, and GLONASS, respectively.

In comparison with the previous station, the performance of each constellation is slightly different. Despite the alignment of the time series, there are considerable offsets (cf. Figure 6.4). Regarding the RMSE evaluation, the performance of the reflectometry method in this station is twice as bad. The reference solution and the reflectometry ones span between 17 and 39 cm. Finally, the combination of GPS and GLONASS again yields the best results, but GLONASS surpasses GPS (cf. Table 6.5).

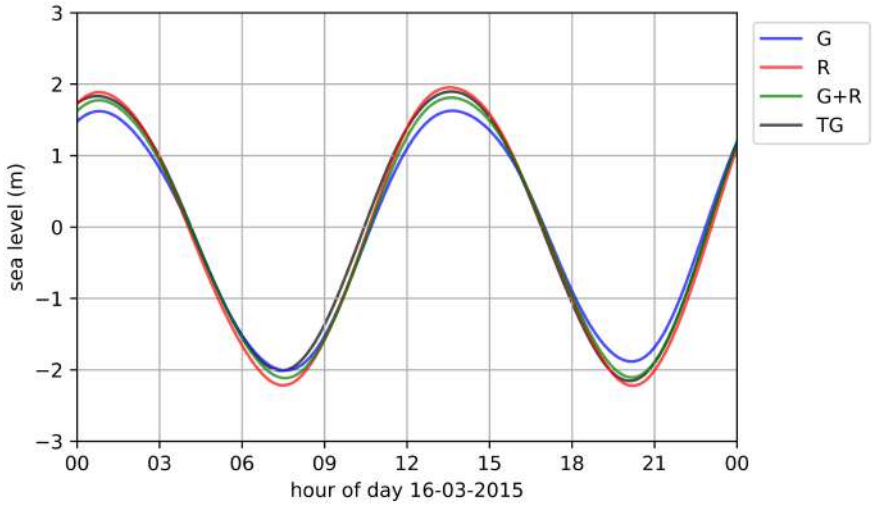

Figure 6.4: Comparison between all sea-level monitoring solutions in Roscoff station on March 16, 2015. The abbreviations for each solution coincide with those in Table 6.4.

RMSE (cm)				
	G	R	G+R	TG
G	0	60	26	39
R	60	0	40	23
G+R	26	40	0	17
TG	39	23	17	0

Table 6.5: RMSE in cm between all solutions in Roscoff station. The abbreviations for each solution coincide with those in Table 6.4.

6.4 Conclusions

This chapter demonstrates the capabilities of the GNSS-R methodology for monitoring level changes in water bodies. Data from two seafront stations are analyzed for the evaluation of the technique. Both sites are located on the European side of the Atlantic Ocean and are subject to high-amplitude tides. The datasets are not referred to the same period and cover a maximum period of one year.

The algorithm for calculating the water level is a simplified version of the one developed for the soil-moisture application. It allows for the exploitation of all constellations and carrier frequencies in parallel or independently, and it does not require calibration. The experiment results indicate good agreement with the higher-magnitude tidal coefficients, which is reduced when considering lower-order harmonics. The coincidence with the reference TG datasets is up to the sub-decimetre level, and the higher ambiguity is remarkably advantageous for the quality of the solution. Moreover, there are significant accuracy differences between the results of the two stations. Assuming that the TG data are of similar quality, the sea-surface conditions (e.g. roughness) also influence the GNSS-R series.

Chapter 7

Soil-Moisture Estimation in Northwestern Argentina

One of the main goals of this dissertation is the observation of the hydrological cycle in northwestern Argentina with GNSS remote-sensing techniques. Soil moisture is a key element of this process; thus it is decided to employ the methodology described in Chapter 5 in three ground stations in the province of Salta. Despite the successful evaluation of the soil-moisture algorithm, this experiment is very challenging because the climate conditions that characterize those locations are totally different from those in the previous experiment.

7.1 Stations Description

The GNSS ground stations were explicitly installed for this study by the GFZ and the University of Potsdam (UP). Two facilities are located in privately owned properties in Tolombon and Payogasta villages, while the third is installed in Pozuelos Salar, inside an open lithium mine. The altitude of the facilities spans between 1667 and 3760 m asl, and they are characterized by only two distinct seasons rather than four. In addition, the highest soil-moisture values occur in the summer, when most of the rain events occur (cf. Chapter 2.2). Furthermore, although the sites of this experiment are situated at a relatively short distance, there are differences between each other. The stations in Tolombon (CAFJ - 1667 m asl) and Payogasta (CACN - 2453 m asl) experience higher rainfall rates than in Pozuelos (PUNJ - 3760 m asl) (cf. Figures 7.1 and 7.2).

Each station is equipped with different quality GNSS receivers to evaluate their performance. Moreover, TDR sensors are used for comparison, and metrological information is retrieved either from in-situ or nearby stations. The measurements extend through three years, starting in March 2019, and ending in October 2021. The calibration period, when the appropriate reflections are selected, takes place over the first 12 months of the observations, while the rest of the period is used for the evaluation of the results.

As suggested in Chapter 5, the superior solution is the one that takes into account all constellations and frequencies. Thus, only this combination is examined. Furthermore, unlike the former soil-moisture experiments, it is possible to access independent soil-moisture data for the absolute referencing of the time series. In fact, instead of key values of the TDR sensors, observations from the Argentine satellite SAOCOM (Giraldez, 2003) are introduced in the least-squares

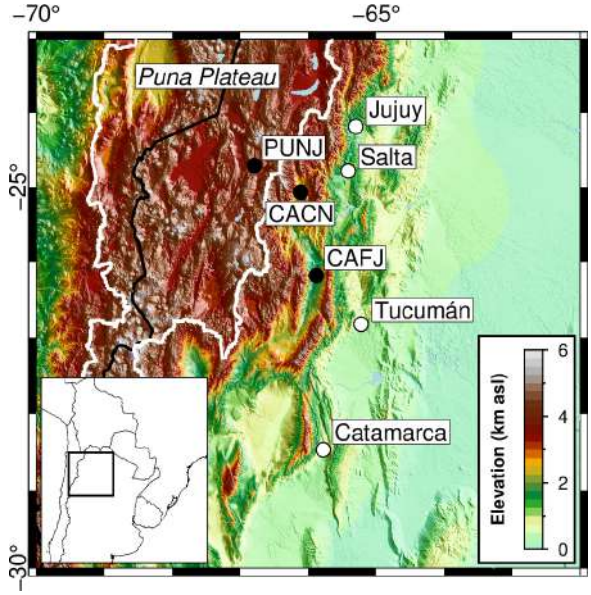

Figure 7.1: Topographic setting of the South-Central Andes with the three GNSS stations (black dots) installed during this campaign. The white dots indicate the major cities of the area. The white line delineates the extremely arid Central Andean Plateau, and international borders are drawn by the black lines (Topography data obtained from ETOPO1 (Amante, 2009)).

adjustment as fixed values. As a result, this product's accuracy and spatial resolution are very high, but its temporal is only 28 days. Thus the fusion of both methods can yield a high-quality product in terms of accuracy as well as temporal resolution. Furthermore, the evaluation of the results is more legitimate because the comparison is held against a third external source, which is not correlated with the GNSS-R or the satellite methodology.

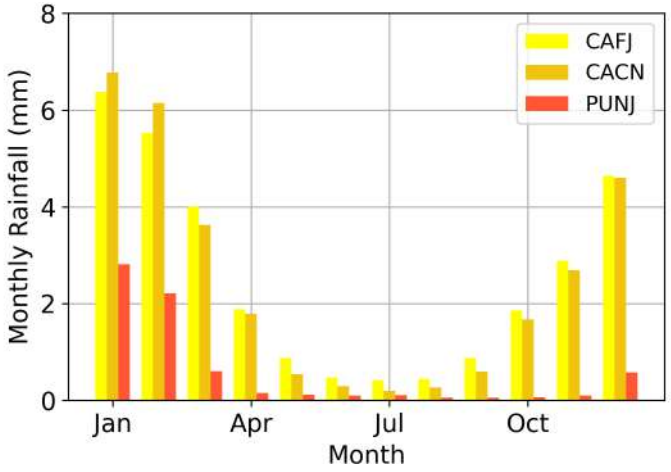

Figure 7.2: Mean monthly total rainfall of the CAFJ, CACN, and PUNJ stations (Meteorological information retrieved from Hersbach et al., 2020 - ERA5-Land monthly averaged data from 2000 to 2020).

Apart from some modifications, all stations were built according to the same concept. A Linux-based computer with no graphical interfaces is connected with a geodetic and a low-cost GNSS receiver, as well as with a meteorological sensor, when available. The model of the geodetic receiver varies, while the low-cost one is always a Geostar GeoS-5M. Unfortunately, the latter stopped operating properly due to technical issues and did not provide sufficient observations to analyze. The primary utilization of the computer is the execution of terminal commands for controlling the flow of the data and the storage of the observations in internal and external hard drives. Moreover, the computer can reinitialize in the case of long-period interruption of the measurements. The TDR-FDR sensors operate independently of the computer. The logger runs an in-house developed, low-level algorithm that controls the acquisition of the observations through the probes buried in two distinct depths. The first set of five detectors was placed at a shallow depth of 5 cm, and the second set of four detectors was buried at 10 cm depth. Additionally, photovoltaic panels are used in Payogasta and Pozuelos sites because there is no access to the electrical grid. Combined with a car battery, frames of 400 W total peak power are sufficient to provide energy to the assembly on a 24-hour basis. Except for the sensors, all devices are stored in a metal box to avoid exposure to rain and dust. Furthermore, the metal box includes a ground wire for lightning protection.

Figure 7.3: Equipment assembly of the station in Pozuelos. The instrumentation includes a TDR-FDR logger, a computer, a Javad Delta TRE-G3T multi-frequency and multi-constellation geodetic receiver, a battery (top to bottom order), a Geostar GeoS-5M low-cost receiver (top left), and a solar charge controller (bottom right).

7.1.1 Tolombon

Tolombon station (Figure 7.4) is situated on a private property close to the homonym village on the southern border of the province of Salta, Argentina. The landscape is very good for reflectometry because the terrain is flat, and there is no vegetation except for some small and low-density bushes. The direct vicinity of the antenna is clear from tall constructions, which allows all reflections to be recorded. At last, the facility has direct access to the electricity network. Even though the energy supply is not very stable in this area, there were no significant and long-period blackouts that could lead to substantial data loss.

The regolith exhibits typical callus characteristics under sidewall deposition conditions where the hydrographic system's carrying capacity changes sharply. The coarseness is not clearly distributed. There is presence of both coarse and fine-grained material, with the latter predominating due to the considerable distance from the morphological alteration. From a mineralogical point of view, the mixture is relatively undefined. The predominance of carbonates is clear, but the existence of silicates is also strong. This is supported by the presence of granitic formations and crystalline schists in the area, with the latter carbonates being dominant.

The installation of the equipment took place from 14 to 16 March 2019. It included the excavation for the electricity cables and the TDR-FDR probes, the stable positioning of the pole on a concrete base, and the installation of all devices in a metal box. The most labour-intensive operation was the excavation, and it occupied more than 60 % of the time. This station is equipped with a Javad Delta TRE-G3T multi-frequency and -constellation geodetic receiver, a Javad GrAnt-G3T antenna, a Vaisala WXT520 weather sensor, and a series of Truebner SMT 100 TDR-FDR probes connected with a Campbell CR800 data logger.

Figure 7.4: Tolombon station. **Left:** GNSS and meteorological equipment installed on a 2 m pole. The metal box includes all necessary instrumentation (Looking angle in the north direction). **Right:** Soil vertical profile and two TDR-FDR probes arranged at distinct depths. In the photo is shown the top-layer soil composition, including the organic matter, the different size granules, and pebbles.

7.1.2 Payogasta

Payogasta station (Figure 7.5) is located in the Valles Calchaquíes, between Cachi and the homonym villages. The field is privately owned, and it was offered for the study because it is not exploited. Besides the southeast corner, the field has nearly zero inclination and is partially covered with low pasture. Although there are no constructions adjacent, some hills east of the antenna are masking the low-elevation reflections up to 10 deg. However, this disadvantage is of minor importance because the cliffs do not encompass the entire azimuthal range, and the GNSS receiver dumps by default all observations originating up to 7 deg. Furthermore, the area has no

direct access to the electricity network.

Typical fluvial deposits characterize the regolith in Payogasta. The coarse grain-size distribution and the rounded geomorphology of the strains (conglomerates) make up the picture. The bedrock that trophicizes the valley is mainly composed of siliciclastic and plagioclastic sandstones (Payogastilla Group). In many cases, carbonate binders are present. The presence of phyllosilicate orthocrysts is also evident, and its slightly reddish colour is probably due to the presence of iron oxides. The origin of the iron may be from the phyllosilicate minerals or volcanic intrusions occurring in the outcrops. These vein systems often reach the surface, while the presence of a gaseous system in the past is definite. These systems locally deposit sulphur and sulphur compounds.

The equipment was installed between 17 and 18 March 2019. The labour work included the same tasks as the Tolombon station, apart from connecting with the electricity grid. The use of solar panels facilitated the operations in terms of time and effort. An other difference between the two stations is the use of a Novatel SMART-V1G single-frequency geodetic receiver, which provides signal strength measurements with lower numerical resolution (1 instead of $0.25\,\mathrm{dB-Hz}$). Considering the similar climatological conditions and the comparable development level of the soil, this set-up allows for direct comparison between the two receiver types. Lastly, even though the National Institute of Agricultural Technology of Argentina (Instituto Nacional de Tecnología Agropecuaria, 2022) had installed a meteorological station close to the site, it was impossible to exclusively use this source because of data losses. Thus, measurements from the Global Precipitation Measurement mission (Huffman et al., 2019) were adjusted to the rain gauge to cover the entire period of observations.

Figure 7.5: Payogasta station. **Left:** GNSS antennas attached on a 2.5 m pole, as well as solar panels installed for energy supply. The metal box includes all necessary instrumentation (Looking angle in the southeast direction). **Right:** Soil vertical profile and a TDR-FDR probe placed at 5 cm depth. The development level of the soil is comparable with Tolombon station (cf. Figure 7.4).

7.1.3 Pozuelos

The station of Pozuelos (Figure 7.6) is found in Altiplano-Puna Plateau, 230 km west of the city of Salta and 150 km from the Argentina–Chile border. The field is part of an open lithium mine within the homonym salar, and Litica Resources SA is exploiting it. The area is totally flat, and the vicinity is free of substantial natural obstacles that mask the reflections. On the other hand, the location is very remote, several kilometres from the mine campus. Furthermore, as there is extra equipment from the mining company, the complex is enclosed by a wire fence for security. Lastly, the closed point with energy supply is the campus; hence, access to this source was not possible.

The salars have particular characteristics in terms of their minimally-developed regolith. The sedimentation that takes place is almost exclusively chemical, while the vicinity's geomorphology indicates no significant deposition of new material. The result is that the main component is dominated by evaporite bedrock with a relatively intermediate grain size due to the distance from the central parts of the lake. There are also apparent small amounts of aeolian deposits, mainly sandy in grain size, with the primary material supply from the carbonaceous marine sedimentary rocks. The mineralogy of this area is not defined because the composition varies considerably from place to place.

The operations for the installation of the equipment lasted three days, from 20 to 22 March 2019. The excavation was the most challenging aspect of this work because the soil of this salar is always very dry and compact and requires additional effort to process it. Furthermore, the

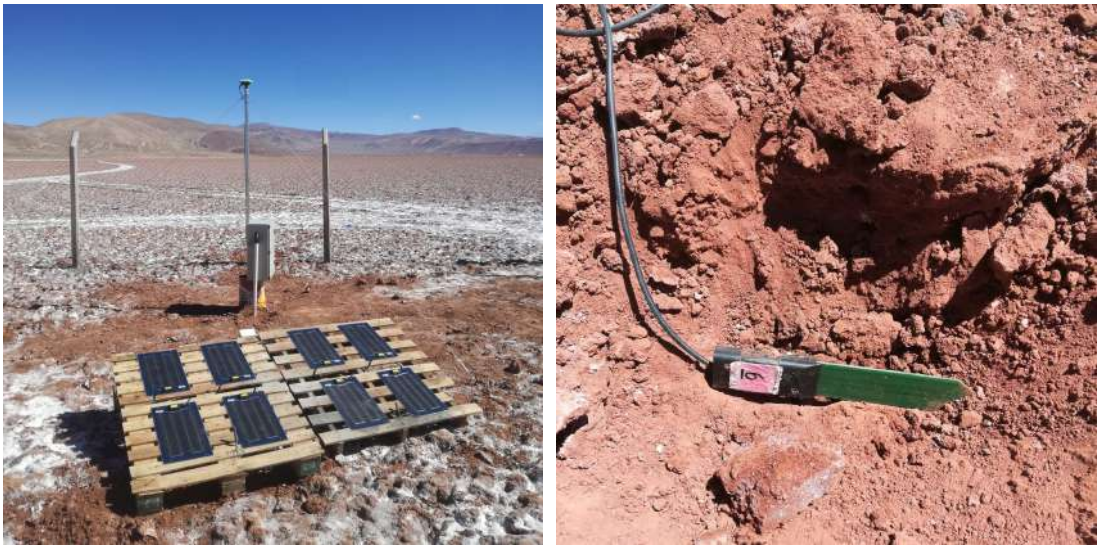

Figure 7.6: Pozuelos station. **Left:** Detailed overview of the base, where the GNSS is installed along with additional sensors, used for the mining operations. The antenna is attached on a 2.5 m pole, the solar panels are installed for energy supply, and the metal box includes all necessary instrumentation (Looking angle in the southeast direction). **Right:** Soil vertical profile and a TDR-FDR probe placed at 10 cm depth. In the photo are shown the soil granules, as well as the formatted rock salts.

GNSS and TDR-FDR instruments are identical to the Tolombon station, and whereas was no need to install a meteorological sensor because the mining company could provide that data through their equipment. Finally, this station's location was explicitly chosen to compare the performance of same-model quality receivers under varying environments.

7.2 Experiment Results

The results from the station in Tolombon generally indicate very low soil-moisture values of 3-3.5 v/v % during the austral winter that rise sharply in the rainy season. Therefore, there is good agreement between the reflectometry solution and the TDR-FDR series. Nevertheless, the behaviours of the data sets are different. Upon rainfall episodes, the TDR-FDR one yields sharp soil-moisture peaks that decay smoothly and rapidly. On the other hand, the GNSS-R data set does not always drop immediately and is noisier. Moreover, some rainfall events during November-December 2020 are not well recorded by the reflectometry solution. In addition, there are some cases (e.g. May-June 2021) when both sources point out a soil-moisture increase without recording rainfall. Added to this, the decay's shape is different from the post-rain events. For the integrity of this statement, the rain gauge measurements were inter-compared with satellite data from the Global Precipitation Measurement mission (Huffman et al., 2019). Lastly, all observations of the SAOCOM are found in the last third of the GNSS-R time series and show minor differences, less than 5 v/v %, against the TDR-FDR data.

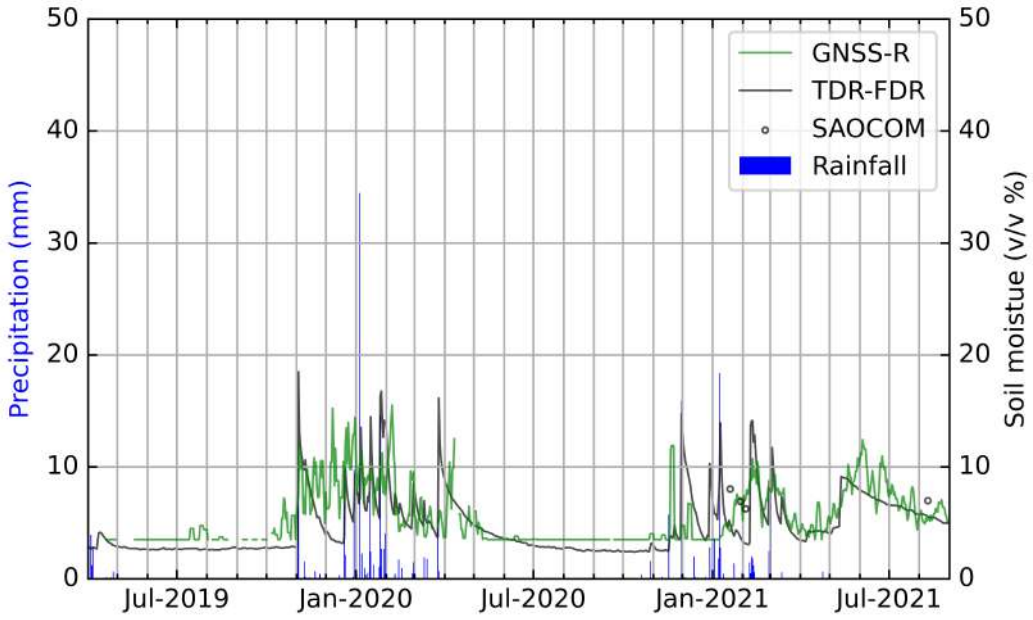

Figure 7.7: Soil-moisture estimation in the CAFJ station between April 2019 and August 2021. The reflectometry solution takes into account all constellations, and the series were fixed using absolute soil-moisture values from the Argentine Microwaves Observation Satellite (Satélite Argentino de Observación con Microondas - SAOCOM) (Giraldez, 2003).

From the statistical point of view, the correlation between GNSS-R and TDR-FDR is moderate

(0.59), while the RMSE is very low (2.4 v/v %). Moreover, compared to the previous experiments (cf. Chapter 5), the correlation is remarkably lower, whereas the RMSE stands at the same levels. This indicates specific time frames that yield inconsistent results.

The station in Payogasta produces similar-behaviour soil-moisture series to those from Tolombon. There are pronounced peaks associated with the wet season, while fairly low values mark the other epochs. Furthermore, there are certain epochs when the performance of the GNSS-R solution does not respond optimally to rainfall events (e.g. November-December 2020). In contrast, the decay rates of the two sources are more uniform, and no soil-moisture peaks occur without the presence of rain. The reflectometry series produce significantly higher soil-moisture readings during the austral summer of 2019-2020. Unlike the following year, when the observations are comparable, this season is characterized by extended rainfall that amplifies the divergence. The SAOCOM observations are again detected in the end. In general, the agreement is at the level of 5 v/v %. There is only one exception when the variation doubles.

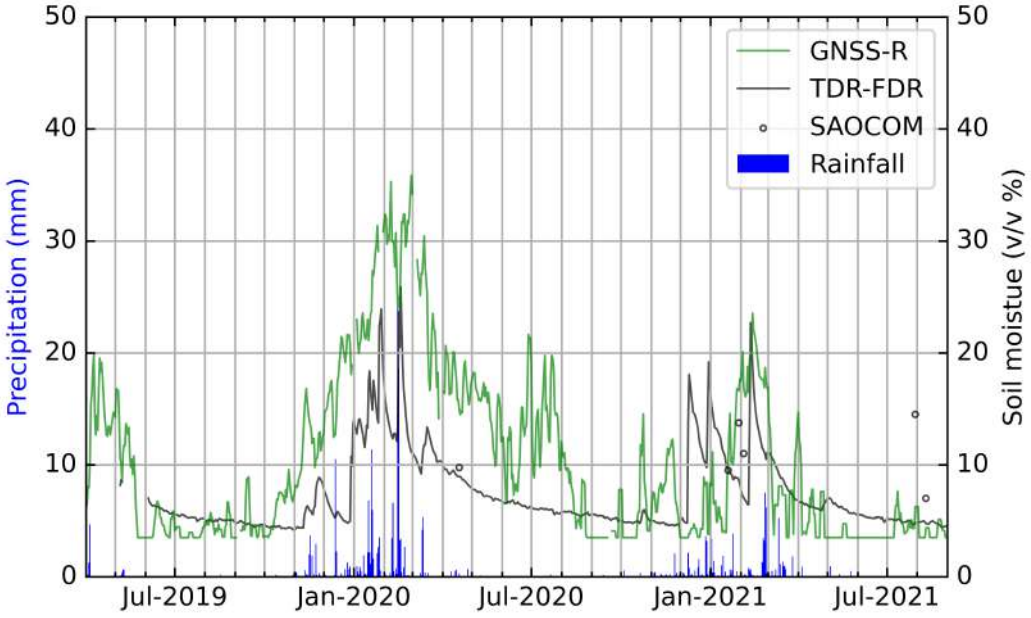

Figure 7.8: Soil-moisture estimation in CACN station between April 2019 and August 2021. The reflectometry solution takes into account all constellations, and the series were fixed using absolute soil-moisture values from the Argentine Microwaves Observation Satellite (Satélite Argentino de Observación con Microondas - SAOCOM) (Giraldez, 2003) (Rainfall information was retrieved by combining local meteorological data with observations from the Global Precipitation Measurement mission (Huffman et al., 2019)).

The statistics of the station in Payogasta show worse performance than the ones from Tolombon. Despite the fact that the correlation is of similar quality (0.61), the RMSE is 2-3 times worse (6.69 v/v %). This decline occurs due to the lower numerical resolution of the utilized receiver. Finally, compared with the previous experiments in Chapter 5, the rainfall shows a higher coincidence with the soil moisture. This demonstrates distinct hydrological mechanisms because of the more arid conditions.

The station in Pozuelos Salar illustrates a different behaviour than the previous facilities. The soil moisture rises sharply at the beginning of the wet season and drops gradually to the lowest value just before the following year's rainfall events start. In addition, the readings in this station are higher, despite the drier climate. Comparing the tied-to-the-SAOCOM GNSS-R series with the TDR-FDR ones, although the decay rates are comparable, the responses to the rain are not analogous. The prior is significantly more sensitive, leading to a maximum soil-moisture variation of 40 v/v %. This difference is abnormal and cannot be justified by the non-identical approximations of each methodology. Moreover, light rainfall events (e.g. August 2020) may trigger soil moisture instantaneously. With respect to the SAOCOM measurements, in most cases, they are well aligned with the GNSS-R series, except for one instance when the divergence surpasses the level of 3.5 v/v %.

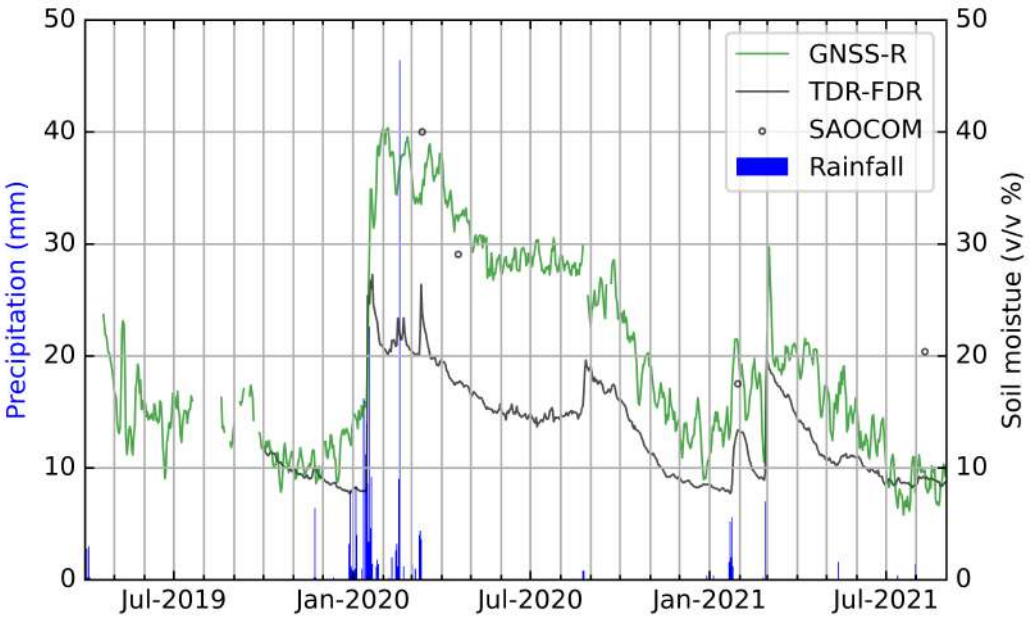

Figure 7.9: Soil-moisture estimation in PUNJ station between April 2019 and August 2021. The reflectometry solution takes into account all constellations, and the series were fixed using absolute soil-moisture values from the Argentine Microwaves Observation Satellite (Satélite Argentino de Observación con Microondas - SAOCOM) (Giraldez, 2003).

The statistical analysis of this station suggests a very high correlation with the TDR-FDR method (0.89) but poor RMSE performance (9.22 v/v %). This occurs due to the significant offset of the SAOCOM readings, which is not constant throughout the period of the observations and depends on the amount of rainfall. In combination with the visual comparison of the series (cf. Figure 7.9), this evaluation exemplifies the influence of the salinity and indicates better calibration to achieve more consistent results.

7.3 Conclusions

This chapter examines the modernized GNSS-R soil-moisture methodology under unique soil and climate conditions. The ground stations were installed in locations where the soil is subject to erosion, is not compact, and does not follow the typical stratification with discrete layers (cf. Figure 2.3). Moreover, the climate in this area is characterized by extremely dry conditions and seasonal rainfall between November-March. Finally, this test case is special because the reflectometry series were calibrated with third-party data and not the TDR-FDR observations. Considering the results from the three stations, the following conclusions are drawn:

- The time series of the stations in Tolombon and Payogasta reflect the impact of high-porosity soils on this technique. They designate higher-noise solutions and lower quality in terms of correlation and RMSE, and GNSS-R cannot always respond appropriately after rainfall. In addition, the single-frequency receiver performs worse.
- The station in Pozuelos Salar demonstrates the effect of high salinity. Considering that this zone is one of the most arid places on the Earth, all sources yield unreasonably high soil-moisture readings. However, the SAOCOM measurements are considerably higher, illustrating the necessity for calibration.
- There are some cases when soil moisture rises despite the absence of rain. Additionally, this behaviour is reported by all sources with a high agreement. However, given the long temporal extent and the smooth decay rate of this reaction, the cause may be related to near-surface atmospheric processes (e.g. humidity) and must be further investigated.

Chapter 8

Water-Vapour Analysis in Northwestern Argentina

This chapter is complementary to Chapter 7 and is referred to the same area of study. The main research topic is the analysis of water vapour and builds on the investigation published in Antonoglou et al. (2022b). The goals are to examine the impact of the topography and understand the acting mechanisms for the association of the water vapour fluctuations with the precipitation events in this area. Finally, in this investigation, the ZWDs and their gradients are considered. The prior gives information about the water vapour, while the latter indicates the azimuthal direction, to which the wet delay is greater.

8.1 Data Collection

This study combines GNSS measurements from ground stations in northwestern Argentina and ERA5 reanalysis data (Hersbach et al., 2020). The analysis period extends between 2010-2021, and it is mainly restricted by the accessibility to the GNSS observations.

8.1.1 GNSS Network

In line with the study demands, the GNSS measurements were collected from a network of 23 stations (Figure 8.1). The majority of the stations are situated in northwestern Argentina (16), but there is a small fraction of the facilities located in Chile (4) and Bolivia (3). The sites cover an altitude range between 198 and 5451 m asl and extend from the mountain front to the core of the Central Andean Plateau. The span of this network exceeds the 700 and 450 km in the east-west (E-W) and north-south (N-S) directions, respectively. This distribution is ideal for the study because the area's topography is diverse, and the transition between completely distinct climate conditions is sharp. In order to monitor variations along the topographic gradient, seven stations are explicitly examined. Four sites lie along the E-W cross-section (UNSA - 1224 m, GOLG - 2343 m, SRSA - 3113 m, and SALC - 3799 m asl), and an other set of four sites lie along the N-S one (UNSA - 1224 m, TUCU - 456 m, JBAL - 381 m, and CATA - 518 m asl), while both sets share a common station. Additionally, there is the availability of high-quality meteorological information for three stations which are located in various altitudes (UNSA - 1224 m, CAFJ - 1667 m, and PUNJ - 3760 m asl).

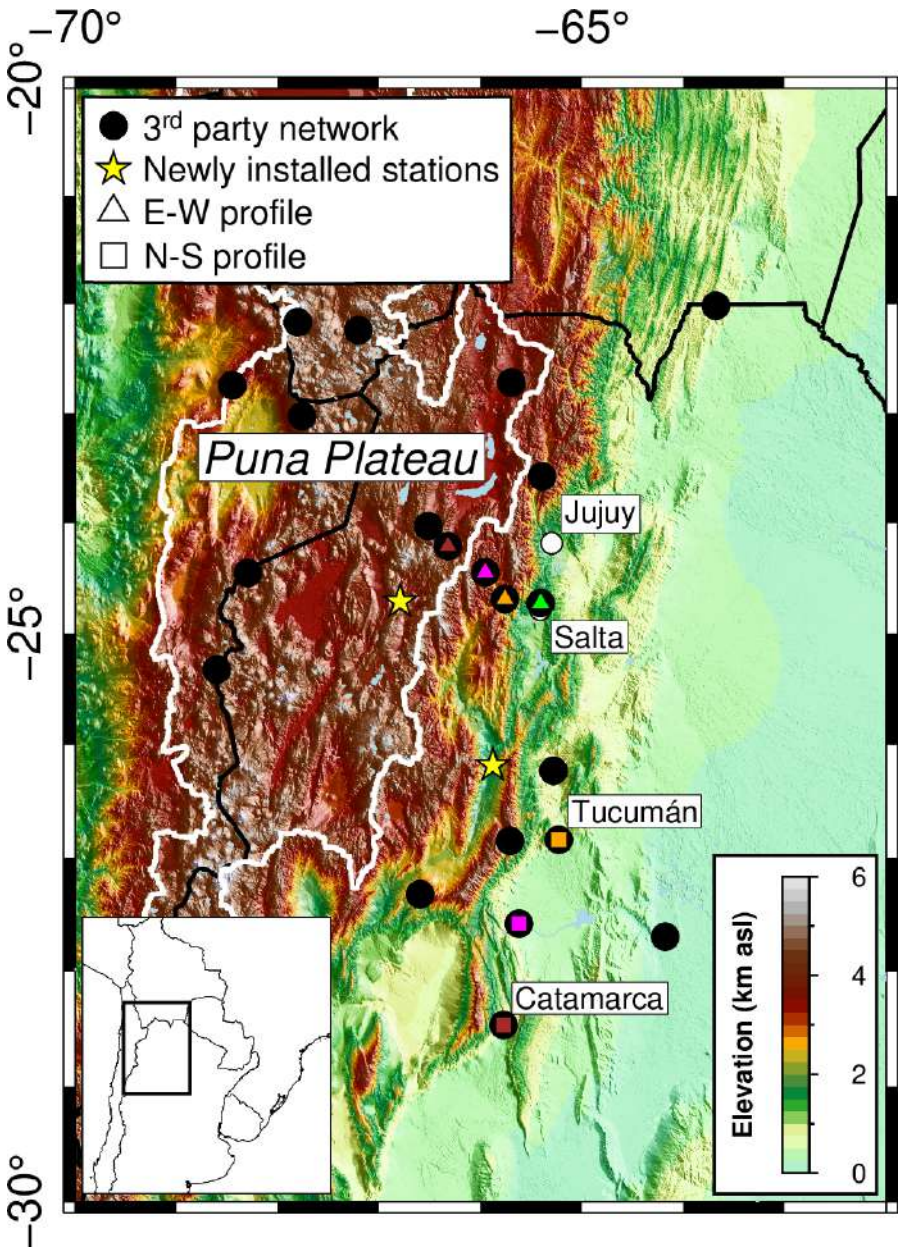

Figure 8.1: Topographic setting of the study area in the South-Central Andes, including the locations of the GNSS ground stations. The black dots point out the stations that third-party organizations installed, and the yellow stars point out the stations that were exclusively installed for this study. The inner triangles and the squares indicate the subsets along the east-west (E-W) cross-section (UNSA, GOLG, SRSA, and SALC) and in parallel with the Andes in the north-south (N-S) direction (UNSA, TUCU, JBAL, and CATA), respectively. UNSA, GOLG/TUCU, SRSA/JBAL, and SALC/CATA are illustrated with green, orange, magenta, and brown colour, respectively. The white line delineates the extremely arid Central Andean Plateau. The white dots show the area's major cities, and the black lines show international borders (Topographic data obtained from ETOPO1 (Amante, 2009)).

The GNSS network is not homogeneous; it consists of various sets of stations operated independently by different third-party organizations. The stations CAFJ and PUNJ are already described in Chapter 7, while the GFZ was responsible for processing their observations for water-vapour estimation. On the other hand, the rest of the sites were either installed by the Argentine National Geographic Institute (Instituto Geográfico Nacional) (Piñón et al., 2018) or UNAVCO (Simons et al., 2010a,b; Pritchard, 2010a,b, 2011, 2012; Smalley and Bennett, 2015a,b,c,d,e,f,g). The analysis of those observations is exclusively carried out by Blewitt et al. (2018) from the Nevada Geodetic Laboratory, and the results are released publicly for further processing[1].

Station Name	**Latitude**	**Longitude**	**Height** (m)	**Source**	**Analysis Centre**
ABRA	22°43'19.32"S	65°41'50.31"W	3530.10	IGN	NGL
ALUM	27°19'24.33"S	66°35'47.86"W	2736.94	IGN	NGL
CAFJ	26°10'51.22"S	65°52'49.17"W	1702.36	GFZ/UP	GFZ
CATA	28°28'15.54"S	65°46'26.83"W	547.15	IGN	NGL
CBAA	22°44'46.92"S	68°26'53.33"W	3514.84	UNAVCO	NGL
CJNT	23°01'38.96"S	67°45'38.06"W	5074.05	UNAVCO	NGL
COLO	22°10'02.57"S	67°48'14.32"W	4376.93	UNAVCO	NGL
GOLG	24°41'26.11"S	65°45'38.80"W	2381.15	UNAVCO	NGL
JBAL	27°35'03.86"S	65°37'21.89"W	409.16	IGN	NGL
LCEN	25°19'33.81"S	68°36'09.36"W	4270.94	UNAVCO	NGL
PUNJ	24°42'46.96"S	66°47'37.27"W	3802.58	GFZ/UP	GFZ
SALC	24°12'47.11"S	66°19'20.83"W	3841.62	UNAVCO	NGL
SOCM	24°27'16.60"S	68°17'42.59"W	3969.45	UNAVCO	NGL
SRSA	24°26'59.24"S	65°57'11.85"W	3153.80	UNAVCO	NGL
TAVA	26°51'10.72"S	65°42'36.02"W	2036.74	IGN	NGL
TERO	27°41'57.30"S	64°10'42.17"W	222.63	IGN	NGL
TIL2	23°34'37.70"S	65°23'42.26"W	2517.78	IGN	NGL
TRNC	26°13'48.77"S	65°16'55.82"W	816.08	IGN	NGL
TUCU	26°50'35.71"S	65°13'49.26"W	485.02	IGN	NGL
TUZG	24°01'53.82"S	66°30'59.56"W	4338.67	UNAVCO	NGL
UNSA	24°43'38.84"S	65°24'27.51"W	1257.79	IGN	NGL
UTUR	22°14'31.21"S	67°12'19.94"W	5184.09	UNAVCO	NGL
YCBA	22°01'01.56"S	63°40'47.94"W	659.66	IGN	NGL

Table 8.1: Geographic coordinates of the stations that constitute the network utilized for the water-vapour analysis. The column **Source** shows the corresponding institutions/organizations that maintain the stations, which are the Argentine National Geographic Institute (Instituto Geográfico Nacional - IGN), the German Research Centre for Geosciences (Deutsches GeoForschungsZentrum - GFZ), the University of Potsdam (UP), and UNAVCO. The column **Analysis Centre** indicates the institution that processed the raw data, either the Nevada Geodetic Laboratory (NGL) or the GFZ.

Because of the gradual development of the GNSS network during independent campaigns, there is no complete temporal overlap between the observations of all stations (cf. Figure 8.2). As a result, the time series of only six stations cover the entire time frame between 2010-2021. Moreover, all stations experience data loss for brief periods owing to technical issues.

[1] http://geodesy.unr.edu/. Accessed: 29.09.2022

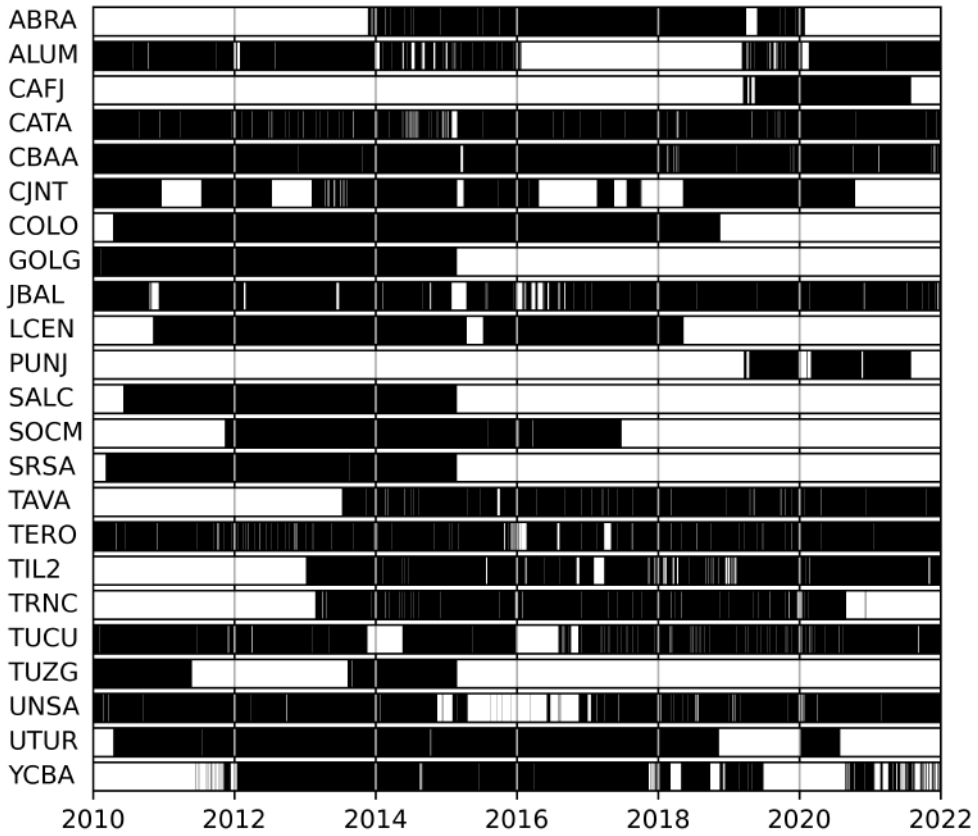

Figure 8.2: Data availability indicated by black areas of the 23 stations that are utilized for the water-vapour analysis.

8.1.2 ERA5 Reanalysis Data

Atmospheric-refractivity information on pressure levels obtained from the ERA5 reanalysis data set from the European Centre for Medium-range Weather Forecasting (Hersbach et al., 2020). This collection provides data from 1979 to the present at a native spatial and temporal resolution of 0.25° and 1 hour, respectively. The main advantages of the ERA5 data set are the extended temporal coverage, the minimal-lag update of the data, and the fact that it provides multi-layer information up to the altitude of 80 km via 37 pressure levels. Lastly, the data series were linearly resampled to a 5-minute temporal resolution to align with the GNSS data.

8.2 GNSS Observations Processing

The basic principles for estimating water vapour with GNSS observations are described in Section 4.2.2. This section provides information about the software packages that are used, and it addresses the strategy that is utilised to exploit data from different sources. The methodology needs to be explicitly explained because, even though all GNSS software use algorithms that are based on the same principles, detailed knowledge of their approximations is essential for the accurate processing of their results. Additionally, the calculation of the ZWDs and their gradients

requires information about the refraction that occurs by the dry elements of the atmosphere. Those data are calculated with ray-tracing algorithms.

8.2.1 Earth Parameter and Orbit System

Earth Parameter and Orbit System (EPOS) is a collection of GNSS software packages developed in the GFZ (GFZ German Research Centre for Geosciences, 2021). The development of EPOS started in the 1990s, and its core functions are related to precise orbit determination of various satellite missions, but they are not limited to this. This software can provide Precise Point Positioning solutions in a near real-time mode that estimate the STDs (Gendt et al., 2004; Douša et al., 2018). Even though this approximation requires plenty of information for the pre-processing, it is superior to the network solutions because it examines each station independently and demands fewer computation resources. In this software, the slant delays are projected to the zenith using the Global Mapping Function (Böhm et al., 2006a), and the gradients are calculated with the mapping function described in Bar-Sever et al. (1998).

8.2.2 Gipsy

Gipsy is a GNSS navigation software developed by the Jet Propulsion Laboratory. Its initial version was Gipsy Proto, and it was released in the 1980s. Since then, many updates have been made, and the most modern version, which is used for the processing of this study, is GipsyX. This software allows for the simultaneous estimation of geodetic and geophysical parameters in real-time and post-processing modes. Besides its terrestrial applications, Gipsy is also utilised for orbit and clock determination of LEO satellites (Bertiger et al., 2020). Similarly to EPOS, Gipsy processes each station independently using Precise Point Positioning algorithms. Lastly, the transformation between the slant and the zenith delays is achieved with the Vienna Mapping Function 1 (Böhm et al., 2006b; Kouba, 2008), and the gradient parameters are also computed with the mapping function of Bar-Sever et al. (1998) (Blewitt et al., 2018; Bertiger et al., 2020).

8.2.3 Ray tracing

Initially, the propagation path of any electromagnetic signal between the source and the observer through the neutral atmosphere is determined via ray tracing (e.g., Nievinski and Santos, 2010; Urquhart et al., 2012; Balidakis et al., 2018; Nikolaidou et al., 2020a,b). This information is estimated as a function of position, time, azimuth and elevation angle through refractivity fields of the ERA5 reanalysis model (Hersbach et al., 2020) at the native spatial and temporal resolution. More specifically, the meteorological input parameters to this algorithm are pressure, geopotential height, temperature, and specific humidity. Even though ray-tracing processes are always complex and computationally intensive and require a plethora of input data, they yield high-quality results. More information about this approximation is given in Nievinski and Santos (2010).

The ray-tracing approximation is based on the principle that the electromagnetic signal follows the path that minimizes travel time. In this case, the optical paths are calculated by inserting refractivity information in a definite integral, where the integrand satisfies the Euler-Lagrange equation (Zus et al., 2012, 2014, 2021). The output of this process is azimuth- and elevation-angle-dependent functions that allow for the calculation of the hydrostatic and wet delay of the signal. While ray tracing is a robust method, the precision of the derivatives is analogous to the quality of the input data.

In addition to the reanalysis-model-derived ZHDs and ZWDs, ray tracing is also utilized for the estimation of the gradients of previously-mentioned scalars. In contrast to the projection to the zenith, the consistency of the mapping functions related to the gradient components is critical for the integrity of the results. Even though some studies advocate for an elevation-only-dependent mapping function ($(\sin(\epsilon)\tan(\epsilon)+0.0032)^{-1}$) (Chen and Herring, 1997), the incorporation of the wet mapping function ($m_{wet}\cot(\epsilon)$) is often applied (Bar-Sever et al., 1998). These two approximations are distinct and cannot be inter-combined (Balidakis, 2019; Kačmařík et al., 2019). Provided that both EPOS (GFZ German Research Centre for Geosciences, 2021) and GipsyX (Blewitt et al., 2018; Bertiger et al., 2020) employ the latter model, the parameters of the azimuthal mapping functions for the wet and dry gradients are consistently calculated in a least-squares adjustment.

8.2.4 Processing Strategy of Water-Vapour Estimates

The STDs for every station, epoch, and observed satellite were calculated either by the GFZ or by the Nevada Geodetic Laboratory (Blewitt et al., 2018) with EPOS (GFZ German Research Centre for Geosciences, 2021) and GipsyX (Bertiger et al., 2020), respectively. The ZWDs and the gradients of the ZTDs are estimated in a linear system of unknown variables, where the mathematical model is given by Equation 4.16. Additionally, the water vapour is calculated using the Equations 4.17, 4.18 and 4.19. Further, the ZWD gradients (or wet gradients) are calculated by subtracting the reanalysis-model-derived ZHD gradients from the GNSS-derived ZTD ones. Lastly, the estimated time series are publicly available by Antonoglou et al. (2022a).

8.3 Methodology for Analysing Water Vapour

This section provides detailed information about the analysis methods followed in the study. In order to support the initial hypothesis that the moisture circulation and the topography dictate the local climate, the investigation is held gradually. Specifically, the steps include: a) classification according to the monthly-averaged water vapour values; b) spectral analysis of the water-vapour readings; c) relation between high-precision rainfall observations and water vapour; and d) determination of the zonal moisture transport via the wet gradients.

8.3.1 K-means Stations Clustering

As a first step, the stations are classified into clusters to examine the correlation between their locations and their patterns of the monthly-averaged water-vapour values. The classification is achieved using the TimeSeriesKMeans algorithm from the Tslearn library (Tavenard et al., 2020). This special version of the K-Means algorithm for 2D time series uses the Euclidean distance to cluster the data. According to the needs of the study, this methodology is ideal because even though the water-vapour series of the same zone is subject to amplitude fluctuations, it is tuned to the same seasonal frequency, and they do not experience any time/phase shifts. Furthermore, the number of classes represents the transition from a humid to an arid environment through an intermediate zone. This hypothesis is proposed in Castino et al. (2017), and it is extendedly discussed in Section 2.2.2.

The clustering of all sites is impossible owing to the lack of temporal coverage during the entire period (cf. Figure 8.2). Thus this process the observations during 2014 from 20 sites that do not yield gaps. This fraction is sufficient for the extraction of safe conclusions because it spans a

seasonal cycle and it consists of stations that are located along the entire spectrum of the topographic gradient. Therefore, almost all facilities that belong to the E-W and N-S cross-sections are involved in this analysis.

8.3.2 Spectral Analysis

In a further stage, the spectral responses of the data series along the E-W and N-S cross-sections are analysed. The initiative for this study is the short- and long-period patterns of the raw water-vapour observations in two different altitude stations (UNSA and SALC). In a distinctive summary, during 2012, the daily-sampled readings reflect the seasonal cycle in both sites (cf. Figure 8.3). In addition, deviations with higher frequencies result in periods of five to ten days. This interval matches the water-vapour residence time (cf. Section 2.1). Lastly, the 5-minute

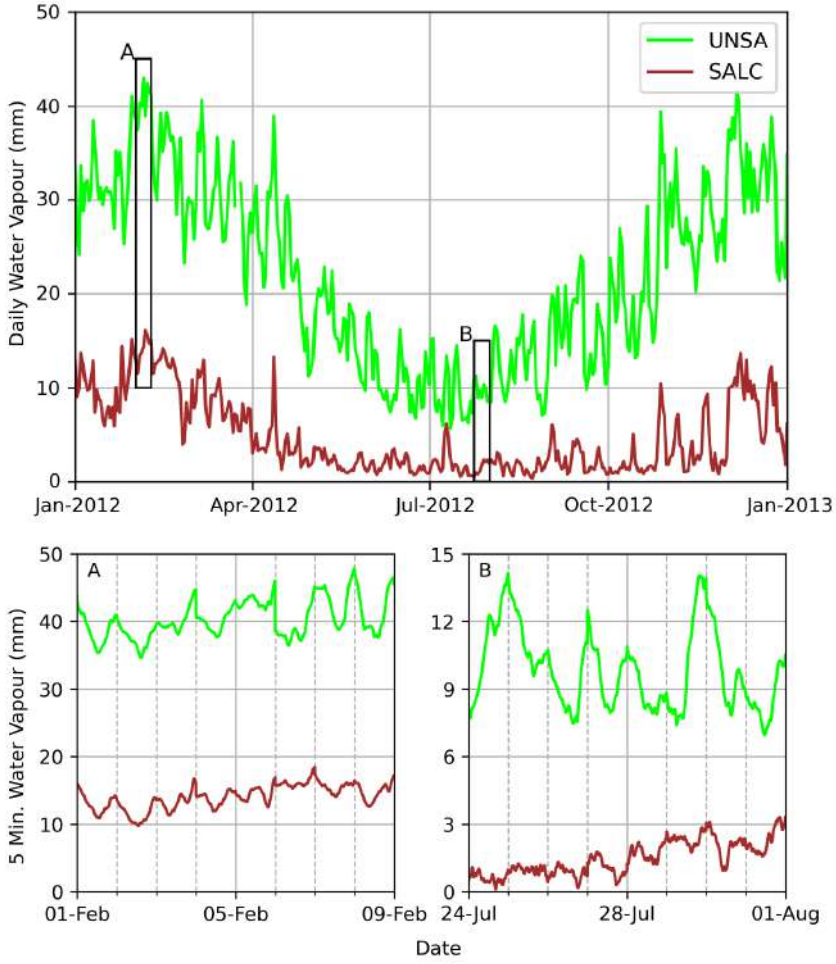

Figure 8.3: **Top:** Daily-sampled water-vapour observations for the stations UNSA at1224 m and SALC at 3799 m asl during 2012. **Bottom:** Hourly-sampled observations during two events in the wet (A) and the dry season (B). The y-axes differ in the left and right panels because of the distinct seasonality that yields totally different water-vapour values.

resolution series focuses on two characteristic frames in summer and winter, depicting the semi-diurnal and diurnal circulations.

The analysis of the signal in the frequency domain is achieved by calculating the spectrograms over the time with a sequence of Fourier transformations. This methodology is explained by Oppenheim et al. (1999), and the utilized algorithms are implemented within the SciPy library (Virtanen et al., 2020). Provided that all stations were not functional throughout the entire period, it is decided to limit this study according to the data availability. The most suitable period lies between 2010-2014, when all sites that belong to the E-W and N-S cross-sections were operational. The selected sampling window is seven days because this time frame is similar to the period of the synoptic-scale fluctuations (cf. Figure 8.3). Considering the incapability of the Fourier transformation algorithm to process discontinuous data, gaps of minor importance are forecasted with the Prophet algorithm (Taylor and Letham, 2018).

The last step of the spectral analysis includes quantifying the spectral signals. This assessment is held by decomposing the water-vapour time series (wv) into the polynomial counterpart (wv_p), the harmonic variations (wv_h), the synoptic counterpart (wv_s), and the noise (wv_n) as follows:

$$wv = wv_p + wv_h + wv_s + wv_n \tag{8.1}$$

Because of the insignificant influence of the polynomial term for short-period observations, it is not taken into account in this case. Additionally, the synoptic term only describes high-frequency signals. Hence, the water-vapour series is only described by the harmonic variations with the following equation:

$$wv_h(t) = \sum_j A_j \cos\left(\chi_j\left(t\right) - \phi_j\right) \tag{8.2}$$

where:
j frequency
A amplitude
ϕ phase
χ astronomical argument

The astronomical argument is based on the Doodson variable multipliers, as given by Hartmann and Wenzel (1995). According to the Rayleigh criterion, the in-phase and quadrature components are estimated for the signals whose period lies between the time frame corresponding to the folding (or Nyquist) frequency and the interval equal to half of the time-series extent. This process aims to calculate the time series' power-spectral density (PSD). The distribution of that data is further analyzed in a power-law fitting (Clauset et al., 2009). This method is superior to bandstop filtering approaches (e.g., Butterworth, 1930) because it is not sensitive to data discontinuities. Finally, since the probability of the natural phenomena drops exponentially with their magnitude, the Power-law distribution is ideal for this study (e.g., White et al., 2008; Lorenz, 2009; Corral et al., 2010).

The PSDs are estimated for the post-fit residuals utilizing in-house algorithms that are based on the Multi-taper method (e.g., Babadi and Brown, 2014; Di Matteo et al., 2021). Since the radiative forcing yields spectral discontinuities, the post-fit residuals are preferred against the raw data to evade biased estimations. In a further step, the amplitudes occurring from the PSDs are normalized with their standard deviations to permit the inter-comparison between different-altitude stations. Lastly, the PSDs are filtered at a set of fundamental frequencies that describe natural phenomena for a more efficient comparison of the spectral behaviour of the sites.

8.3.3 Water vapour and Rainfall Relation

The third step of this study includes comparing water vapour and high-accuracy precipitation data. In this case, the stations UNSA, CAFJ, and PUNJ are taken into consideration because there is the availability of rain-gauge instruments in the vicinity of the sites. Moreover, the observations span 24 months, from August 2019 to July 2021. Water vapour and precipitation are firmly linked, but the relation of the two scalars is not straightforward. The prior is constantly apparent in the atmosphere, while the latter occurs when the atmosphere becomes saturated and the relative humidity reaches its peak value. This results in precipitation of different forms (Glickman and Zenk, 2000). Considering the unique climate conditions of the area, precipitation only takes place in the form of rainfall. In the first phase, the water-vapour readings are averaged on a daily basis, and the top 10 % is selected. In addition, the daily-summed rainfall series for the corresponding dates are also selected. Those two sub-sets are modelled with the Power-law distribution (Clauset et al., 2009) for station-wise comparison. In the second phase, the reference data set is reversed. The dates that correspond to the top 25 % of the daily-summed rainfall are used for selecting the two sub-sets. The relation is examined on a linear basis by generating quantile-quantile (Q-Q) plots.

8.3.4 Latitudinal Moisture Gradient Transport

The last phase of this study is held to better understand the moisture-transportation processes that the LLJs drive. In this step, the wet gradients are examined together with wind and rainfall information for the stations UNSA, CAFJ, and PUNJ. More specifically, the azimuthal distributions of the wind vectors are compared against those of the wet gradients. In order to avoid biased observations due to the frictional drag on the wind, the observations for the first km above the surface are omitted. The seasonal variations of the wet gradients are examined in a second phase, where the per-epoch azimuthal distributions of the wet gradients are individually evaluated. Moreover, key directions that reflected changes in the boundary conditions are spotted by plotting the 90^{th} to 50^{th} percentile ratio. As the last step, the epochs when the top 25 % hourly rainfall takes place are filtered to select the corresponding wet gradients. Plotting the azimuthal distributions will help to detect the position of the wet masses during strong rainfall events.

8.4 Experiment Results and Discussion

The results of the analysis methods are presented in separate subsections, in the same order as in Section 8.3. Additionally, the discussion is supported with additional figures and analysis to justify the statements better.

8.4.1 K-means Stations Clustering

According to the k-means clustering, there is a high correlation between the spatial distribution of the stations and the water vapour-based separation (cf. Figure 8.4). This fact confirms the initial hypothesis, as already mentioned in previous research (Castino et al., 2017). It is important to note that the time series grouping was only held according to the water-vapour readings, independently of the stations' location. The climatic zones are defined by climatic conditions (500 mm/yr rainfall contour) and elevation (catchment of the Central Andean Plateau).

Cluster 1 experiences the highest values and refers to the low-altitude stations. The observations

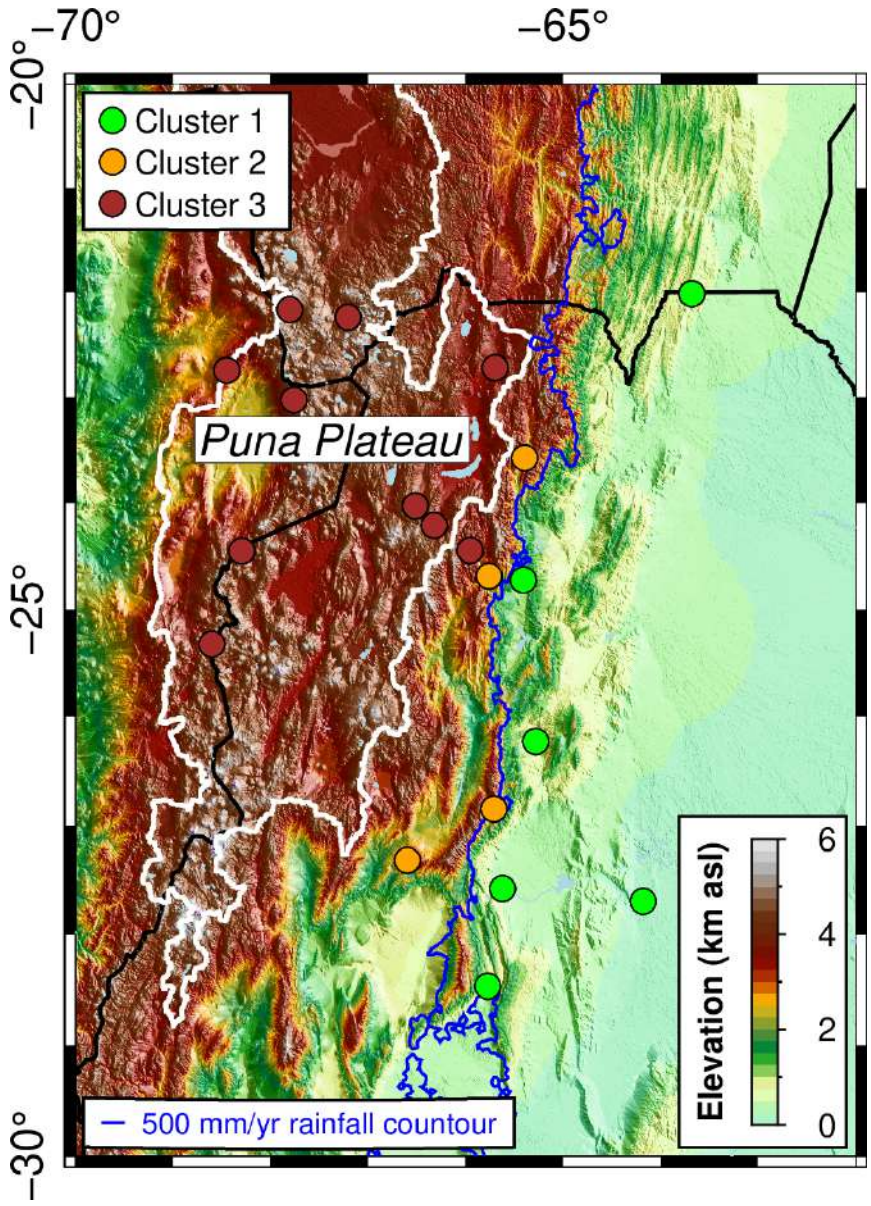

Figure 8.4: Spatial distribution of the clustered stations, according to the monthly-averaged water-vapour values. The colours correspond to Figure 8.5. The low-altitude stations are indicated with green colour and extend up to 1250 m asl. The orange points are linked with sites with an elevation between 2000-2700 m asl, and they are separated spatially by the previous cluster with the 500 mm/yr mean rainfall contour (blue line). The stations with an elevation greater than 3100 m asl are shown with brown colour. Almost all sites of this cluster are situated within the Central Andean Plateau (white line). The black lines show international borders (Topographic data obtained from ETOPO1 (Amante, 2009), rainfall information retrieved from Tropical Rainfall Measuring Mission (TRMM) (2011), as cited in Bookhagen and Strecker (2008)).

oscillate around a mean value of 27.5 mm with an amplitude of 12.5 mm. Cluster 2 is associated with the medium-altitude stations, and its time series are shifted 10-15 mm lower. Finally, the observations in Cluster 3 are virtually flat, except for the months during the austral summer. This sub-set refers to the stations in the Central Andean Plateau. Despite the differences in amplitude and shape, seasonal patterns are reflected in all time series.

Despite the aforementioned differences, there are some behavioural similarities. In each of the three instances, the highest values occur during January and February, when the SAMS takes place. On the contrary, the lowest ones occur during June. In addition, October always provides higher values than November (cf. Figure 8.5). This is the only case when the gradual increase or decrease of the water vapour is interrupted.

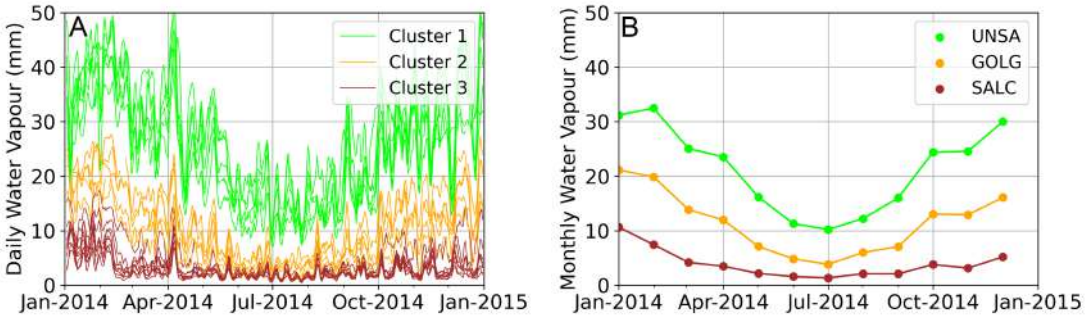

Figure 8.5: Daily-averaged water-vapour time series clustered according to their monthly mean values (A) and monthly-averaged data of three stations along the topographic gradient (B). Asl altitude: UNSA 1224 m, GOLG 2343 m, and SALC 3799 m.

The k-means clustering results suggest that the sub-tropical zone in lower altitudes exhibits high-magnitude seasonal signals. In contrast, the seasonality patterns are less evident in higher altitudes characterized by an arid climate. Furthermore, the intermediate zone experiences weaker, easily detectable seasonal signals and shows the transition between the two climate zones. This outcome points out the influence of the climate and the topography. It is in agreement with previous research that has investigated the impact of the orography in the climate conditions (Bookhagen and Strecker, 2008, 2012). In order to prove that water vapour does not only alter because of the different altitude of the sites, the observations of UNSA are projected at higher elevations for direct comparison with other stations (cf. Figure 8.6). The equation that calculates the water-vapour height decay is given as follows (Leckner, 1978; Wang et al., 2020):

$$wv = wv_0 \exp C_2 \Delta h \tag{8.3}$$

where C_2 is a constant of 0.439, and Δh is the height difference in kilometres.

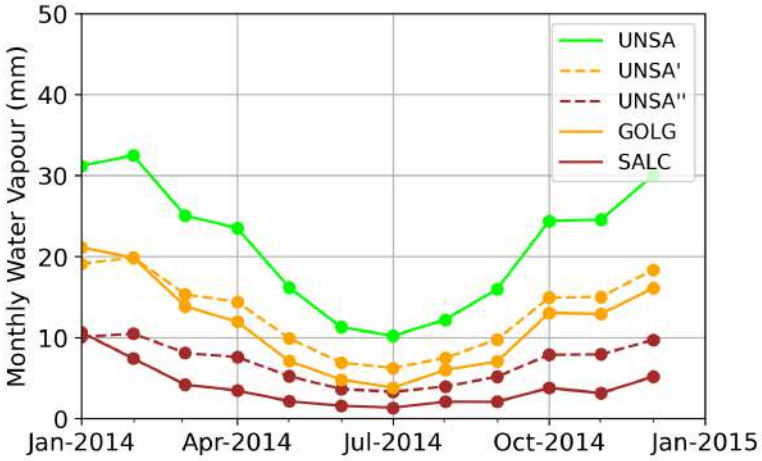

Figure 8.6: Estimation of the monthly-averaged water vapour at different altitudes. The reference station is UNSA at 1224 m asl, and its values are projected at 2343 m (UNSA') and 3799 m asl (UNSA") for comparison with GOLG and SALC, respectively. Most instances show that the water vapour-height decay rate is lower in the foothill zone.

Despite the spatial separation of the time series, there is a feature that they share in common. In all cases, there is an interruption of the gradual advancement of the water vapour during the austral spring. A better overview of this pattern is investigated by plotting the monthly means along with the standard deviations over a wider time frame (Figure 8.7). The averaged series show a smooth transition from September to November with considerable uncertainty; hence the fluctuation observed during 2014 is due to climate variability.

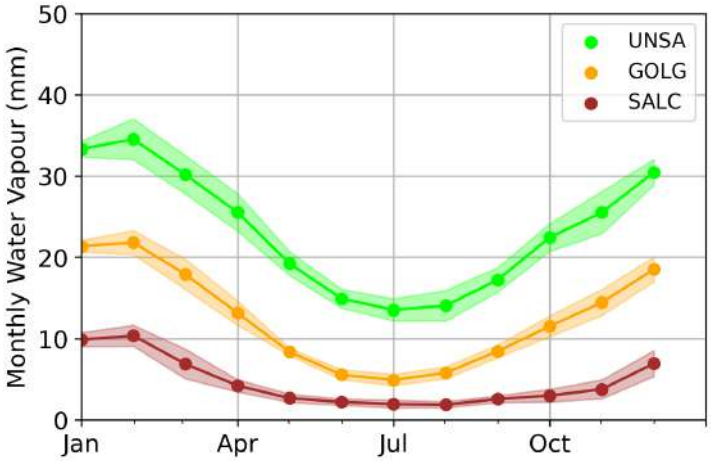

Figure 8.7: Monthly-averaged water vapour between 2010-2021 for the three stations along the topographic gradient (cf. Figure 8.5). These sets were generated by inserting ERA5 reanalysis data on pressure levels (Hersbach et al., 2020) in ray-tracing algorithms. The standard deviations are illustrated with semi-transparent colours.

8.4.2 Spectral Analysis

The spectral behaviour is initially examined by generating the spectrograms for time series along the E-W and N-S cross-sections (Figure 8.8). The spectrograms for the stations along the topographic gradient (UNSA, GOLG, SRSA, and SALC) show that the responses are weaker for the sites in high altitudes. Additionally, this degradation is augmented during winter, when water concentrations in the atmosphere are lower. On the other hand, the spectrograms related to the stations across the topographic gradient (UNSA, JBAL, TUCU, and CATA) point out similar behaviour without major differences within each graph. Finally, there is a strong signal with a daily period in all cases.

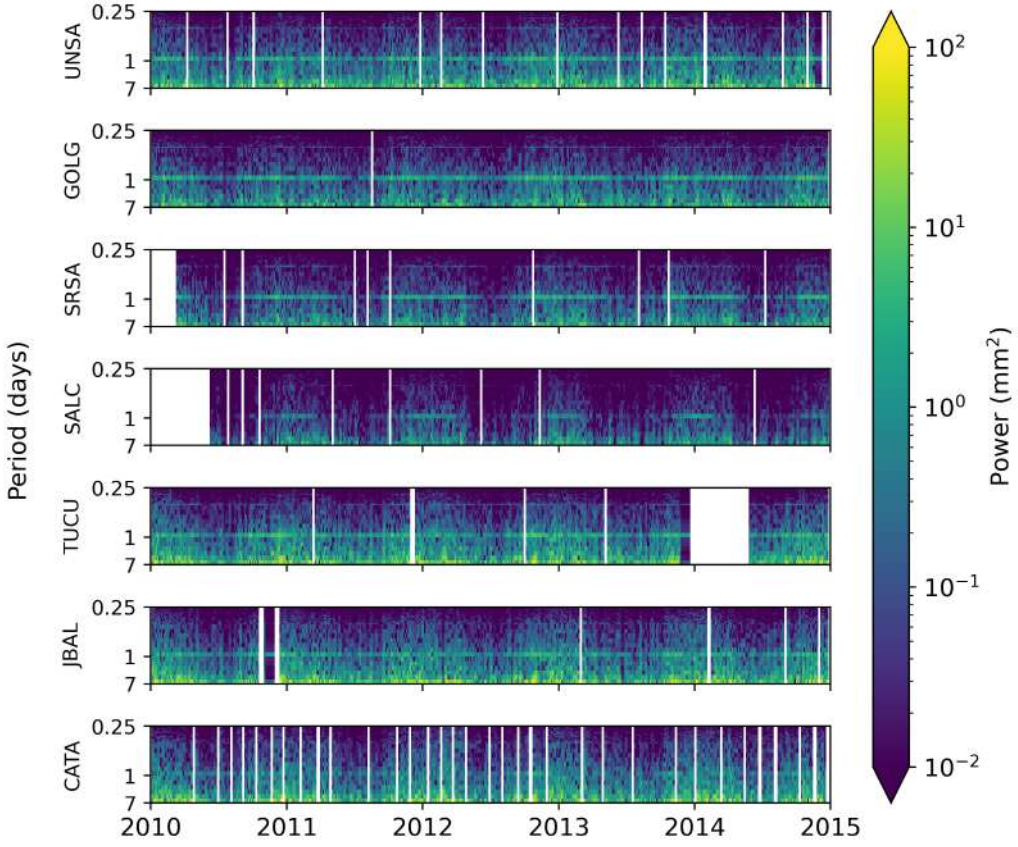

Figure 8.8: Spectrograms with a seven-day window for the stations along the east-west (E-W) and north-south (N-S) cross-sections. The analysis was held using a seven-day sampling window. (Altitude asl: UNSA 1224 m, GOLG 2343 m, SRSA 3113 m, SALC 3799 m, TUCU 456 m, JBAL 381 m, and CATA 518 m, cf. Figure 8.1 and Table 8.1).

The quantification of the spectral behaviours is examined through the PSDs of a low- and a high-elevation station (Figure 8.9). The frequencies of the major interest are the ones that correspond to the annual (An), semi-annual (S-An), monthly (M), weekly (W), and diurnal (D) periods. The yearly, half-yearly, and daily periods yield the most potent signal responses in both sites. In a station-wise comparison, the UNSA station always returns higher power than the SALC

station. In the case of the annual and daily periods, the difference is one order of magnitude. Meanwhile, the variation for the semi-annual, monthly, and weekly periods is relatively lower.

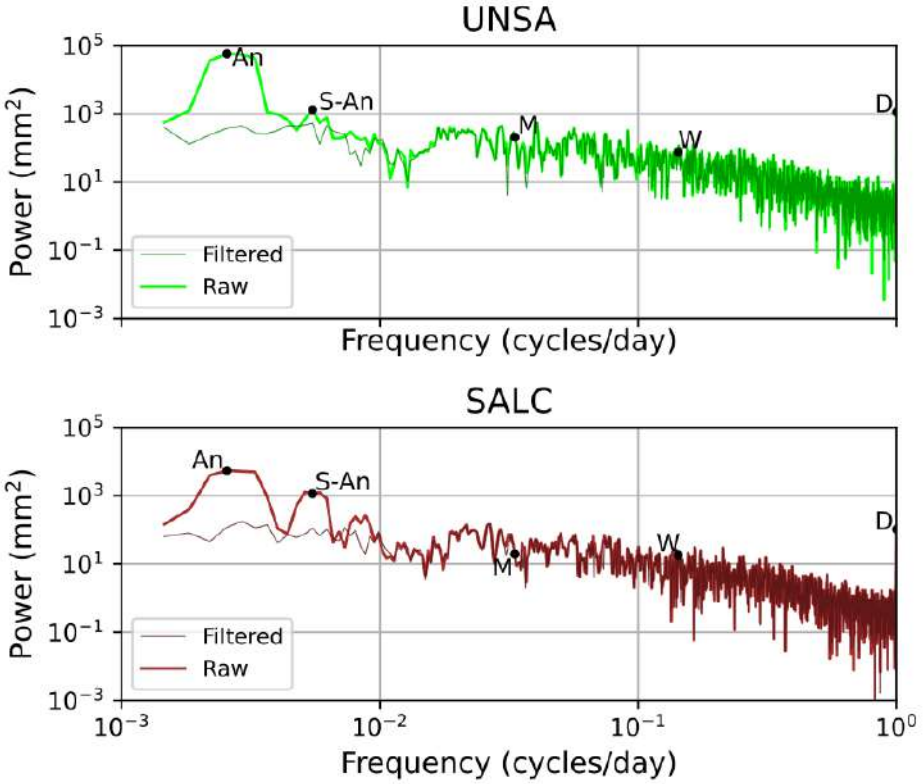

Figure 8.9: Power-spectral densities (PSDs) of the UNSA and SALC stations. The raw PSDs are illustrated with thick lines, and the filtered PSDs are illustrated with thin darker-coloured ones.

The amplitudes of the fundamental harmonics show that the signals of all stations yield significantly higher responses for the diurnal, semi-annual and annual harmonics. In contrast, among the strongest signals, the annual one stands out. Moreover, there is a gradual decrease of up to 80 % with the altitude for the stations along the topographic gradient, whereas the sites perpendicular to this direction are homogeneous. This fact coincides with the previous statements (cf.

Period	**Absolute and Relative Amplitudes (mm/-)**						
	UNSA	**GOLG**	**SRSA**	**SALC**	**JBAL**	**TUCU**	**CATA**
daily	1.85/0.19	1.82/0.25	1.44/0.26	0.54/0.14	1.63/0.14	1.90/0.16	0.83/0.18
weekly	0.30/0.03	0.08/0.01	0.05/0.01	0.11/0.03	0.37/0.03	0.54/0.05	0.53/0.05
monthly	0.51/0.05	0.43/0,06	0.32/0.06	0.24/0.06	0.94/0.08	1.27/0.11	0.68/0.06
semi-annual	10.13/1.01	7.22/1.00	5.39/0.97	3.12/0.80	11.77/0.99	11.73/0.98	10.16/0.96
annual	21.86/2.19	12.60/1.74	7.99/1.44	4.89/1.25	27.55/2.31	28.22/2.37	23.37/2.22

Table 8.2: Absolute and relative (standard-deviation normalized) amplitudes of the fundamental harmonics for the stations along the east-west (E-W) and north-south (N-S) cross-sections.

Figure 8.8). Concerning the weaker harmonics, there is no physical connection between those frequencies and the water-vapour time series. Lastly, the standard-deviation normalized amplitudes reveal similar magnitudes for the diurnal and semi-annual harmonics, while the annual one shows an amplitude-height dependency.

The fitting of the filtered PSDs of the UNSA and SALC stations to the Power-law distribution points out similar behaviours (cf. Figure 8.10). The gradients of the lines, as expressed by the power-law exponent, are similar. Furthermore, the lines are parallelly shifted, revealing different roll-over points. The level of similarity of the power-law exponents is examined via a t-test. Considering the alpha values (1.50 and 1.46), their standard deviations (0.03 for both cases), and the degrees of freedom (18 for both cases), the resulting t-score is 2.898. This value allows for the assumption of comparable gradients with a confidence level of 99.9 %. As for the roll-over points, this shift is expected because of varying PSDs (cf. Figure 8.9).

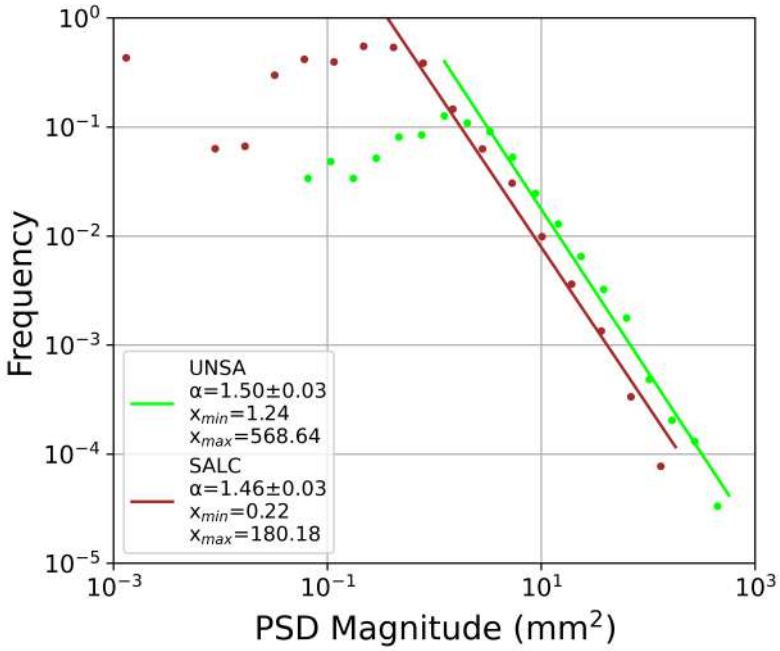

Figure 8.10: Fitting of the filtered power-spectral densities (PSDs) of the UNSA and SALC stations to the Power-law distribution. The series was logarithmically binned in 20 classes, and the minimum value (x_{min}) was set to the tipping point. The power-law exponent gives the decay rate (α).

The integrity of the GNSS- and ERA5 ray-tracing derived spectrograms (Figure 8.8) is examined against the spectral responses of purely-reanalysis data (Figure 8.11). The relative differences are of low magnitude, with the majority being less than 1 %. Nevertheless, the excellent correlation between the two sets suggests the high reliability of the GNSS data. Moreover, this methodology yields significantly higher temporal resolution (typically five minutes), being able to detect microscale water-vapour fluctuations. On the contrary, reanalysis models usually yield 1-hour and several-kilometres temporal and spatial resolution, respectively. This allows for monitoring mesoscale (or higher-scale) atmospheric phaenomena.

The predominant alignment of the water-vapour series at the yearly, half-yearly, and daily periods indicates a coincidence with the air moisture's short- and long-period cycles. Additionally, the half-yearly harmonics are relatively more evident in higher elevations due to the form of the data. More specifically, those stations exhibit an almost-flat shape during the austral winter, which results in a two-harmonic seasonal oscillation. Thus the ratio between the amplitudes is different. In the case of the low-altitude stations, the spectrograms and the PSDs reveal more robust responses, demonstrating the Andean orographic barrier's protagonist role in the formation of the local climate. Regarding the power-law fitting of the filtered PSDs, the analogous exponents for stations at different altitudes designate height-independent responses to the seasonality.

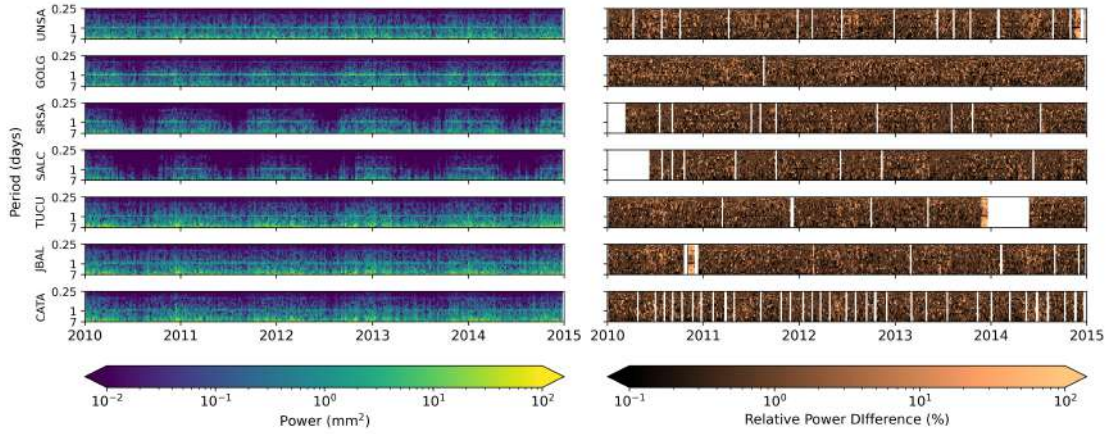

Figure 8.11: **Left:** Spectrograms with a seven-day window for the stations along the east-west (E-W) and north-south (N-S) cross-sections using ERA5 reanalysis data on pressure levels (Hersbach et al., 2020). **Right:** Comparison of the GNSS- and ERA5 ray-tracing derived data from Figure 8.8 with the purely-reanalysis data from the left panel. The variation is expressed as a relative difference.

8.4.3 Water vapour and Rainfall Relation

In this section, the focus of the research is the examination of the water-vapour values against rainfall. Initially, the reference dataset is selected as the highest 10 % of the daily-averaged water-vapour values. Moreover, the daily-summed rainfall values for the corresponding epochs comprise the secondary dataset.

In both cases, the data series fits well with the Power-law distribution (cf. Figure 8.12). As for the water vapour, the slope expressed by the exponent (α) is steeper for the UNSA and CAFJ stations. In contrast, the decline is significantly smoother for the high-elevation site. The horizontal position of the slope, as expressed by the maximum value (x_{max}), is inversely proportional to the stations' elevation. The power-law fitting of the cumulative rainfall points out an altitude-exponent relationship, but the inclinations are always smoother, and the differences between the stations are less evident. Despite the tendency for stronger events at low-altitude stations, the maximum value at CAFJ is lower than at PUNJ. Finally, the statistics of the power-law fitting indicate high uncertainty for the water vapour, where the standard deviation is 50 % of the estimated value. In the case of rainfall, this ratio is reduced to 8-22 %.

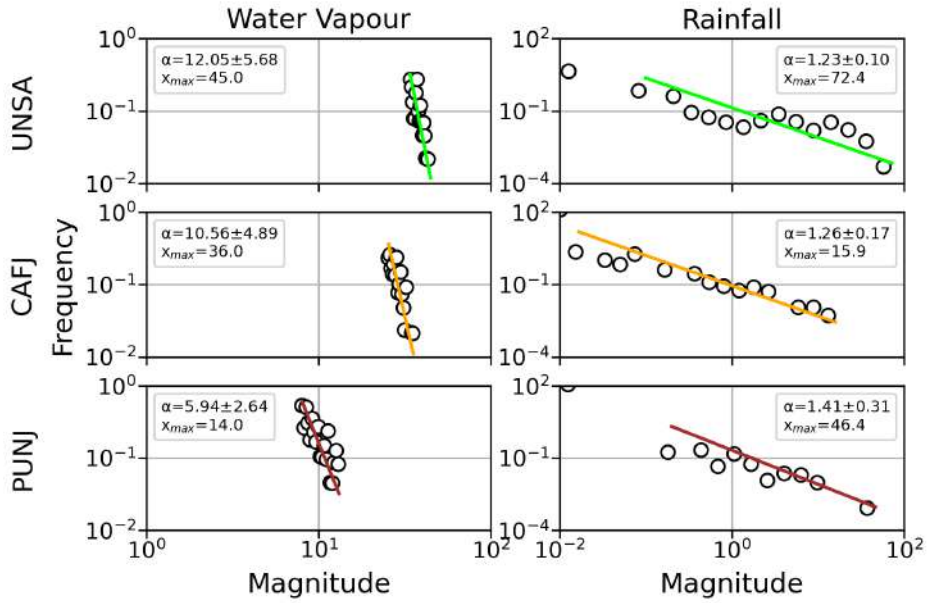

Figure 8.12: Fitting of the top 10 % daily-averaged water-vapour (left) and the corresponding daily-summed rainfall (right) of the UNSA, CAFJ, and PUNJ stations (Asl altitude: 1224 m, 1667 m, and 3760 m, respectively) to the Power-law distribution. The input data are logarithmically binned into 20 clusters. The minimum value was constrained to the lowest-magnitude cluster in the case of the water vapour. As for the rainfall, daily values less than 0.01 mm were not considered.

Station Name	**Water vapour**		**Rainfall**	
	α	$\mathbf{x}_{max}$	α	$\mathbf{x}_{max}$
UNSA	12.05±5.68	45.0	1.23±0.10	72.40
CAFJ	10.56±4.89	36.0	1.26±0.17	15.90
PUNJ	5.94±2.64	14.0	1.41±0.31	46.40

Table 8.3: Exponents (α) with their standard deviations, as well as maximum values (x_{max}) of the power-law fitting in Figure 8.12.

Subsequently, the top 25 % daily-summed rainfall is set as the reference dataset. The dates when no rainfall occurs are not taken into account. The daily-averaged water vapour constitutes the secondary dataset for the corresponding epochs. In this case, the relationship is examined on a linear basis by plotting the readings of the primary scalar against the secondary one in a series of Q-Q plots (Figure 8.13).

Even though there is no clear tie between the rainfall and water-vapour subsets, some patterns correlate to the stations' altitude. Specifically, the y-axes illustrate different-amplitude scattering, inversely proportional to the altitude. In addition, the x-axes depict similar behaviour, albeit the differences are less evident. Lastly, establishing a linear relationship is not feasible due to the high scattering and the limited amount of observations.

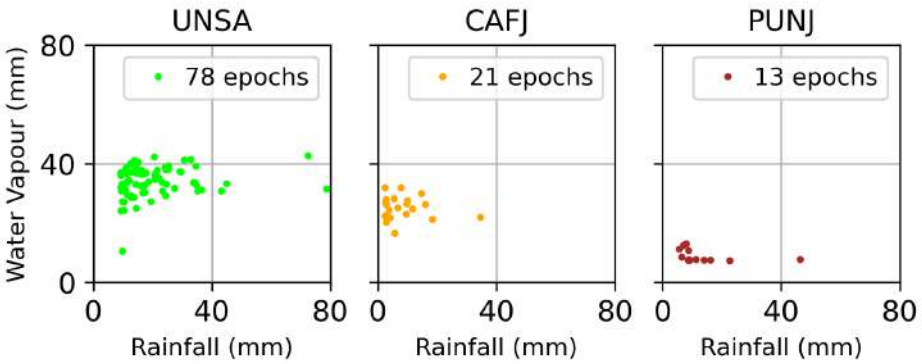

Figure 8.13: Quantile-quantile (Q-Q) plots of the top 25 % daily-summed rainfall and the corresponding daily-averaged rainfall of the UNSA, CAFJ, and PUNJ stations. Fewer observations characterize higher-elevation stations because of the less frequent rainfall events.

The maximum values of the water-vapour power-law fitting indicate greater levels at low-height stations. Additionally, the slopes reveal a lower inclination for the sites in the Central Andean Plateau. The first finding has already been previously mentioned (cf. Figures 8.3 and 8.5). In contrast, the latter finding is more intriguing, showing more homogeneous peak water-vapour values at higher elevations. In the case of the power-law fitting of the rainfall, although there is a height-magnitude dependency, it is possible to achieve heavy occurrences at high elevations, but the probability is lower. This perspective, nevertheless, does not hold well with the medium-elevation station CAFJ. One has to consider that his facility is situated in an intermontane basin, and the lower cloud masking leads to heat-up that does not occur in the foothill zone. Furthermore, despite the relatively high standard deviation of the estimated power-law exponents, the tendencies are apparent.

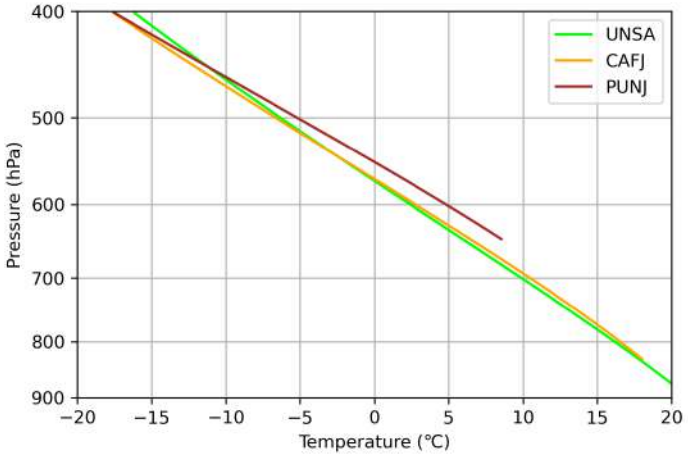

Figure 8.14: Average tropospheric-temperature profiles for the UNSA, CAFJ, and PUNJ stations from 2010 to 2021, during the austral summer months. The observations do not start from the same level because of the different heights of the stations (Temperature information retrieved from ERA5 reanalysis data on pressure levels (Hersbach et al., 2020)).

The Q-Q plots verify the presence of strong rainfall at the high-altitude zone, but the air conditions differ. First, the water-vapour spectrum is less broad, illustrating that atmospheric saturation requires different air moisture levels depending on the height. In addition, a second factor that affects the saturation is the ambient temperature. Considering the along-the-height cooling and the varying cloud masking due to the divergent topography, there is a distinct temperature variation between the examined stations (cf. Figure 8.14).

8.4.4 Latitudinal Moisture Gradient Transport

Initially, the wet gradients are correlated against the wind vectors for the entire period of observations between August 2019 and July 2021 (Figure 8.15). In the case of the low-elevation station UNSA, the wet gradients point from the northwest to the southeast direction, with a

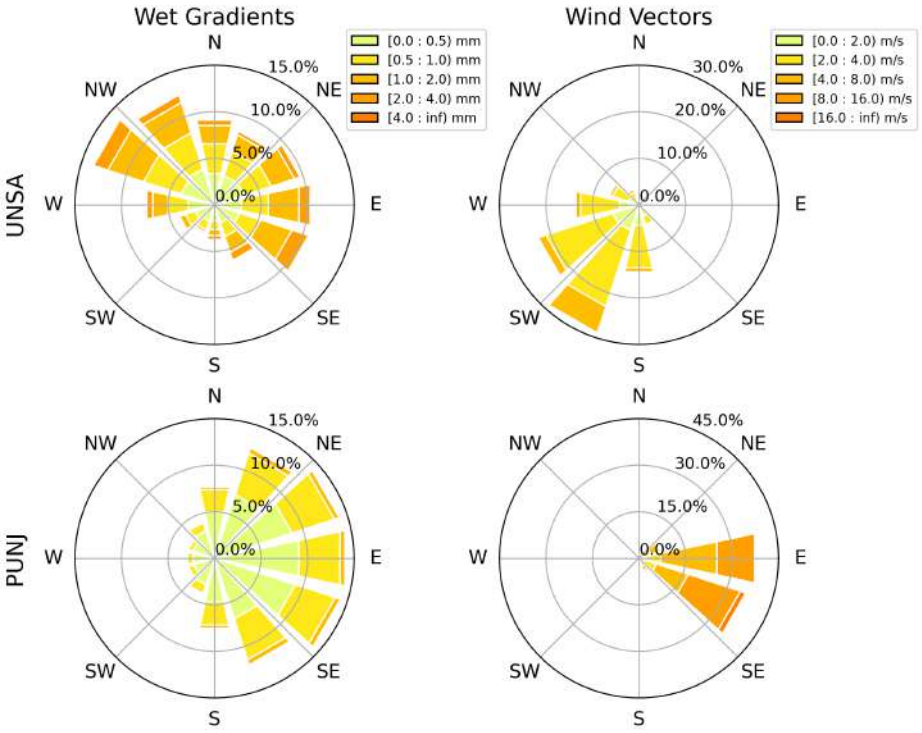

Figure 8.15: Two-dimensional distributions of the directions and the magnitudes of the wet gradients (left) and the wind vectors (right). The upper panel is referred to the UNSA station at 1224 m asl, and the lower one is referred to the PUNJ station at 3760 m asl. The directions are split into 12 azimuthal frames of 30° width. The magnitudes are separated into five different-size clusters, depending on the scalar to be represented. The effective radius of influence of the vast majority of the observations is roughly 20 km (cf. Figure 8.19). The wind observations refer to the median height between the level of one kilometre above the station and the pressure level of 200 hPa. Low elevation observations are excluded because of the wind surface friction. The temporal resolution of the data series is five minutes, and the coverage is limited from August 2019 to July 2021 to account for the reduced range of the GNSS observations (Wind information is retrieved from the ERA5 reanalysis data on pressure levels (Hersbach et al., 2020)).

primary concentration to the northwest. The winds in this station point to the southwest. In the high-elevation station PUNJ, both the wet gradients and the winds are oriented to the east, but the prior cover a broader angular spectrum of 180°. Lastly, the wind velocities in this site are higher-magnitude.

The per-epoch analysis depicts the reliance of the wet gradients on seasonal variation (Figure 8.16). The UNSA station is subject to northerly LLJs, and the events are concentrated around two azimuths towards the directions of 90° and 270°. Moreover, there is a seasonal oscillation. For example, the austral spring and summer seasons mainly exhibit observations to the east, while this direction is reversed during the austral fall and winter seasons. On the other hand, the PUNJ station is characterized by a narrow-range peak-azimuth oscillation between 45° and (135° in the course of the epochs.

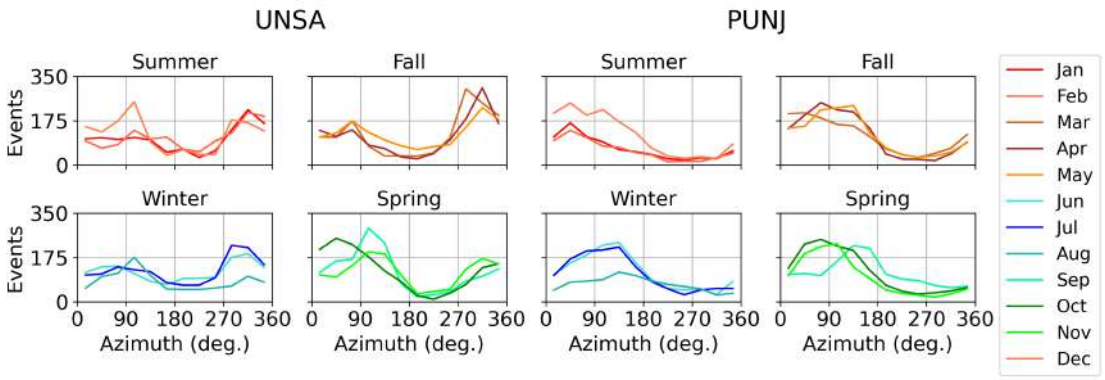

Figure 8.16: Monthly- and event-based distribution of the wet gradients for the UNSA and PUNJ stations. The months are grouped according to the austral seasons. The temporal coverage and directional clustering coincide with those in Figure 8.15. For a better illustration of the results, the wet gradients are sampled on an hourly basis, and the events point out the occurrences for each azimuthal frame throughout each month.

In a follow-up step, the 90^{th} to 50^{th} percentile ratios of the wet gradients are evaluated in a direction-wise analysis (Figure 8.17). The normalization of the high-rank wet-gradient magnitudes by their medians helps identify extraordinarily high occurrences that point out changes in the atmospheric boundary conditions. Additionally, the per-direction and -epoch separation assists in focussing on key azimuths and seasons. For example, the UNSA station experiences observations in all directions, but the most robust ratios point to azimuths between 15°-75° (northeast-east). On the contrary, the PUNJ station yields more homogeneous observations with significantly lower ratios. Moreover, wedges are directed eastwards. Finally, the summer season provides slightly higher magnitudes.

Considering all previous results, the last step of this investigation is the focus on the wet gradients during heavy rainfall. More specifically, the top 25 % daily-summed rainfall is filtered, and the wet gradients during those epochs are printed (Figure 8.18). In the UNSA station, there are observations throughout the horizon, but the main concentration of the events is towards the southeast. In contrast, the PUNJ station only yields five directions, with the most dominant -in terms of magnitude- also pointing to the southeast. In both cases, the majority of the wet gradients are oriented eastwards (UNSA: 105°-165°, PUNJ: 15°-135°), demonstrating the influence

of the topographic shielding.

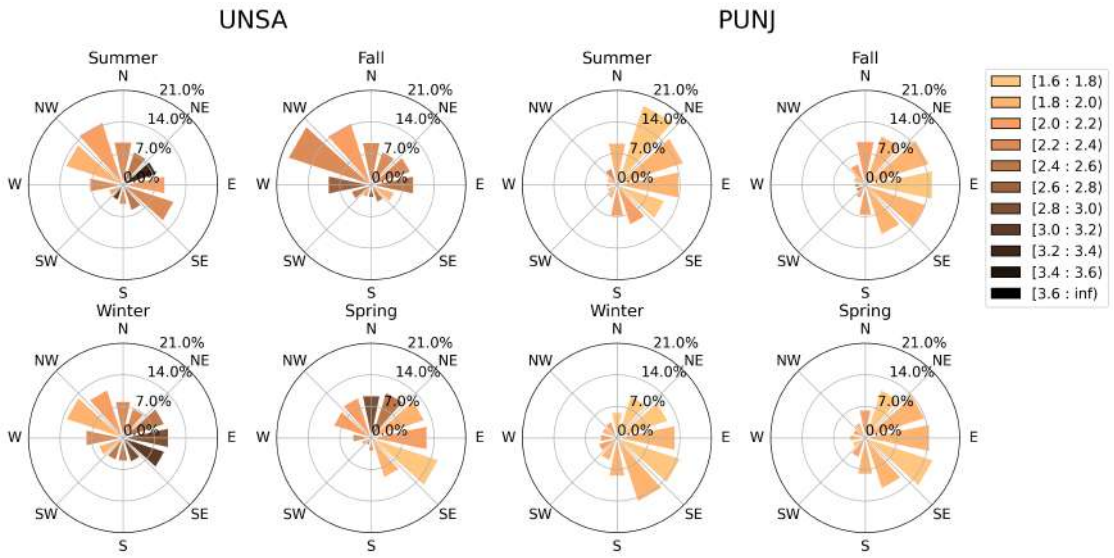

Figure 8.17: Ratios between the 90^{th} and 50^{th} percentile wet gradients' magnitudes for the UNSA and PUNJ stations. The temporal coverage and directional clustering coincide with these in Figure 8.15.

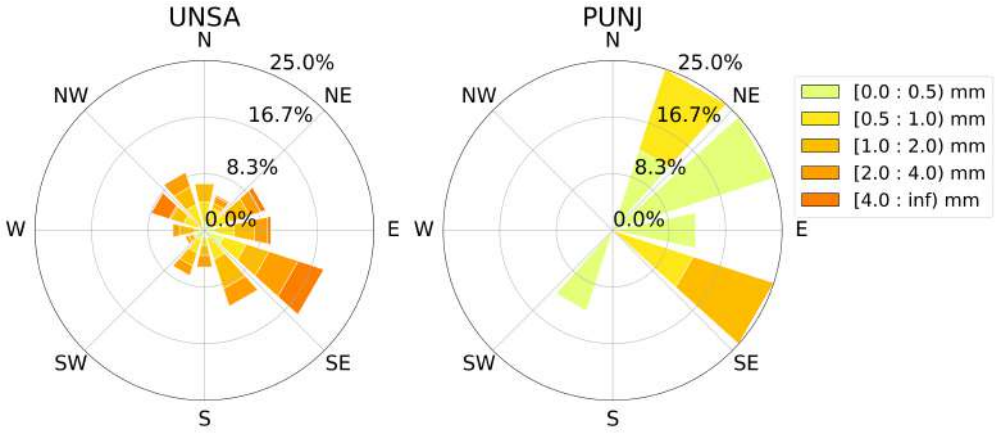

Figure 8.18: Distribution of the wet gradients for the top 25 % rainfall events during the austral summer months for the UNSA and PUNJ stations. The temporal coverage and directional clustering coincide with this in Figures 8.15, 8.16 and 8.17. In-situ meteorological stations with an hourly temporal resolution retrieve rainfall information.

The stations in the foothill zone are influenced by the LLJs along the Andes, indicating moisture fluxes from the east and northeast to the south. On the other hand, the stations in the high-altitude zone do not demonstrate a correlation between the wind directions and the wet gradients, indicating minimal influence by the LLJs (cf. Figure 8.15). Furthermore, the wind velocities differ

between each station because they do not refer to the same point. When examining a constant pressure level, there is no notable difference across the entire area of interest. In addition, the seasonal grouping of the wet gradients does not reveal significant interseasonal variations, illustrating the dominant impact of the altitude and the complex terrain (cf. Figure 8.16). The link to the northerly LLJs along the Andes for UNSA is also shown by the ratios between the 90^{th} and 50^{th} percentile of the wet gradients' magnitudes. Moreover, the highest ratios are oriented towards the intersection point between the Andean cordillera and the circulation path of the LLJs (cf. Figures 8.15). The examination of the wet gradients in parallel with the heaviest daily rainfall events complements the statements mentioned earlier, showing that the main moisture fluxes in Salta originate in the eastern and southeastern flanks of the city. In some cases, heavy rainfall occurs on the western flank, between the mountain range and the city. This outcome clearly demonstrates the influence of the topography on moisture circulation. In the case of the PUNJ station, even though this facility exhibits weaker wet-gradient magnitudes, their directions are highly associated with the topography (cf. Figures 8.16 and 8.19). This occurs because the moisture inhomogeneity of the atmosphere in very high altitudes is only due to the flow of wet masses.

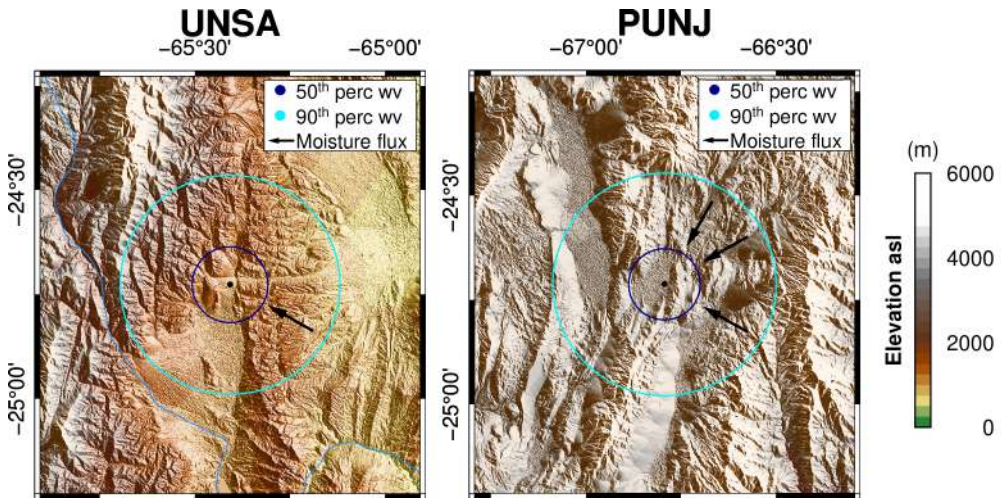

Figure 8.19: Topographic setting of the vicinity of the UNSA and PUNJ stations. The major 50 % that influence the GNSS observations are indicated by the green cycles with an approximate radius of 20 km. The light-green cycle with an approximate radius of 50 km points out the influence of the top 90 % of the measurements. The black vectors show the most prominent moisture fluxes during heavy rainfall events (cf. Figure 8.18) (Topographic data obtained from ETOPO1 (Amante, 2009)).

8.5 Conclusions

This chapter focuses on exploiting the capabilities of the GNSS Meteorology for a better understanding of the moisture circulation over northwestern Argentina. Datasets from 23 ground stations cover the period between 2010-2021, and the observations are used to measure the atmospheric water vapour at a very high temporal resolution of five minutes. Four non-independent experiments were carried out, according to which the following noteworthy assertions are derived:

- The water-vapour series depict the climatic gradient that characterizes the South-Central

Andes. The clustering of the stations separates the area into three zones: a) a low-elevation sector that is subject to heavy seasonal rainfall due to the humidity transportation by the LLJs; b) a middle-elevation sector that acts as a transition zone from the foothills to the Central Andean Plateau; and c) an extremely arid sector at high altitudes that with the lowest absolute seasonal variability.

- The spectral analysis addresses the seasonal behaviour of the signals. The most prominent frequencies correspond to the annual, semi-annual, and diurnal periods. Although there is a clear relation between the periods' magnitudes and the stations' altitudes, with the lower ones yielding higher values, a relative comparison shows similar responses to the seasonality.

- The relation between water vapour and rainfall initially points out a dependency on higher values with lower altitudes. Moreover, heavy rainfall at higher altitudes is still possible, but the probability rate is lower. This experiment also shows that the atmospheric conditions that may yield intense events are elevation-dependent. The water-vapour range is significantly narrower in high altitudes than in lower ones. In addition, air temperature is an other major parameter influencing atmospheric saturation.

- The wet-gradients analysis highlights the influence of the topography on moisture circulation. Although the water vapour propagation is generally dictated by the LLJs and the MCSs on a regional scale, topographic artefacts significantly alter the local climate by shaping the air-moisture propagation corridors.

Chapter 9

Summary and Outlook

This research study focuses on examining two distinct GNSS remote-sensing techniques for observing soil moisture and water vapour. The prior variable is measured by exploiting reflected signals (GNSS-R), and the latter variable is based on the signal delay due to the propagation through the atmosphere. Moreover, there is a complementary case study related to sea-level monitoring with GNSS-R.

Although the focus area is the South-Central Andes and, more specifically, northwestern Argentina, the soil-moisture methodology was first developed using easily-accessible data from pilot stations in northeastern Germany. Additionally, data from two stations on the Atlantic coast of the Netherlands and France were used in the sea-level experiment. In this case, the processing software for this application was based on the methodology for soil-moisture calculation. In a final stage, the developed algorithm was tested in the region of main interest. This decision was taken under compulsion because it was impossible to realize the logistics for the data acquisition in South America during the COVID-19 pandemic.

On the other hand, the GNSS meteorology technique is well established, and there was no need for further development of the raw-data analysis process. However, the main focus of this part is the climate analysis and the detection of the moisture-circulation pathways over the South-Central Andes. Instead of only exploiting the water-vapour readings in the zenith direction (integrated water vapour), this research also considers the azimuthal asymmetry. The analysis is based on observations from a network of 23 stations spread between Argentina, Chile, and Bolivia. In addition, the facilities are located over a wide altitude range; this allows for examination of the water vapour in different climate conditions.

9.1 GNSS Reflectometry

The soil-moisture experiments illustrate, in general, very promising results with a high level of agreement with the reference solutions. The modernized approximation that was developed during this study indicates improved performance because of the use of multiple constellations and carrier signals, and due to the introduction of a more advanced mathematical model. Since the GNSS-R and TDR-FDR methodologies do not measure soil moisture in the same way and at the same position, certain discrepancies that reflect how each methodology functions are to be expected. Especially the geodetic receivers in the pilot stations in northeastern Germany yield high-quality output. However, the low-cost receivers do not always perform consistently, and

the results may degrade, depending on the model. In this case, the results highly depend on the numerical resolution of the observations. On the other hand, the stations in northwestern Argentina show a different attitude. The performance is controlled by the extreme climate conditions of the zone that keep the soil-moisture levels low and affect the soil stratification. More specifically, the ground is subject to erosion and its porosity is abnormally high, while there is a station characterized by high salinity. Hence, the output is of lower quality because it is affected by the lower soil density and the higher dielectric constant. Furthermore, additional calibration is suggested to achieve better solutions.

The sea-level test case was held to evaluate the suitability of the GNSS-R methodology for measuring dynamic height changes. The observations are inserted into a tidal model, and the calculated coefficients from each solution are inter-compared. This strategy simplifies the evaluation and ensures its integrity. The results show that GNSS-R permits sub-decimetre measurements when all available constellations and carrier frequencies are combined. Hence, redundant observations are beneficial for the results, as noted in previous experiments. Additionally, the GNSS-R estimated tidal models yield more accurate and consistent higher-magnitude tidal coefficients that significantly exceed ($>$ two times) the a-posteriori standard deviation. Lastly, it is essential to mention that the GNSS-R methodology and the TG do not function similarly. The prior scans a whole surface and calculates level height at non-uniform time intervals, while the latter performs point measurements with constant temporal resolution.

Ground-based GNSS-R is a relatively recent methodology. The first applications were developed in the 1990s-2000s, and even though it has been proven through various research studies that this technique is very promising, high-quality results call for particular conditions. Independently of the variable of interest, vertical obstacles in the vicinity of the GNSS antenna are deterring factors because they block the reflections on the surface of interest (the soil or the water). Moreover, soil-moisture applications require low vegetation and smooth and flat surfaces. Hence, although operational use in agriculture is complex, reflectometry-based soil moisture could be introduced into weather-prediction models. Numerous permanent GNSS networks in the world provide the necessary infrastructure, and it is only needed to select the fraction of the stations that satisfy the necessary conditions. Moreover, reflectometry data could be combined with satellite observations to take advantage of the high-frequency but relative measurements of the prior and the very precise but sparse readings of the latter. Concerning the water-level monitoring applications, the existing seafront stations could be employed for measuring the tides to facilitate marine activities.

9.2 GNSS Meteorology

The atmospheric-moisture analysis exploits the capabilities of GNSS meteorology. While the analysis of the water content in an atmospheric column has already been examined in previous research studies, the examination of the azimuthal gradient is novel. The results confirm the separation of northwestern Argentina into three climatic zones, with a high (negative) correlation between the stations' water vapour levels and their altitudes. Despite this distinction, the seasonal and diurnal signatures may differ in magnitude, but they are always apparent. When comparing high-accuracy rain measurements against water vapour, this investigation initially points out a high correlation between those variables. In addition, the results designate intense but less frequent rainfall events in high altitudes. Lastly, considering the azimuthal inhomogeneity of the atmosphere allows for the detection of station-related moisture-circulation pathways.

More specifically, it was possible to spot and analyze the direction of the moist fluxes during heavy rainfall.

GNSS meteorology permits very accurate measurements in near real-time with very high temporal resolution. Thus, it is successfully used in weather prediction for many years. Those characteristics show supremacy against the reanalysis models and emphasize the necessity of a homogenized and dense GNSS network that covers both urban and remote areas. This set-up would provide a complete overview of the atmosphere through a three-dimensional analysis. Moreover, moisture-gradient information could be integrated into nowcasting and weather-prediction applications for better handling heavy rainfall. Even though this approximation has not been tested yet, this research shows high potential. The economy in northwestern Argentina is based on agriculture, and the organization of logistics is a topic of significant importance. Accurate prediction of severe events would help properly manage natural hazards and protect crops and road networks.

Appendix A

Used Hardware

This appendix includes photos of the hardware devices used during the station-installation campaign in northwestern Argentina. It is separated into four sections, depending on the equipment category. Namely, a) the hardware for controlling the sensors and data storage; b) the GNSS instruments; c) the TDR-FDR sensors for measuring soil moisture; and d) the meteorological equipment.

A.1 Sensors-Monitoring and Data-Storage Equipment

Figure A.1: **Left:** TinyPc Linux-based computer connected to a portable battery. **Right:** SOLARA 100 Wp solar panel. The computer was used for the transmission of commands to the sensors to ensure their uninterrupted operation and for data storage. The solar panels were only used in the case there was not possibility for connection to the local network.

A.2 GNSS Equipment

Figure A.2: **Left:** Javad GrAnt-G3T antenna. **Right:** Javad Delta TRE-G3T multi-frequency and -constellation geodetic receiver. The two instrument do not operate autonomously, but they are connected with a cable.

Figure A.3: **Left:** Swift Navigation GPS500 antenna. **Right:** GeoStar GeoS-5M single-frequency low-cost receiver. The two instrument do not operate autonomously, but they are connected with a cable.

Figure A.4: Novatel SMARTV1G smart antenna. This assembly only receives single-frequency signals and operates autonomously because it includes both the antenna and the receiver.

A.3 Soil-Moisture Equipment

Figure A.5: Campbell CR800 data logger connected to nine Truebner SMT-100 soil-moisture probes. The data logger includes a processor that controls the probes and stores the observations. The measurements are obtained by the probes that are buried in the soil.

A.4 Meteorological Equipment

Figure A.6: Vaisala WXT536 meteorological station. This equipment records air temperature, relative humidity, atmospheric pressure, precipitation, and wind speed and direction.

Appendix B

Complete Soil-Moisture Estimations

This appendix includes complete time series for the experiments described in Chapter 5. The presented time series are only related to MARQ and TRFS stations because they are the ones that undergo the longest measurements. In all figures, G, R, and E indicate GPS, GLONASS, and Galileo, respectively. In addition, days with temperatures below 4 °C are labelled with a cyan background, whereas days with temperatures over 25 °C have a red background. Finally, the vertical blue bars show the precipitation.

B.1 MARQ Station

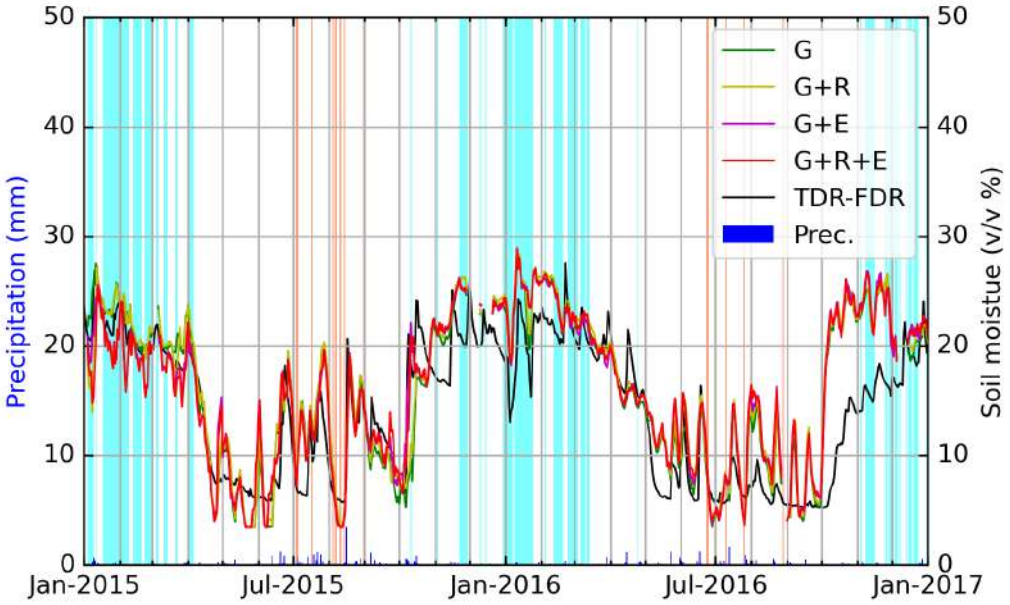

Figure B.1: Soil-moisture estimation in MARQ station during 2015-2016.

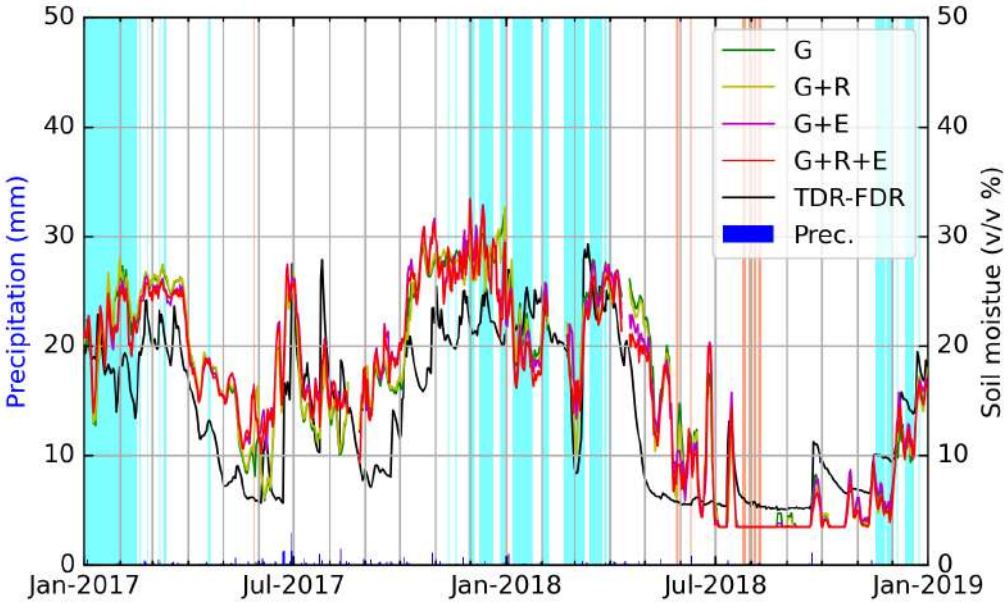

Figure B.2: Soil-moisture estimation in MARQ station during 2017-2018.

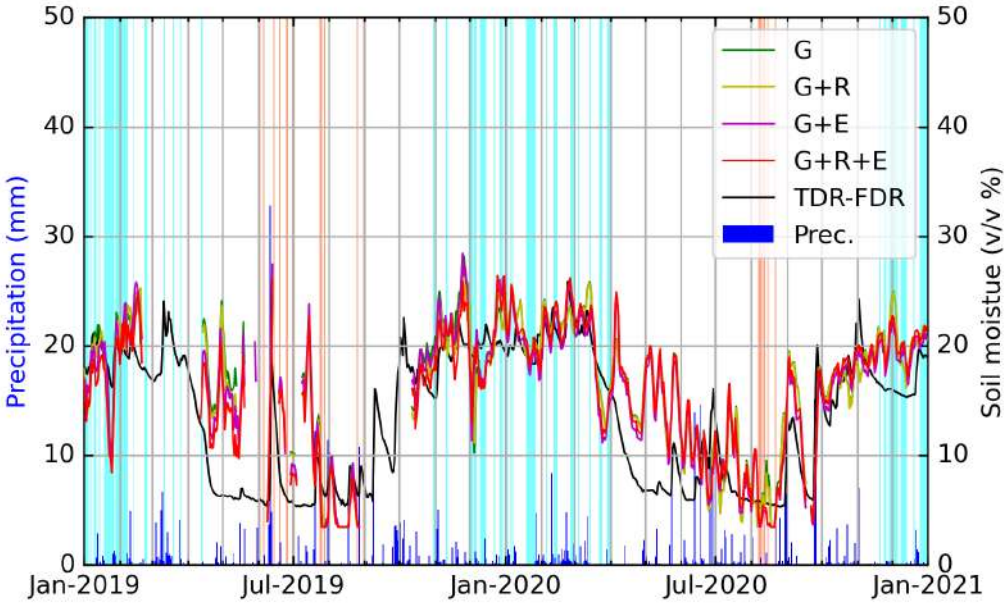

Figure B.3: Soil-moisture estimation in MARQ station during 2019-2020.

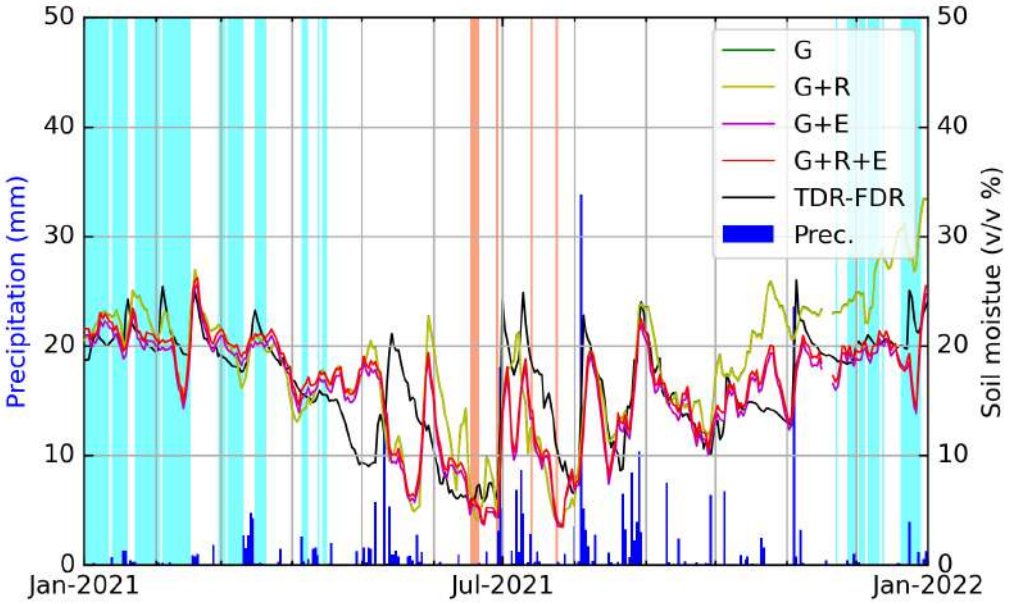

Figure B.4: Soil-moisture estimation in MARQ station during 2021.

B.2 TRFS Station

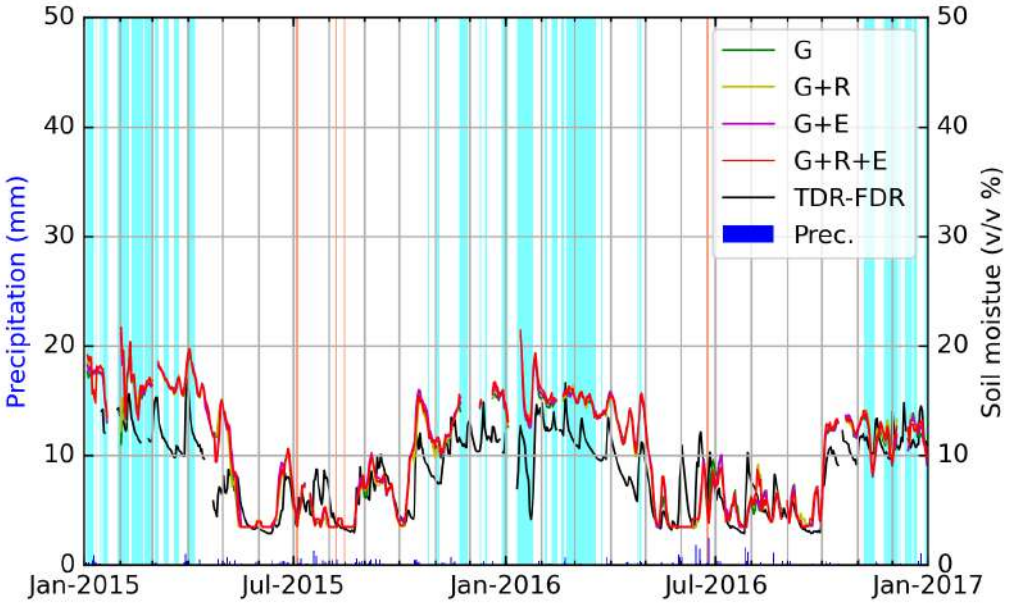

Figure B.5: Soil-moisture estimation in TRFS station during 2015-2016.

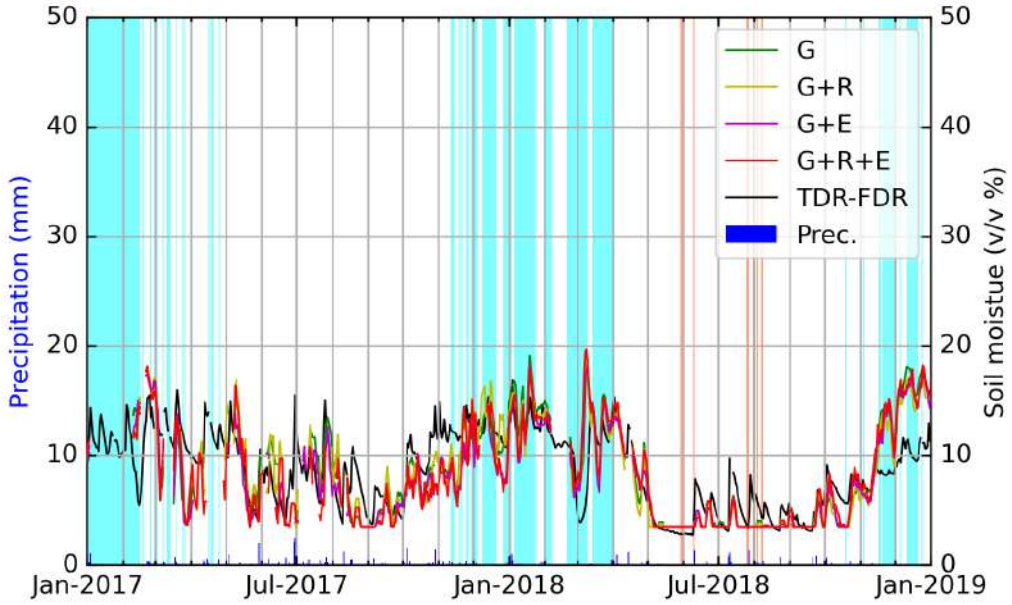

Figure B.6: Soil-moisture estimation in TRFS station during 2017-2018.

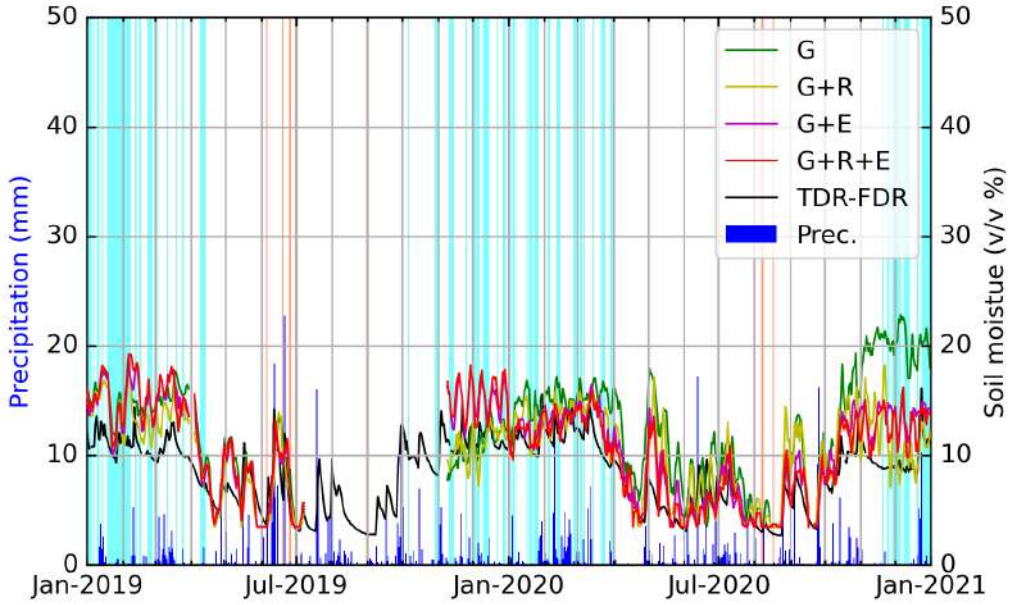

Figure B.7: Soil-moisture estimation in TRFS station during 2019-2020.

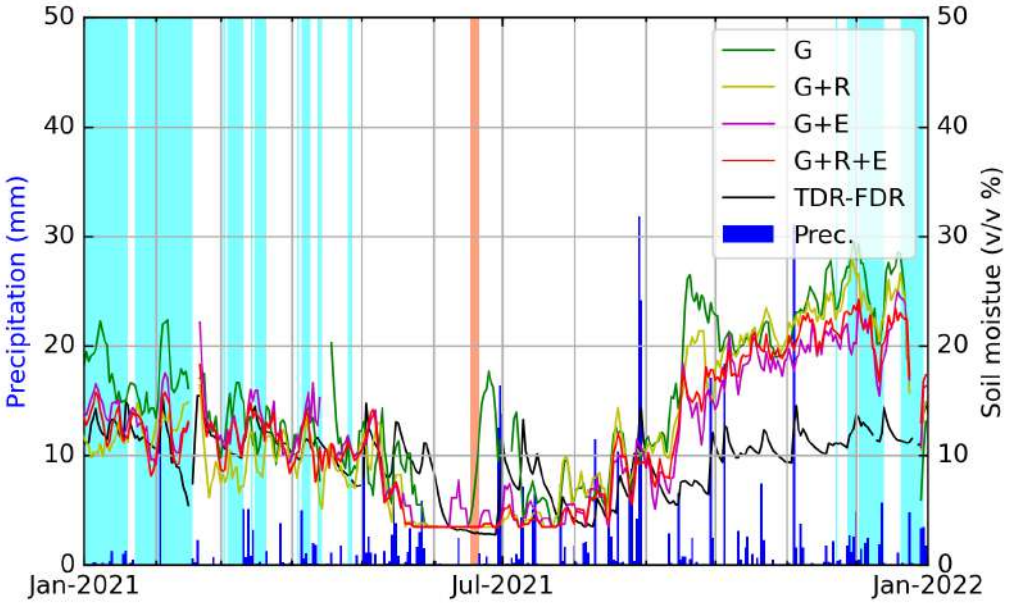

Figure B.8: Soil-moisture estimation in TRFS station during 2021.

Bibliography

Allmendinger, R. W., Jordan, T. E., Kay, S. M., & Isacks, B. L. (1997). The evolution of the Altiplano-Puna plateau of the Central Andes. *Annual Review of Earth and Planetary Sciences*, *25*(1), 139–174.

Alonso, R. N., et al. (2006). Tectonics, climate, and landscape evolution of the southern central Andes: the Argentine Puna Plateau and adjacent regions between 22 and 30 S. In *The Andes* (pp. 265–283). Springer. https://doi.org/10.1007/978-3-540-48684-8_12.

Alshawaf, F., Balidakis, K., Dick, G., Heise, S., & Wickert, J. (2017). Estimating trends in atmospheric water vapor and temperature time series over Germany. *Atmospheric Measurement Techniques*, *10*(9), 3117–3132, https://doi.org/10.5194/amt-10-3117-2017.

Amante, C. (2009). ETOPO1 1 Arc-Minute Global Relief Model: Procedures, Data Sources and Analysis. Available online: https://doi.org/10.7289/V5C8276M. Accessed: 15.11.2021.

Anderson, M. G. (2005). *Encyclopedia of Hydrological Sciences*. Wiley Online Library. ISBN 978-0-471-49103-3.

Antonoglou, N., Balidakis, K., Dick, G., Wickert, J., & Bookhagen, B. (2022a). Hydrostatic and wet signal delays calculated from a network of 23 GNSS stations in northwestern Argentina between 2010-2021. https://doi.org/10.5880/GFZ.1.1.2022.002.

Antonoglou, N., Balidakis, K., Wickert, J., Dick, G., de la Torre, A., & Bookhagen, B. (2022b). Water-Vapour Monitoring from Ground-Based GNSS Observations in Northwestern Argentina. *Remote Sensing*, *14*(21), 5427, https://doi.org/10.3390/rs14215427.

Arras, C., Wickert, J., Beyerle, G., Heise, S., Schmidt, T., & Jacobi, C. (2008). A global climatology of ionospheric irregularities derived from GPS radio occultation. *Geophysical Research Letters*, *35*(14), https://doi.org/10.1029/2008GL034158.

Asgarimehr, M., Zavorotny, V., Wickert, J., & Reich, S. (2018). Can GNSS reflectometry detect precipitation over oceans? *Geophysical Research Letters*, *45*(22), 12–585, https://doi.org/10.1029/2018GL079708.

Babadi, B. & Brown, E. N. (2014). A Review of Multitaper Spectral Analysis. *IEEE Transactions on Biomedical Engineering*, *61*(5), 1555–1564, https://doi.org/10.1109/TBME.2014.2311996.

Bai, W., et al. (2018). Evaluation of atmospheric profiles derived from single-and zero-difference excess phase processing of BeiDou radio occultation data from the FY-3C GNOS mission. *Atmospheric Measurement Techniques*, *11*(2), 819–833, https://doi.org/10.5194/amt-11-819-2018.

Balidakis, K. (2019). On the development and impact of propagation delay and geophysical loading on space geodetic technique data analysis (PhD Thesis) (pp. 90–94). Technische Universität Berlin, Berlin, Germany. Available online: https://depositonce.tu-berlin.de/handle/11303/10136. Accessed: 08.02.2023.

Balidakis, K., Nilsson, T., Zus, F., Glaser, S., Heinkelmann, R., Deng, Z., & Schuh, H. (2018). Estimating integrated water vapor trends from VLBI, GPS, and numerical weather models: Sensitivity to tropospheric parameterization. *Journal of Geophysical Research: Atmospheres*, *123*(12), 6356–6372, https://doi.org/10.1029/2017JD028049.

Bar-Sever, Y. E., Kroger, P. M., & Borjesson, J. A. (1998). Estimating horizontal gradients of tropospheric path delay with a single GPS receiver. *Journal of Geophysical Research: Solid Earth*, *103*(B3), 5019–5035, https://doi.org/10.1029/97JB03534.

Bauer, F., et al. (2006). The GPS space service volume. In *Proceedings of the 19th international technical meeting of the Satellite Division of the Institute of Navigation (ION GNSS 2006)* (pp. 2503–2514).

Beard, R. & Senior, K. (2017). Clocks. In *Springer Handbook of Global Navigation Satellite Systems* (pp. 121–164). Springer. https://doi.org/10.1007/978-3-319-42928-1_5.

Beckheinrich, J., Beyerle, G., Schön, S., Apel, H., Semmling, M., & Wickert, J. (2012). WISDOM: GNSS-R based flood monitoring. In *2012 Workshop on Reflectometry Using GNSS and Other Signals of Opportunity (GNSS+ R)* (pp. 1–6).: IEEE. https://doi.org/10.1109/GNSSR.2012.6408257.

Bender, M., Stosius, R., Zus, F., Dick, G., Wickert, J., & Raabe, A. (2011). GNSS water vapour tomography–Expected improvements by combining GPS, GLONASS and Galileo observations. *Advances in Space Research*, *47*(5), 886–897, https://doi.org/10.1016/j.asr.2010.09.011.

Benevides, P., Catalao, J., & Nico, G. (2019). Neural Network Approach to Forecast Hourly Intense Rainfall Using GNSS Precipitable Water Vapor and Meteorological Sensors. *Remote Sensing*, *11*(8), 966, https://doi.org/10.3390/rs11080966.

Bengtsson, L. (2010). The global atmospheric water cycle. *Environmental Research Letters*, *5*(2), https://doi.org/10.1088/1748-9326/5/2/025002.

Bennitt, G. V. & Jupp, A. (2012). Operational assimilation of GPS zenith total delay observations into the Met Office numerical weather prediction models. *Monthly Weather Review*, *140*(8), 2706–2719, https://doi.org/10.1175/MWR-D-11-00156.1.

Bertiger, W., et al. (2020). GipsyX/RTGx, a new tool set for space geodetic operations and research. *Advances in Space Research*, *66*(3), 469–489, https://doi.org/10.1016/j.asr.2020.04.015.

Bevis, M., Businger, S., Chiswell, S., Herring, T. A., Anthes, R. A., Rocken, C., & Ware, R. H. (1994). GPS meteorology: Mapping zenith wet delays onto precipitable water. *Journal of Applied Meteorology*, *33*(3), 379–386, https://doi.org/10.1175/1520-0450(1994)033<0379:GMMZWD>2.0.CO;2.

Bevis, M., Businger, S., Herring, T. A., Rocken, C., Anthes, R. A., & Ware, R. H. (1992). GPS meteorology: Remote sensing of atmospheric water vapor using the global positioning system. *Journal of Geophysical Research: Atmospheres*, *97*(D14), 15787–15801, https://doi.org/10.1029/92JD01517.

Bianchi, A. R. & Yañez, C. (1992). Las precipitaciones en el noroeste argentino. *Instituto Nacional de Tecnologia Agropecuaria, Estacíon Experimental Agropecuaria Salta, Argentina.*

Bilich, A., Larson, K. M., & Axelrad, P. (2008). Modeling GPS phase multipath with SNR: Case study from the Salar de Uyuni, Boliva. *Journal of Geophysical Research: Solid Earth*, *113*(B4), https://doi.org/10.1029/2007JB005194.

Blewitt, G., Hammond, W. C., & Kreemer, C. (2018). Harnessing the GPS data explosion for interdisciplinary science. *Eos*, *99*, 485, https://doi.org/10.1029/2018EO104623.

Boers, N., Barbosa, H. M., Bookhagen, B., Marengo, J. A., Marwan, N., & Kurths, J. (2015a). Propagation of strong rainfall events from southeastern South America to the central Andes. *Journal of Climate*, *28*(19), 7641–7658, https://doi.org/10.1175/JCLI-D-15-0137.1.

Boers, N., Bookhagen, B., Barbosa, H. M., Marwan, N., Kurths, J., & Marengo, J. A. (2014). Prediction of extreme floods in the eastern Central Andes based on a complex networks approach. *Nature Communications*, *5*(1), 1–7, https://doi.org/10.1038/ncomms6199.

Boers, N., Bookhagen, B., Marengo, J., Marwan, N., von Storch, J.-S., & Kurths, J. (2015b). Extreme rainfall of the South American monsoon system: a dataset comparison using complex networks. *Journal of Climate*, *28*(3), 1031–1056, https://doi.org/10.1175/JCLI-D-14-00340.1.

Böhm, J., Niell, A., Tregoning, P., & Schuh, H. (2006a). Global Mapping Function (GMF): A new empirical mapping function based on numerical weather model data. *Geophysical Research Letters*, *33*(7), https://doi.org/10.1029/2005GL025546.

Böhm, J., Werl, B., & Schuh, H. (2006b). Troposphere mapping functions for GPS and very long baseline interferometry from European Centre for Medium-Range Weather Forecasts operational analysis data. *Journal of Geophysical Research: Solid Earth*, *111*(B2), https://doi.org/10.1029/2005JB003629.

Bona, P., Starck, D., Galli, C., Gasparini, Z., & Reguero, M. (2014). Caiman cf. latirostris (Alligatoridae, Caimaninae) in the late Miocene Palo Pintado Formation, Salta Province, Argentina: paleogeographic and paleoenvironmental considerations. *Ameghiniana*, *51*(1), 26–36, https://doi.org/10.5710/AMEGH.11.12.2013.1507.

Bookhagen, B. (2010). Appearance of extreme monsoonal rainfall events and their impact on erosion in the Himalaya. *Geomatics, Natural Hazards and Risk*, *1*(1), 37–50, https://doi.org/10.1080/19475701003625737.

Bookhagen, B. & Strecker, M. R. (2008). Orographic barriers, high-resolution TRMM rainfall, and relief variations along the eastern Andes. *Geophysical Research Letters*, *35*(6), https://doi.org/10.1029/2007GL032011.

Bookhagen, B. & Strecker, M. R. (2012). Spatiotemporal trends in erosion rates across a pronounced rainfall gradient: Examples from the southern Central Andes. *Earth and Planetary Science Letters*, *327*, 97–110, https://doi.org/10.1029/2009JF001426.

Borowitz, M. (2016). Is It Time for Commercial Weather Satellites? Analyzing the Case of Global Navigation Satellite System Radio Occultation. *New Space*, *4*(2), 115–122, https://doi.org/10.1089/space.2015.0020.

Braasch, M. S. (2017). Multipath. In *Springer Handbook of Global Navigation Satellite Systems* (pp. 443–468). Springer. https://doi.org/10.1007/978-3-319-42928-1_15.

Brocca, L., Ponziani, F., Moramarco, T., Melone, F., Berni, N., & Wagner, W. (2012). Improving landslide forecasting using ASCAT-derived soil moisture data: A case study of the Torgiovannetto landslide in central Italy. *Remote Sensing*, *4*(5), 1232–1244, https://doi.org/10.3390/rs4051232.

Brush, S. B. (1982). The Natural and Human Environment of the Central Andes. *Mountain Research and Development*, (pp. 19–38).

Butterworth, S. (1930). On the theory of filter amplifiers. *Wireless Engineer*, *7*(6), 536–541.

Campbell, J. B. & Wynne, R. H. (2011). *Introduction to Remote Sensing*. Guilford Press. ISBN 978-1-60918-176-5.

Camps, A., Park, H., Sekulic, I., & Rius, J. M. (2017). GNSS-R altimetry performance analysis for the GEROS experiment on board the international space station. *Sensors*, *17*(7), 1583, https://doi.org/10.3390/s17071583.

Cardellach, E., Fabra, F., Nogués-Correig, O., Oliveras, S., Ribó, S., & Rius, A. (2011). GNSS-R ground-based and airborne campaigns for ocean, land, ice, and snow techniques: Application to the GOLD-RTR data sets. *Radio Science*, *46*(6), 1–16, https://doi.org/10.1029/2011RS004683.

Carreno-Luengo, H., Camps, A., Ramos-Perez, I., & Rius, A. (2014). Experimental evaluation of GNSS-reflectometry altimetric precision using the P (Y) and C/A signals. *IEEE Journal of Selected Topics in Applied Earth Observations and Remote Sensing*, *7*(5), 1493–1500, https://doi.org/10.1109/JSTARS.2014.2320298.

Carvalho, L. M. V., Jones, C., Posadas, A. N., Quiroz, R., Bookhagen, B., & Liebmann, B. (2012). Precipitation characteristics of the South American monsoon system derived from multiple datasets. *Journal of Climate*, *25*(13), 4600–4620, https://doi.org/10.1175/JCLI-D-11-00335.1.

Castino, F., Bookhagen, B., & de la Torre, A. (2020). Atmospheric dynamics of extreme discharge events from 1979 to 2016 in the southern Central Andes. *Climate Dynamics*, *55*(11), 3485–3505, https://doi.org/10.1080/19475701003625737.

Castino, F., Bookhagen, B., & Strecker, M. R. (2016). River-discharge dynamics in the Southern Central Andes and the 1976–77 global climate shift. *Geophysical Research Letters*, *43*(22), 11–679, https://doi.org/10.1002/2016GL070868.

Castino, F., Bookhagen, B., & Strecker, M. R. (2017). Rainfall variability and trends of the past six decades (1950-2014) in the subtropical NW Argentine Andes. *Climate Dynamics*, *48*(3), 1049–1067, https://doi.org/10.1007/s00382-016-3127-2.

Chahine, M. T. (1992). The hydrological cycle and its influence on climate. *Nature*, *359*(6394), 373–380, https://doi.org/10.1038/359373a0.

Chen, G. & Herring, T. A. (1997). Effects of atmospheric azimuthal asymmetry on the analysis of space geodetic data. *Journal of Geophysical Research: Solid Earth*, *102*(B9), 20489–20502, https://doi.org/10.1029/97JB01739.

Chew, C., Reager, J. T., & Small, E. (2018). CYGNSS data map flood inundation during the 2017 Atlantic hurricane season. *Scientific Reports*, *8*(1), 1–8, https://doi.org/10.1038/s41598-018-27673-x.

Chew, C. & Small, E. (2018). Soil moisture sensing using spaceborne GNSS reflections: Comparison of CYGNSS reflectivity to SMAP soil moisture. *Geophysical Research Letters*, *45*(9), 4049–4057, https://doi.org/10.1029/2018GL077905.

Chew, C., Small, E. E., & Larson, K. M. (2016). An algorithm for soil moisture estimation using GPS-interferometric reflectometry for bare and vegetated soil. *GPS Solutions*, *20*(3), 525–537, https://doi.org/10.1007/s10291-015-0462-4.

Chew, C. C., Small, E. E., Larson, K. M., & Zavorotny, V. U. (2014). Effects of Near-Surface Soil Moisture on GPS SNR Data: Development of a Retrieval Algorithm for Soil Moisture. *IEEE Transactions on Geoscience and Remote Sensing*, *52*(1), 537–543, https://doi.org/10.1109/TGRS.2013.2242332.

China Satellite Navigation Office (2019). *BeiDou Navigation Satellite System Signal In Space Interface Control Document - Open Service Signal B1I (Version 3.0)*. Technical report, China Satellite Navigation Office. Available online: http://en.beidou.gov.cn/SYSTEMS/ICD/20190 2/P020190227702348791891.pdf. Accessed: 05.05.2021.

Clarizia, M. P., Pierdicca, N., Costantini, F., & Floury, N. (2019). Analysis of CYGNSS data for soil moisture retrieval. *IEEE Journal of Selected Topics in Applied Earth Observations and Remote Sensing*, *12*(7), 2227–2235, https://doi.org/10.1109/JSTARS.2019.2895510.

Clauset, A., Rohilla Shalizi, C., & Newman, M. E. J. (2009). Power-Law Distributions in Empirical Data. *SIAM Review*, *51*(4), 661–703, https://doi.org/10.1137/070710111.

Commins, R. & Janssen, V. (2012). Improving GNSS CORS Design: The CORSnet-NSW Adjustable Antenna Mount (CAAM). *Journal of Global Positioning Systems*, *11*(2), 109–115, https://doi.org/10.5081/jgps.11.2.109.

Corral, Á., Ossó, A., & Llebot, J. E. (2010). Scaling of tropical-cyclone dissipation. *Nature Physics*, *6*(9), 693–696, https://doi.org/10.1038/nphys1725.

Cucurull, L., Anthes, R., & Tsao, L.-L. (2014). Radio Occultation Observations as Anchor Observations in Numerical Weather Prediction Models and Associated Reduction of Bias Corrections in Microwave and Infrared Satellite Observations. *Journal of Atmospheric and Oceanic Technology*, *31*(1), 20–32, https://doi.org/10.1175/JTECH-D-13-00059.1.

de Carvalho, L. M. V. & Cavalcanti, I. F. (2016). The South American Monsoon System (SAMS). *The Monsoons and Climate Change*, (pp. 121–148)., https://doi.org/10.1007/978-3-319-216 50-8_6.

de Rosnay, P., Balsamo, G., Albergel, C., Muñoz-Sabater, J., & Isaksen, L. (2014). Initialisation of land surface variables for numerical weather prediction. *Surveys in Geophysics*, *35*(3), 607–621, https://doi.org/10.1007/s10712-012-9207-x.

Desilets, D., Zreda, M., & Ferré, T. P. (2010). Nature's neutron probe: Land surface hydrology at an elusive scale with cosmic rays. *Water Resources Research*, *46*(11), https://doi.org/10.1029/2009WR008726.

Di Matteo, S., Viall, N. M., & Kepko, L. (2021). Power Spectral Density Background Estimate and Signal Detection via the Multitaper Method. *Journal of Geophysical Research: Space Physics*, *126*(2), https://doi.org/10.1029/2020ja028748.

Didan, K. (2015). MOD13A3 MODIS/Terra vegetation indices monthly L3 global 1km SIN grid V006. https://doi.org/10.5067/MODIS/MOD13A3.006.

Dirmeyer, P. A. & Halder, S. (2016). Sensitivity of numerical weather forecasts to initial soil moisture variations in CFSv2. *Weather and Forecasting*, *31*(6), 1973–1983, https://doi.org/10.1175/WAF-D-16-0049.1.

Douša, J., Václavovic, P., Zhao, L., & Kačmařík, M. (2018). New adaptable all-in-one strategy for estimating advanced tropospheric parameters and using real-time orbits and clocks. *Remote Sensing*, *10*(2), 232, https://doi.org/10.3390/rs10020232.

Drusch, M. (2007). Initializing numerical weather prediction models with satellite-derived surface soil moisture: Data assimilation experiments with ECMWF's Integrated Forecast System and the TMI soil moisture data set. *Journal of Geophysical Research: Atmospheres*, *112*(D3), https://doi.org/10.1029/2006JD007478.

Durkee, J. D., Mote, T. L., & Shepherd, J. M. (2009). The contribution of mesoscale convective complexes to rainfall across subtropical South America. *Journal of Climate*, *22*(17), 4590–4605, https://doi.org/10.1175/2009JCLI2858.1.

E. Bowler, N. (2020). An assessment of GNSS radio occultation data produced by Spire. *Quarterly Journal of the Royal Meteorological Society*, *146*(733), 3772–3788, https://doi.org/10.1002/qj.3872.

Elazab, M. (2015). Integrated Cooperative Localization in VANETs for GPS Denied Environments (PhD Thesis) (p. 8). Queen's University, Kingston, Canada. Available online: https://qspace.library.queensu.ca/handle/1974/13789. Accessed: 08.02.2023.

Elgered, G. & Wickert, J. (2017). Monitoring of the Neutral Atmosphere. In *Springer Handbook of Global Navigation Satellite Systems* (pp. 1109–1138). Springer. https://doi.org/10.1007/978-3-319-42928-1_38.

Ellingson, S., Bunton, J., & Bell, J. (2000). Suppression of GLONASS signals using Parametric Signal Modelling. In *Proc. Workshop on the Applications of Radio Science (WARSOO), National Committee for Radio Science* (pp. 176–181).: Citeseer.

Entekhabi, D., et al. (2010). The soil moisture active passive (SMAP) mission. *Proceedings of the IEEE*, *98*(5), 704–716, https://doi.org/10.1109/JPROC.2010.2043918.

ESA (2021). TechDemoSat-1. Available online: https://directory.eoportal.org/web/eoportal/satellite-missions/t/techdemosat-1. Accessed: 21.05.2021.

Ewen, T., Grant, A., & Brönnimann, S. (2008). A Monthly Upper-Air Dataset for North America Back to 1922 from the Monthly Weather Review. *Monthly Weather Review*, *136*(5), 1792–1805, https://doi.org/10.1175/2007MWR2202.1.

Falcone, M., Hahn, J., & Burger, T. (2017). Galileo. In *Springer Handbook of Global Navigation Satellite Systems* (pp. 247–272). Springer. https://doi.org/10.1007/978-3-319-42928-1_9.

Fang, B. T. (1986). Trilateration and extension to global positioning system navigation. *Journal of Guidance, Control, and Dynamics*, *9*(6), 715–717.

Fersch, B., et al. (2020). A dense network of cosmic-ray neutron sensors for soil moisture observation in a highly instrumented pre-Alpine headwater catchment in Germany. *Earth System Science Data*, *12*(3), 2289–2309, https://doi.org/10.5194/essd-12-2289-2020.

Foth, A. & Pospichal, B. (2017). Optimal estimation of water vapour profiles using a combination of Raman lidar and microwave radiometer. *Atmospheric Measurement Techniques*, *10*(9), 3325–3344, https://doi.org/10.5194/amt-10-3325-2017.

Foti, G., Gommenginger, C., Jales, P., Unwin, M., Shaw, A., Robertson, C., & Rosello, J. (2015). Spaceborne GNSS reflectometry for ocean winds: First results from the UK TechDemoSat-1 mission. *Geophysical Research Letters*, *42*(13), 5435–5441, https://doi.org/10.1002/2015GL064204.

Gandu, A. W. & Silva Dias, P. L. (1998). Impact of tropical heat sources on the South American tropospheric upper circulation and subsidence. *Journal of Geophysical Research: Atmospheres*, *103*(D6), 6001–6015, https://doi.org/10.1029/97JD03114.

Garreaud, R. D., Vuille, M., Compagnucci, R., & Marengo, J. (2009). Present-day South American climate. *Palaeogeography, Palaeoclimatology, Palaeoecology*, *281*(3-4), 180–195, https://doi.org/10.1016/j.palaeo.2007.10.032.

Gebre-Egziabher, D. & Gleason, S. (2009). *GNSS Applications and Methods*. Artech House. ISBN 978-1-59693-329-3.

Gendt, G., Dick, G., Reigber, C., Tomassini, M., Liu, Y., & Ramatschi, M. (2004). Near real time GPS water vapor monitoring for numerical weather prediction in Germany. *Journal of the Meteorological Society of Japan. Ser. II*, *82*(1B), 361–370, https://doi.org/10.2151/jmsj.2004.361.

GFZ German Research Centre for Geosciences (2021). "Earth Parameter and Orbit System" software EPOS. Available online: https://www.gfz-potsdam.de/en/section/global-geomonitoring-and-gravity-field/topics/earth-system-parameters-and-orbit-dynamics/earth-parameter-and-orbit-system-software-epos. Accessed: 04.08.2021.

Giraldez, A. E. (2003). SAOCOM-1 Argentina L-band SAR Mission Overview. In *Coastal and Marine Applications of SAR Symposium*, volume 565 (pp.$\tilde{2}$7).

Gleason, S. & Ruf, C. (2015). Overview of the Delay Doppler Mapping Instrument (DDMI) for the cyclone global navigation satellite systems mission (CYGNSS). In *2015 IEEE MTT-S International Microwave Symposium* (pp. 1–4).: IEEE. https://doi.org/10.1109/MWSYM.2015.7166775.

Gleisner, H., Ringer, M. A., & Healy, S. B. (2022). Monitoring global climate change using GNSS radio occultation. *npj Climate and Atmospheric Science*, *5*(1), 1–4, https://doi.org/10.1038/s41612-022-00229-7.

Glickman, T. S. & Zenk, W. (2000). *Glossary of Meteorology*. AMS (American Meteorological Society). ISBN 978-1-87-822034-9.

Gorbunov, M. E. & Sokolovskiy, S. V. (1993). *Remote sensing of refractivity from space for global observations of atmospheric parameters*. Technical Report 119, Max-Planck-Institut für Meteorologie.

Görres, B., Campbell, J., Becker, M., & Siemes, M. (2006). Absolute calibration of GPS antennas: laboratory results and comparison with field and robot techniques. *GPS Solutions*, *10*(2), 136–145, https://doi.org/10.1007/s10291-005-0015-3.

Griffiths, J. & Ray, J. R. (2009). On the precision and accuracy of IGS orbits. *Journal of Geodesy*, *83*(3), 277–287, https://doi.org/10.1007/s00190-008-0237-6.

Gurtner, W. & Lou, E. (2018). *RINEX The Receiver Independent Exchange Format (Version 3.04)*. Technical report, Astronomical Institute, University of Bern. Available online: http://acc.igs.org/misc/rinex304.pdf. Accessed: 13.05.2021.

GYGNSS (2020). CYGNSS Level 1 Full Delay Doppler Map Data Record Version 3.0. Ver. 3.0. PO.DAAC, CA, USA. Available online: https://doi.org/10.5067/CYGNS-L1F30. Accessed: 26.05.2021.

Hajj, G. A., Kursinski, E., Romans, L., Bertiger, W., & Leroy, S. (2002). A technical description of atmospheric sounding by GPS occultation. *Journal of Atmospheric and Solar-Terrestrial Physics*, *64*(4), 451–469, https://doi.org/10.1016/S1364-6826(01)00114-6.

Hartmann, T. & Wenzel, H.-G. (1995). The HW95 tidal potential catalogue. *Geophysical Research Letters*, *22*(24), 3553–3556, https://doi.org/10.1029/95GL03324.

Hathaway, D. H. (2015). The Solar Cycle. *Living Reviews in Solar Physics*, *12*(1), 1–87, https://doi.org/10.1007/lrsp-2015-4.

Hauschild, A. (2017a). Basic Observation Equations. In *Springer Handbook of Global Navigation Satellite Systems* (pp. 561–582). Springer. https://doi.org/10.1007/978-3-319-42928-1_19.

Hauschild, A. (2017b). Combinations of Observations. In *Springer Handbook of Global Navigation Satellite Systems* (pp. 583–604). Springer. https://doi.org/10.1007/978-3-319-42928-1_20.

Healy, S., Jupp, A., & Marquardt, C. (2005). Forecast impact experiment with GPS radio occultation measurements. *Geophysical Research Letters*, *32*(3), https://doi.org/10.1029/2004GL020806.

Hegarty, C. J. (2017). The Global Positioning System (GPS). In *Springer Handbook of Global Navigation Satellite Systems* (pp. 197–218). Springer. https://doi.org/10.1007/978-3-319-42928-1_7.

Hein, G. W., Godet, J., Issler, J.-L., Martin, J.-C., Lucas-Rodriguez, R., & Pratt, T. (2001). The Galileo frequency structure and signal design. In *Proceedings of the 14th International Technical Meeting of the Satellite Division of The Institute of Navigation (ION GPS 2001)* (pp. 1273–1282).

Heistermann, M., et al. (2023). Three years of soil moisture observations by a dense cosmic-ray neutron sensing cluster at an agricultural research site in north-east Germany. *Earth System Science Data*, *15*(7), 3243–3262, https://doi.org/10.5194/essd-15-3243-2023.

Hersbach, H., et al. (2020). The ERA5 global reanalysis. *Quarterly Journal of the Royal Meteorological Society*, *146*(730), 1999–2049, https://doi.org/10.1002/qj.3803.

Hildebrandt, A. & Eltahir, E. A. (2008). Using a horizontal precipitation model to investigate the role of turbulent cloud deposition in survival of a seasonal cloud forest in Dhofar. *Journal of Geophysical Research: Biogeosciences*, *113*(G4), https://doi.org/10.1029/2008JG000727.

Ho, S.-p., et al. (2009). Estimating the uncertainty of using GPS radio occultation data for climate monitoring: Intercomparison of CHAMP refractivity climate records from 2002 to 2006 from different data centers. *Journal of Geophysical Research: Atmospheres*, *114*(D23), https://doi.org/10.1029/2009JD011969.

Hobiger, T. & Jakowski, N. (2017). Atmospheric Signal Propagation. In *Springer Handbook of Global Navigation Satellite Systems* (pp. 165–193). Springer. https://doi.org/10.1007/978-3-319-42928-1_6.

Hofmann-Wellenhof, B., Lichtenegger, H., & Wasle, E. (2008). *GNSS - Global Navigation Satellite Systems: GPS, GLONASS, Galileo, and more*. Wien, Austria: Springer. ISBN 978-3-211-73017-1.

Hopfield, H. (1969). Two-quartic tropospheric refractivity profile for correcting satellite data. *Journal of Geophysical Research*, *74*(18), 4487–4499, https://doi.org/10.1029/JC074i018p04487.

Hu, S. & Vallis, G. K. (2019). Meridional structure and future changes of tropopause height and temperature. *Quarterly Journal of the Royal Meteorological Society*, *145*(723), 2698–2717, https://doi.org/10.1002/qj.3587.

Huffman, G., Stocker, E., Bolvin, D., Nelkin, E., & Jackson, T. (2019). GPM IMERG Final Precipitation L3 1 day 0.1 degree x 0.1 degree V06. Edited by Andrey Savtchenko, Greenbelt, MD, Goddard Earth Sciences Data and Information Services Center (GES DISC). Accessed: 29.11.2022.

INSIDE GNSS (2010). Measuring GNSS Signal Strength. Available online: https://insidegnss.com/measuring-gnss-signal-strength. Accessed: 13.05.2021.

Instituto Nacional de Tecnología Agropecuaria (2022). Sistema de Información y Gestión Agrometeorológica. Available online: http://siga.inta.gob.ar/.

Itzerott, S., et al. (2018). TERENO (Northeast), Soil moisture stations of the GFZ German Research Centre for Geoscienes (GFZ). https://doi.org/10.5880/TERENO.GFZ.SM.2018.ALL.

Jakowski, N., Wehrenpfennig, A., Heise, S., Reigber, C., Lühr, H., Grunwaldt, L., & Meehan, T. (2002). GPS radio occultation measurements of the ionosphere from CHAMP: Early results. *Geophysical Research Letters*, *29*(10), 95–1–95–4, https://doi.org/10.1029/2001GL014364.

Jia, J., Yan, W., Chen, X., & Liu, W. (2019). Characteristics of Horizontal Precipitation in Semi-Humid Forestland in Northern China. *Water*, *11*(5), 975, https://doi.org/10.3390/w11050975.

Jin, S., Cardellach, E., & Xie, F. (2014a). Atmospheric Sensing Using GNSS RO. In *GNSS Remote Sensing. Remote Sensing and Digital Image Processing*, volume 19 (pp. 121–157). Springer. https://doi.org/10.1007/978-94-007-7482-7_6.

Jin, S., Cardellach, E., & Xie, F. (2014b). Ground GNSS Atmospheric Sensing. In *GNSS Remote Sensing. Remote Sensing and Digital Image Processing*, volume 19 (pp. 33–60). Springer. https://doi.org/10.1007/978-94-007-7482-7_3.

Jin, S., Cardellach, E., & Xie, F. (2014c). Hydrology and Vegetation Remote Sensing. In *GNSS Remote Sensing. Remote Sensing and Digital Image Processing*, volume 19 (pp. 241–250). Springer. https://doi.org/10.1007/978-94-007-7482-7_10.

Johnston, G., Riddell, A., & Hausler, G. (2017). The International GNSS Service. In *Springer Handbook of Global Navigation Satellite Systems* (pp. 967–982). Springer. https://doi.org/10.1007/978-3-319-42928-1_33.

Jones, J., Guerova, G., Douša, J., Dick, G., de Haan, S., Pottiaux, E., & van Malderen, R. (2019). *Advanced GNSS tropospheric products for monitoring severe weather events and climate*. Cham, Switzerland: Springer. ISBN 978-3-030-13900-1.

Jones, J. N., Boulton, S. J., Stokes, M., Bennett, G. L., & Whitworth, M. R. Z. (2021). 30-year record of Himalaya mass-wasting reveals landscape perturbations by extreme events. *Nature Communications*, *12*(1), 1–15, https://doi.org/10.1038/s41467-021-26964-8.

Juang, J.-C., Lin, C.-T., & Tsai, Y.-F. (2020). Comparison and Synergy of BPSK and BOC Modulations in GNSS Reflectometry. *IEEE Journal of Selected Topics in Applied Earth Observations and Remote Sensing*, *13*, 1959–1971, https://doi.org/10.1109/JSTARS.2020.2989824.

Kačmařík, M., Douša, J., Zus, F., Václavovic, P., Balidakis, K., Dick, G., & Wickert, J. (2019). Sensitivity of GNSS tropospheric gradients to processing options. In *Annales Geophysicae*, volume 37 (pp. 429–446).: Copernicus GmbH. https://doi.org/10.5194/angeo-37-429-2019.

Kerr, Y. H., et al. (2010). The SMOS mission: New tool for monitoring key elements of the global water cycle. *Proceedings of the IEEE*, *98*(5), 666–687, https://doi.org/10.1109/JPROC.2010.2043032.

Khorram, S., Koch, F. H., van der Wiele, C. F., & Nelson, S. A. (2012). *Remote Sensing*. Springer Science & Business Media. ISBN 978-1-4614-3102-2.

Kodama, Y. (1992). Large-scale common features of subtropical precipitation zones (the Baiu frontal zone, the SPCZ, and the SACZ) Part I: Characteristics of subtropical frontal zones. *Journal of the Meteorological Society of Japan. Ser. II*, *70*(4), 813–836, https://doi.org/10.2151/jmsj1965.70.4_813.

Köhli, M., Schrön, M., Zreda, M., Schmidt, U., Dietrich, P., & Zacharias, S. (2015). Footprint characteristics revised for field-scale soil moisture monitoring with cosmic-ray neutrons. *Water Resources Research*, *51*(7), 5772–5790, https://doi.org/10.1002/2015WR017169.

Komma, J., Blöschl, G., & Reszler, C. (2008). Soil moisture updating by Ensemble Kalman Filtering in real-time flood forecasting. *Journal of Hydrology*, *357*(3-4), 228–242, https://doi.org/10.1016/j.jhydrol.2008.05.020.

Kouba, J. (2008). Implementation and testing of the gridded Vienna Mapping Function 1 (VMF1). *Journal of Geodesy*, *82*(4-5), 193–205, https://doi.org/10.1007/s00190-007-0170-0.

Krawinkel, T. & Schön, S. (2016). Benefits of receiver clock modeling in code-based GNSS navigation. *GPS Solutions*, *20*(4), 687–701, https://doi.org/10.1007/s10291-015-0480-2.

Kuo, Y.-H., Sokolovskiy, S. V., Anthes, R. A., & Vandenberghe, F. (2000). Assimilation of GPS radio occultation data for numerical weather prediction. *Terrestrial Atmospheric and Oceanic Sciences*, *11*(1), 157–186, https://doi.org/10.3319/TAO.2000.11.1.157(COSMIC).

Kursinski, E. (1997). The GPS radio occultation concept: Theoretical performance and initial results (PhD Thesis) (pp. 2-1–2-42). California Institute of Technology, Pasadena, California, USA. Available online: https://thesis.library.caltech.edu/7448. Accessed: 08.02.2023.

Kursinski, E., Hajj, G., Schofield, J., Linfield, R., & Hardy, K. R. (1997). Observing Earth's atmosphere with radio occultation measurements using the Global Positioning System. *Journal of Geophysical Research: Atmospheres*, *102*(D19), 23429–23465, https://doi.org/10.1029/97JD01569.

Lange, N. A. & Speight, J. G. (2005). *Lange's handbook of chemistry*, volume 1. Mcgraw-hill New York. ISBN 978-0-0714-3220-7.

Langley, R. B., Teunissen, P. J., & Montenbruck, O. (2017). Introduction to GNSS. In *Springer Handbook of Global Navigation Satellite Systems* (pp. 3–23). Springer. https://doi.org/10.1007/978-3-319-42928-1_1.

Larson, K. M., Braun, J. J., Small, E. E., Zavorotny, V. U., Gutmann, E. D., & Bilich, A. L. (2009). GPS multipath and its relation to near-surface soil moisture content. *IEEE Journal of Selected Topics in Applied Earth Observations and Remote Sensing*, *3*(1), 91–99, https://doi.org/10.1109/JSTARS.2009.2033612.

Larson, K. M. & Small, E. E. (2013). Using GPS to Study The Terrestrial Water Cycle. *EOS, Transactions American Geophysical Union*, *94*(52), 505–506.

Larson, K. M., Small, E. E., Gutmann, E., Bilich, A., Axelrad, P., & Braun, J. (2008a). Using GPS multipath to measure soil moisture fluctuations: initial results. *GPS Solutions*, *12*(3), 173–177, https://doi.org/10.1007/s10291-007-0076-6.

Larson, K. M., Small, E. E., Gutmann, E. D., Bilich, A. L., Braun, J. J., & Zavorotny, V. U. (2008b). Use of GPS receivers as a soil moisture network for water cycle studies. *Geophysical Research Letters*, *35*(24), https://doi.org/10.1029/2008GL036013.

Leckner, B. (1978). The spectral distribution of solar radiation at the Earth's surface—elements of a model. *Solar Energy*, *20*(2), 143–150.

Li, X., et al. (2015). Retrieving of atmospheric parameters from multi-GNSS in real time: Validation with water vapor radiometer and numerical weather model. *Journal of Geophysical Research: Atmospheres*, *120*(14), 7189–7204, https://doi.org/10.1002/2015JD023454.

Liou, Y.-A., Pavelyev, A. G., Liu, S.-F., Pavelyev, A. A., Yen, N., Huang, C.-Y., & Fong, C.-J. (2007). FORMOSAT-3/COSMIC GPS radio occultation mission: Preliminary results. *IEEE Transactions on Geoscience and Remote Sensing*, *45*(11), 3813–3826, https://doi.org/10.1109/TGRS.2007.903365.

Liu, W., et al. (2017). Coastal Sea-Level Measurements Based on GNSS-R Phase Altimetry: A Case Study at the Onsala Space Observatory, Sweden. *IEEE Transactions on Geoscience and Remote Sensing*, *55*(10), 5625–5636, https://doi.org/10.1109/TGRS.2017.2711012.

Liu, W. S. (2020). Comparison of the greenhouse effect between Earth and Venus using multiple atmospheric layer models. In *E3S Web of Conferences*, volume 167: EDP Sciences. https://doi.org/10.1051/e3sconf/202016704002.

Liu, Z., Li, Y., Guo, J., & Li, F. (2016). Influence of higher-order ionospheric delay correction on GPS precise orbit determination and precise positioning. *Geodesy and Geodynamics*, *7*(5), 369–376, https://doi.org/10.1016/j.geog.2016.06.005.

Lomb, N. R. (1976). Least-squares frequency analysis of unequally spaced data. *Astrophysics and Space Science*, *39*(2), 447–462, https://doi.org/10.1007/BF00648343.

Lorenz, R. D. (2009). Power law of dust devil diameters on Mars and Earth. *Icarus*, *203*(2), 683–684, https://doi.org/10.1016/j.icarus.2009.06.029.

Loria, E., O'Brien, A., Zavorotny, V., Lavalle, M., Chew, C., Shah, R., & Zuffada, C. (2019). Analysis of wetland extent retrieval accuracy using CYGNSS. In *IGARSS 2019-2019 IEEE International Geoscience and Remote Sensing Symposium* (pp. 8684–8687).: IEEE. https://doi.org/10.1109/IGARSS.2019.8898132.

Lu, J., Guo, X., & Su, C. (2020). Global capabilities of BeiDou Navigation Satellite System. *Satellite Navigation*, *1*(27), https://doi.org/10.1186/s43020-020-00025-9.

Mader, G. L. (1999). GPS antenna calibration at the National Geodetic Survey. *GPS Solutions*, *3*(1), 50–58, https://doi.org/10.1007/PL00012780.

Maqsood, M., Gao, S., & Montenbruck, O. (2017). Antennas. In *Springer Handbook of Global Navigation Satellite Systems* (pp. 505–534). Springer. https://doi.org/10.1007/978-3-319-42928-1_17.

Marengo, J. A., et al. (2012). Recent developments on the South American monsoon system. *International Journal of Climatology*, *32*(1), 1–21, https://doi.org/10.1002/joc.2254.

Marengo, J. A., Soares, W. R., Saulo, C., & Nicolini, M. (2004). Climatology of the low-level jet east of the Andes as derived from the NCEP–NCAR reanalyses: Characteristics and temporal variability. *Journal of Climate*, *17*(12), 2261–2280, https://doi.org/10.1175/1520-0442(2004)017<2261:COTLJE>2.0.CO;2.

Marini, J. W. (1972). Correction of satellite tracking data for an arbitrary tropospheric profile. *Radio Science*, *7*(2), 223–231, https://doi.org/10.1029/RS007i002p00223.

Marino, P., Peres, D. J., Cancelliere, A., Greco, R., & Bogaard, T. A. (2020). Soil moisture information can improve shallow landslide forecasting using the hydrometeorological threshold approach. *Landslides*, *17*(9), 2041–2054, https://doi.org/10.1007/s10346-020-01420-8.

Martin, F., Camps, A., Park, H., D'Addio, S., Martin-Neira, M., & Pascual, D. (2014). Cross-correlation waveform analysis for conventional and interferometric GNSS-R approaches. *IEEE Journal of Selected Topics in Applied Earth Observations and Remote Sensing*, *7*(5), 1560–1572, https://doi.org/10.1109/JSTARS.2014.2300232.

Martin-Neira, M. (1993). A passive reflectometry and interferometry system (PARIS): Application to ocean altimetry. *ESA Journal*, *17*(4), 331–355.

Massari, C., et al. (2015). The Use of H-SAF Soil Moisture Products for Operational Hydrology: Flood Modelling over Italy. *Hydrology*, *2*(1), 2–22, https://doi.org/10.3390/hydrology2010002.

MATLAB (2018). version 2018b. The MathWorks Inc. Natick, Massachusetts, USA.

Maurellis, A. & Tennyson, J. (2003). The climatic effects of water vapour. *Physics World*, *16*(5), 29, https://doi.org/10.1088/2058-7058/16/5/33.

Melbourne, W., et al. (1994). The application of spaceborne GPS to atmospheric limb sounding and global change monitoring. *JPL Publication*, *147*, 94–18.

Meng, L., et al. (2021). Continuous rise of the tropopause in the Northern Hemisphere over 1980-2020. *Science Advances*, *7*(45), eabi8065, https://doi.org/10.1126/sciadv.abi8065.

Meurer, M. & Antreich, F. (2017). Signals and Modulation. In *Springer Handbook of Global Navigation Satellite Systems* (pp. 91–119). Springer. https://doi.org/10.1007/978-3-319-42928-1_4.

Mohanty, B. P., Cosh, M. H., Lakshmi, V., & Montzka, C. (2017). Soil moisture remote sensing: State-of-the-science. *Vadose Zone Journal*, *16*(1), 1–9, https://doi.org/10.2136/vzj2016.10.0105.

Möller, G. (2017). Reconstruction of 3D wet refractivity fields in the lower atmosphere along bended GNSS signal paths (PhD Thesis) (pp. 95–127). TU Wien, Vienna, Austria. Available online: https://repositum.tuwien.at/handle/20.500.12708/10401. Accessed: 08.02.2023.

Montini, T. L., Jones, C., & Carvalho, L. M. V. (2019). The South American low-level jet: a new climatology, variability, and changes. *Journal of Geophysical Research: Atmospheres*, *124*(3), 1200–1218, https://doi.org/10.1029/2018JD029634.

Moreira, A., et al. (2015). Tandem-L: A highly innovative bistatic SAR mission for global observation of dynamic processes on the Earth's surface. *IEEE Geoscience and Remote Sensing Magazine*, *3*(2), 8–23, https://doi.org/10.1109/MGRS.2015.2437353.

Morris, M., Chew, C., Reager, J. T., Shah, R., & Zuffada, C. (2019). A novel approach to monitoring wetland dynamics using CYGNSS: Everglades case study. *Remote Sensing of Environment*, *233*, 111417, https://doi.org/10.1016/j.rse.2019.111417.

Morris, V. (2006). *Microwave radiometer (MWR) Handbook*. Technical report, DOE Office of Science Atmospheric Radiation Measurement (ARM) Program (United States). https://doi.org/10.2172/1020715.

NASA (2019). CYGNSS. Available online: https://www.nasa.gov/cygnss. Accessed: 21.05.2021.

National Weather Service (2021). Radiosonde Observation. Available online: https://www.weather.gov/upperair/factsheet. Accessed: 03.12.2021.

Navipedia (2013). Tropospheric Delay. Available online: https://gssc.esa.int/navipedia/index.php/Tropospheric_Delay. Accessed: 31.05.2021.

Navipedia (2018a). BeiDou Receivers. Available online: https://gssc.esa.int/navipedia/index.php/BeiDou_Receivers. Accessed: 23.07.2022.

Navipedia (2018b). GLONASS Future and Evolutions. Available online: https://gssc.esa.int/navipedia/index.php/GLONASS_Future_and_Evolutions. Accessed: 04.05.2021.

Navipedia (2018c). GLONASS Receivers. Available online: https://gssc.esa.int/navipedia/index.php/GLONASS_Receivers. Accessed: 23.07.2022.

Navipedia (2018d). QZSS. Available online: https://gssc.esa.int/navipedia/index.php/QZSS. Accessed: 06.05.2021.

Navipedia (2020a). Galileo Architecture. Available online: https://gssc.esa.int/navipedia/index.php/Galileo_Architecture. Accessed: 05.04.2021.

Navipedia (2020b). Galileo Signal Plan. Available online: https://gssc.esa.int/navipedia/index.php/Galileo_Signal_Plan. Accessed: 05.05.2021.

Navipedia (2020c). Galileo Space Segment. Available online: https://gssc.esa.int/navipedia/index.php/Galileo_Space_Segment. Accessed: 05.05.2021.

Navipedia (2020d). GNSS Basic Observables. Available online: https://gssc.esa.int/navipedia/index.php/GNSS_Basic_Observables. Accessed: 01.08.2022.

Navipedia (2021a). GALILEO Future and Evolutions. Available online: https://gssc.esa.int/navipedia/index.php/GALILEO_Future_and_Evolutions. Accessed: 05.05.2021.

Navipedia (2021b). NAVIC. Available online: https://gssc.esa.int/navipedia/index.php/NAVIC. Accessed: 06.05.2021.

Niell, A. E. (1996). Global mapping functions for the atmosphere delay at radio wavelengths. *Journal of Geophysical Research: Solid Earth*, *101*(B2), 3227–3246, https://doi.org/10.1029/95JB03048.

Nievinski, F. G. & Santos, M. C. (2010). Ray-tracing options to mitigate the neutral atmosphere delay in GPS. *Geomatica*, *64*(2), 191–207, https://doi.org/10.5623/geomat-2010-0020.

Nikolaidou, T., Santos, M., Williams, S., & Geremia-Nievinski, F. (2020a). Raytracing atmospheric delays in ground-based GNSS reflectometry. *Journal of Geodesy*, *94*(8), 1–12, https://doi.org/10.1007/s00190-020-01390-8.

Nikolaidou, T., Santos, M., Williams, S. D., & Geremia-Nievinski, F. (2020b). A simplification of rigorous atmospheric raytracing based on judicious rectilinear paths for near-surface GNSS reflectometry. *Earth, Planets and Space*, *72*(1), 1–10, https://doi.org/10.1186/s40623-020-01206-1.

Nischan, T. (2016). GFZRNX - RINEX GNSS Data Conversion and Manipulation Toolbox. https://doi.org/10.5880/GFZ.1.1.2016.002.

Njoku, E. G., Stacey, J., & Barath, F. T. (1980). The Seasat scanning multichannel microwave radiometer (SMMR): Instrument description and performance. *IEEE Journal of Oceanic Engineering*, *5*(2), 100–115, https://doi.org/10.1109/JOE.1980.1145458.

Ohtani, E. (2020). The role of water in Earth's mantle. *National Science Review*, *7*(1), 224–232, https://doi.org/10.1093/nsr/nwz071.

Oki, T., Entekhabi, D., & Harrold, T. I. (2004). The Global Water Cycle. In *The State of the Planet: Frontiers and Challenges in Geophysics*. American Geophysical Union. https://doi.org/10.1029/150GM18.

Oppenheim, A. V., Schafer, R. W., & Buck, J. R. (1999). *Discrete-time signal processing*. Prentice Hall. ISBN 978-0-1308-3443-0.

Owe, M., de Jeu, R., & Holmes, T. (2008). Multisensor historical climatology of satellite-derived global land surface moisture. *Journal of Geophysical Research: Earth Surface*, *113*(F1), https://doi.org/10.1029/2007JF000769.

Pierrehumbert, R. T. (1995). Thermostats, radiator fins, and the local runaway greenhouse. *Journal of Atmospheric Sciences*, *52*(10), 1784–1806, https://doi.org/10.1175/1520-0469(1995)052<1784:TRFATL>2.0.CO;2.

Piñón, D. A., Gómez, D. D., Smalley Jr, R., Cimbaro, S. R., Lauría, E. A., & Bevis, M. G. (2018). The history, state, and future of the Argentine continuous satellite monitoring network and its contributions to geodesy in Latin America. *Seismological Research Letters*, *89*(2A), 475–482, https://doi.org/10.1785/0220170162.

Ponziani, F., et al. (2013). Landwarn: An Operative Early Warning System for Landslides Forecasting Based on Rainfall Thresholds and Soil Moisture. In *Landslide Science and Practice* (pp. 627–634). Springer. https://doi.org/10.1007/978-3-642-31445-2_82.

Poveda, G., Espinoza, J. C., Zuluaga, M. D., Solman, S. A., Garreaud, R., & Van Oevelen, P. J. (2020). High impact weather events in the Andes. *Frontiers in Earth Science*, *8*, 162, https://doi.org/10.3389/feart.2020.00162.

Press, W. H. & Rybicki, G. B. (1989). Fast algorithm for spectral analysis of unevenly sampled data. *The Astrophysical Journal*, *338*, 277–280, https://doi.org/10.1086/167197.

Priego, E., Jones, J., Porres, M., & Seco, A. (2017). Monitoring water vapour with GNSS during a heavy rainfall event in the Spanish Mediterranean area. *Geomatics, Natural Hazards and Risk*, *8*(2), 282–294, https://doi.org/10.1080/19475705.2016.1201150.

Pritchard, M. (2010a). Plutons GPS Network - COLO-Laguna Colorada P.S. https://doi.org/10.7283/T5Q23XBT.

Pritchard, M. (2010b). Plutons GPS Network - UTUR-Uturuncu Volcano P.S. https://doi.org/10.7283/T5K935MG.

Pritchard, M. (2011). Plutons GPS Network - LCEN-Lazufre Center of Deformation. https://doi.org/10.7283/T53776T2.

Pritchard, M. (2012). Plutons GPS Network - SOCM-Socompa P.S. https://doi.org/10.7283/T5TT4P27.

Python (2018). version 3.7. Python Software Foundation.

Qin, H., Liu, P., Qu, J., & Cong, L. (2019). Optimal carrier-phase integer combinations for modernized triple-frequency BDS in precise point positioning. *IEEE Access*, *7*, 177449–177459, https://doi.org/10.1109/ACCESS.2019.2958204.

Ramezani Ziarani, M. (2020). Characterization of atmospheric processes related to hydrometeorological extreme events over the south-central Andes (PhD Thesis). Universität Potsdam, Potsdam, Germany. Available online: https://publishup.uni-potsdam.de/frontdoor/index/index/docId/47175. Accessed: 08.02.2023.

Ramezani Ziarani, M., Bookhagen, B., Schmidt, T., Wickert, J., de la Torre, A., Deng, Z., & Calori, A. (2021). A Model for the Relationship between Rainfall, GNSS-Derived Integrated Water Vapour, and CAPE in the Eastern Central Andes. *Remote Sensing*, *13*(18), 3788, https://doi.org/10.1785/0220170162.

Rankin, J. (1994). An error model for sensor simulation GPS and differential GPS. In *Proceedings of 1994 IEEE Position, Location and Navigation Symposium-PLANS'94* (pp. 260–266).: IEEE. https://doi.org/10.1109/PLANS.1994.303322.

Rasche, D., Köhli, M., Schrön, M., Blume, T., & Güntner, A. (2021). Towards disentangling heterogeneous soil moisture patterns in Cosmic-Ray Neutron Sensor footprints. *Hydrology and Earth System Sciences Discussions*, (pp. 1–33)., https://doi.org/10.5194/hess-2021-202.

Reddy, M. & Affholder, M. (2002). *Descriptive physical oceanography: State of the Art*. Taylor & Francis. ISBN 90-5410-706-5.

Revnivykh, S. (2011). GLONASS Status and Modernization. In *Proceedings of the 24th International Technical Meeting of the Satellite Division of the Institute of Navigation* (pp. 839–854). Portland, USA: ION GNSS.

Revnivykh, S., Bolkunov, A., Serdyukov, A., & Montenbruck, O. (2017). GLONASS. In *Springer Handbook of Global Navigation Satellite Systems* (pp. 219–245). Springer. https://doi.org/10.1007/978-3-319-42928-1_8.

Rius, A. & Cardellach, E. (2017). Reflectometry. In *Springer Handbook of Global Navigation Satellite Systems* (pp. 1163–1186). Springer. https://doi.org/10.1007/978-3-319-42928-1_40.

Rius, A., et al. (2012). Altimetry with GNSS-R interferometry: First proof of concept experiment. *GPS Solutions*, *16*(2), 231–241, https://doi.org/10.1007/s10291-011-0225-9.

Robock, A., et al. (2000). The global soil moisture data bank. *Bulletin of the American Meteorological Society*, *81*(6), 1281–1300, https://doi.org/10.1175/1520-0477(2000)081<1281:TGSMDB>2.3.CO;2.

Roche, M. A., Bourges, J., Cortes, J., & Mattos, R. (1992). Climatology and Hydrology. In *Lake Titicaca* (pp. 63–88). Springer. https://doi.org/10.1007/978-94-011-2406-5_4.

Rocken, C., et al. (1997). Analysis and validation of GPS/MET data in the neutral atmosphere. *Journal of Geophysical Research: Atmospheres*, *102*(D25), 29849–29866, https://doi.org/10.1029/97JD02400.

Rodriguez-Alvarez, N., Bosch-Lluis, X., Camps, A., Vall-Llossera, M., Valencia, E., Marchan-Hernandez, J. F., & Ramos-Perez, I. (2009). Soil moisture retrieval using GNSS-R techniques: Experimental results over a bare soil field. *IEEE transactions on geoscience and remote sensing*, *47*(11), 3616–3624, https://doi.org/10.1109/TGRS.2009.2030672.

Roesler, C. & Larson, K. M. (2018). Software tools for GNSS interferometric reflectometry (GNSS-IR). *GPS Solutions*, *22*(3), 1–10, https://doi.org/10.1007/s10291-018-0744-8.

Rohm, W. (2013). The ground GNSS tomography–unconstrained approach. *Advances in Space Research*, *51*(3), 501–513, https://doi.org/10.1016/j.asr.2012.09.021.

Rohm, W., Guzikowski, J., Wilgan, K., & Kryza, M. (2019). 4DVAR assimilation of GNSS zenith path delays and precipitable water into a numerical weather prediction model WRF. *Atmospheric Measurement Techniques*, *12*(1), 345–361, https://doi.org/10.5194/amt-12-345-2019.

Romatschke, U. & Houze, R. A. (2013). Characteristics of precipitating convective systems accounting for the summer rainfall of tropical and subtropical South America. *Journal of Hydrometeorology*, *14*(1), 25–46, https://doi.org/10.1175/JHM-D-12-060.1.

Rossel, R. V., Adamchuk, V., Sudduth, K., McKenzie, N., & Lobsey, C. (2011). Proximal soil sensing: An effective approach for soil measurements in space and time. *Advances in Agronomy*, *113*, 243–291, https://doi.org/10.1016/B978-0-12-386473-4.00005-1.

Roth, K., Schulin, R., Flühler, H., & Attinger, W. (1990). Calibration of time domain reflectometry for water content measurement using a composite dielectric approach. *Water Resources Research*, *26*(10), 2267–2273, https://doi.org/10.1029/WR026i010p02267.

Roussel, N., Frappart, F., Ramillien, G., Darrozes, J., Baup, F., Lestarquit, L., & Ha, M. C. (2016). Detection of soil moisture variations using GPS and GLONASS SNR data for elevation angles ranging from 2 to 70. *IEEE Journal of Selected Topics in Applied Earth Observations and Remote Sensing*, *9*(10), 4781–4794, https://doi.org/10.1109/JSTARS.2016.2537847.

Ruf, C., Gleason, S., Ridley, A., Rose, R., & Scherrer, J. (2017). The NASA CYGNSS mission: Overview and status update. In *2017 IEEE International Geoscience and Remote Sensing Symposium (IGARSS)* (pp. 2641–2643).: IEEE. https://doi.org/10.1109/IGARSS.2017.8127537.

Ruf, C. S. & Balasubramaniam, R. (2018). Development of the CYGNSS Geophysical Model Function for Wind Speed. *IEEE Journal of Selected Topics in Applied Earth Observations and Remote Sensing*, *12*(1), 66–77, https://doi.org/10.1109/JSTARS.2018.2833075.

Saastamoinen, J. (1972). Atmospheric correction for the troposphere and stratosphere in radio ranging satellites. *The Use of Artificial Satellites for Geodesy*, *15*, 247–251, https://doi.org/10.1029/GM015p0247.

Salio, P., Nicolini, M., & Saulo, A. C. (2002). Chaco low-level jet events characterization during the austral summer season. *Journal of Geophysical Research: Atmospheres*, *107*, https://doi.org/10.1029/2001JD001315.

Salio, P., Nicolini, M., & Zipser, E. J. (2007). Mesoscale Convective Systems over Southeastern South America and Their Relationship with the South American Low-Level Jet. *Monthly Weather Review*, *135*(4), 1290–1309, https://doi.org/10.1175/MWR3305.1.

Scargle, J. D. (1982). Studies in astronomical time series analysis. II-Statistical aspects of spectral analysis of unevenly spaced data. *The Astrophysical Journal*, *263*, 835–853, https://doi.org/10.1086/160554.

Schmid, R., Dach, R., Collilieux, X., Jäggi, A., Schmitz, M., & Dilssner, F. (2016). Absolute IGS antenna phase center model igs08. atx: status and potential improvements. *Journal of Geodesy*, *90*(4), 343–364, https://doi.org/10.1007/s00190-015-0876-3.

Schmidt, T., Arras, C., Beyerle, G., Heise, S., Wickert, J., & Rothacher, M. (2008). Trends in the global tropopause estimated from GPS radio occultation data. *37th COSPAR Scientific Assembly*, *37*, 2778, https://doi.org/10.1029/2008GL034012.

Schreiner, W. S., Sokolovskiy, S. V., Rocken, C., & Hunt, D. C. (1999). Analysis and validation of GPS/MET radio occultation data in the ionosphere. *Radio Science*, *34*(4), 949–966, https://doi.org/10.1029/1999RS900034.

Schreiner, W. S., et al. (2020). COSMIC-2 radio occultation constellation: First results. *Geophysical Research Letters*, *47*(4), https://doi.org/10.1086/160554.

Schumacher, V., Fernández, A., Justino, F., & Comin, A. (2020). WRF high resolution dynamical downscaling of precipitation for the Central Andes of Chile and Argentina. *Frontiers in Earth Science*, *8*(328), https://doi.org/10.3389/feart.2020.00328.

Seluchi, M. E. & Marengo, J. A. (2000). Tropical–midlatitude exchange of air masses during summer and winter in South America: Climatic aspects and examples of intense events. *International Journal of Climatology: A Journal of the Royal Meteorological Society*, *20*(10), 1167–1190, https://doi.org/10.1002/1097-0088(200008)20:10<1167::AID-JOC526>3.0.CO;2-T.

Semmling, A., et al. (2014). Sea surface topography retrieved from GNSS reflectometry phase data of the GEOHALO flight mission. *Geophysical Research Letters*, *41*(3), 954–960, https://doi.org/10.1002/2013GL058725.

Senyurek, V., Lei, F., Boyd, D., Gurbuz, A. C., Kurum, M., & Moorhead, R. (2020). Evaluations of machine learning-based CYGNSS soil moisture estimates against SMAP observations. *Remote Sensing*, *12*(21), 3503, https://doi.org/10.3390/rs12213503.

Shi, J., Xu, C., Guo, J., & Gao, Y. (2014). Real-Time GPS Precise Point Positioning-Based Precipitable Water Vapor Estimation for Rainfall Monitoring and Forecasting. *IEEE Transactions on Geoscience and Remote Sensing*, *53*(6), 3452–3459, https://doi.org/10.1109/TGRS.2014.2377041.

Shokrana, M. S. B. & Ghane, E. (2020). Measurement of soil water characteristic curve using HYPROP2. *MethodsX*, *7*, 100840, https://doi.org/10.1016/j.mex.2020.100840.

Shukla, M. K. (2013). *Soil physics: An introduction*. CRC press. ISBN 978-1-4398-8842-1.

Silva, V. B. & Kousky, V. E. (2012). The South American monsoon system: Climatology and variability. *Modern Climatology*, *123*, 152, https://doi.org/10.5772/38565.

Silva Dias, P. L., Schubert, W. H., & DeMaria, M. (1983). Large-scale response of the tropical atmosphere to transient convection. *Journal of the Atmospheric Sciences*, *40*(11), 2689–2707, https://doi.org/10.1175/1520-0469(1983)040<2689:LSROTT>2.0.CO;2.

Simeonov, T. (2021). Derivation and analysis of atmospheric water vapour and soil moisture from ground-based GNSS stations (PhD Thesis) (pp. 71–116). Technische Universität Berlin, Berlin, Germany. Available online: https://depositonce.tu-berlin.de/handle/11303/12638. Accessed: 08.02.2023.

Simons, M., Galetzka, J. E., Genrich, J. F., Ortega, F., Comte, D., Glass, B., & Gonzalez, G. (2010a). Central Andean Tectonic Observatory Geodetic Array - CBAA-Cordon Barros Arana P.S. https://doi.org/10.7283/T52J68XN.

Simons, M., Galetzka, J. E., Genrich, J. F., Ortega, F., Comte, D., Glass, B., & Gonzalez, G. (2010b). Central Andean Tectonic Observatory Geodetic Array - CJNT-Chajnantor P.S. https://doi.org/10.7283/T5B27S9T.

Sinha, A. & Harries, J. E. (1995). Water vapour and greenhouse trapping: The role of far infrared absorption. *Geophysical Research Letters*, *22*(16), 2147–2150, https://doi.org/10.1029/95GL01891.

Small, E. E., Larson, K. M., Chew, C. C., Dong, J., & Ochsner, T. E. (2016). Validation of GPS-IR soil moisture retrievals: Comparison of different algorithms to remove vegetation effects. *IEEE Journal of Selected Topics in Applied Earth Observations and Remote Sensing*, *9*(10), 4759–4770, https://doi.org/10.1109/JSTARS.2015.2504527.

Smalley, J. R. & Bennett, R. (2015a). CAP Andes GPS Network - LVRA-Liviara P.S. https://doi.org/10.7283/T5TB1596.

Smalley, J. R. & Bennett, R. (2015b). CAP Andes GPS Network - SCTC-Santa Catalina P.S. https://doi.org/10.7283/T52V2DHH.

Smalley, J. R. & Bennett, R. (2015c). CAP Andes GPS Network - YAVC-Yavi P.S. https://doi.org/10.7283/T5Z31X1J.

Smalley, J. R. & Bennett, R. (2015d). Puna-Andes GPS Network - GOLG-GOLG P.S. https://doi.org/10.7283/T59C6VTS.

Smalley, J. R. & Bennett, R. (2015e). Puna-Andes GPS Network - SALC-SALC P.S. https://doi.org/10.7283/T5PN9413.

Smalley, J. R. & Bennett, R. (2015f). Puna-Andes GPS Network - SRSA-SRSA P.S. https://doi.org/10.7283/T5F47MJH.

Smalley, J. R. & Bennett, R. (2015g). Puna-Andes GPS Network - TUZG-TUZG P.S. https://doi.org/10.7283/T5JW8C9C.

Smith, E. K. & Weintraub, S. (1953). The constants in the equation for atmospheric refractive index at radio frequencies. *Proceedings of the IRE*, *41*(8), 1035–1037, https://doi.org/10.1109/JRPROC.1953.274297.

Srivastava, P. K. (2017). Satellite soil moisture: Review of theory and applications in water resources. *Water Resources Management*, *31*(10), 3161–3176, https://doi.org/10.1007/s11269-017-1722-6.

Stansbury, R. S., Towhidnejead, M., Demidovich, N., Greenlow, C., DiNofrio, J., & Edwards, D. (2013). Initial flight tests of uat ads-b unit for suborbital reusable launch vehicles. In *Integrated Communications, Navigation and Surveillance Conference* (pp. 1–11). Herndon, USA: IEEE. https://doi.org/10.1109/ICNSurv.2013.6548528.

Steigenberger, P., Thoelert, S., & Montenbruck, O. (2020). GPS III Vespucci: Results of half a year in orbit. *Advances in Space Research*, *66*(12), 2773–2785, https://doi.org/10.1016/j.asr.2020.03.026.

Steiner, A., Kirchengast, G., Lackner, B., Pirscher, B., Borsche, M., & Foelsche, U. (2009). Atmospheric temperature change detection with GPS radio occultation 1995 to 2008. *Geophysical Research Letters*, *36*(18), https://doi.org/10.1029/2009GL039777.

Steiner, A., Lackner, B., Ladstädter, F., Scherllin-Pirscher, B., Foelsche, U., & Kirchengast, G. (2011). GPS radio occultation for climate monitoring and change detection. *Radio Science*, *46*(6), 1–17, https://doi.org/10.1029/2010RS004614.

Strecker, M., et al. (2007). Tectonics and Climate of the Southern Central Andes. *Annual Review of Earth and Planetary Sciences*, *35*(1), 747–787, https://doi.org/10.1146/annurev.earth.35.031306.140158.

Subirana, J., Zornoza, J., & Hernández-Pajares, M. (2013). Global Navigation Satellite Systems, Volume I: Fundamentals and Algorithms. *ESA Communications ESTEC, Noordwijk, the Netherlands*, *238*. ISBN 978-92-9221-886-7.

Sun, Y., Xue, R., Zhao, D., & Wang, D. (2017). Radio Frequency Compatibility Evaluation of S Band Navigation Signals for Future BeiDou. *Sensors*, *17*(5), 1039, https://doi.org/10.3390/s17051039.

Tavenard, R., et al. (2020). Tslearn, A Machine Learning Toolkit for Time Series Data. *Journal of Machine Learning Research*, *21*(118), 1–6 https://jmlr.org/papers/v21/20-091.html.

Taylor, S. J. & Letham, B. (2018). Forecasting at scale. *The American Statistician*, *72*(1), 37–45, https://doi.org/10.1080/00031305.2017.1380080.

Ter Steege, H., et al. (2013). Hyperdominance in the Amazonian tree flora. *Science*, *342*(6156), https://doi.org/10.1126/science.1243092.

Topp, G. C., Davis, J., & Annan, A. P. (1980). Electromagnetic determination of soil water content: Measurements in coaxial transmission lines. *Water Resources Research*, *16*(3), 574–582, https://doi.org/10.1029/WR016i003p00574.

Tropical Rainfall Measuring Mission (TRMM) (2011). TRMM Combined Precipitation Radar and Microwave Imager Rainfall Profile L2 1.5 hours V7. Goddard Earth Sciences Data and Information Services Center (GES DISC). Available online: https://disc.gsfc.nasa.gov/datacollection/TRMM_2B31_7.htmls. Accessed: 30.05.2022.

Truebner GmbH (2021). Truebner SMT 100. Available online: https://www.truebner.de/en/smt100.php. Accessed: 08.12.2021.

Turner, I. M. (2001). *The ecology of trees in the tropical rain forest*. Cambridge University Press. ISBN 978-0-5210-6374-6.

UCAR (2011). The Troposphere. Available online: https://scied.ucar.edu/learning-zone/atmosphere/troposphere. Accessed: 02.08.2022.

UCAR (2014). The Ionosphere. Available online: https://scied.ucar.edu/learning-zone/atmosphere/ionosphere. Accessed: 02.08.2022.

UCAR (2015). Layers of Earth's Atmosphere. Available online: https://scied.ucar.edu/learning-zone/atmosphere/layers-earths-atmosphere. Accessed: 02.08.2022.

Unwin, M., Jales, P., Tye, J., Gommenginger, C., Foti, G., & Rosello, J. (2016). Spaceborne GNSS-reflectometry on TechDemoSat-1: Early mission operations and exploitation. *IEEE Journal of Selected Topics in Applied Earth Observations and Remote Sensing*, *9*(10), 4525–4539, https://doi.org/10.1109/JSTARS.2016.2603846.

Urquhart, L., Nievinski, F. G., & Santos, M. C. (2012). Ray-traced slant factors for mitigating the tropospheric delay at the observation level. *Journal of Geodesy*, *86*(2), 149–160, https://doi.org/10.1007/s00190-011-0503-x.

Vaquero-Martínez, J. & Antón, M. (2021). Review on the Role of GNSS Meteorology in Monitoring Water Vapor for Atmospheric Physics. *Remote Sensing*, *13*(12), 2287, https://doi.org/10.3390/rs13122287.

Veldkamp, E. & O'Brien, J. J. (2000). Calibration of a frequency domain reflectometry sensor for humid tropical soils of volcanic origin. *Soil Science Society of America Journal*, *64*(5), 1549–1553, https://doi.org/10.2136/sssaj2000.6451549x.

Vera, C., et al. (2006). Toward a unified view of the American monsoon systems. *Journal of Climate*, *19*(20), 4977–5000, https://doi.org/10.1175/JCLI3896.1.

Vernekar, A. D., Kirtman, B. P., & Fennessy, M. J. (2003). Low-Level Jets and Their Effects on the South American Summer Climate as Simulated by the NCEP Eta Model. *Journal of Climate*, *16*(2), 297–311, https://doi.org/10.1175/1520-0442(2003)016<0297:LLJATE>2.0.CO;2.

Vey, S., Güntner, A., Wickert, J., Blume, T., & Ramatschi, M. (2016a). Long-term soil moisture dynamics derived from GNSS interferometric reflectometry: a case study for Sutherland, South Africa. *GPS Solutions*, *20*(4), 641–654, https://doi.org/10.1007/s10291-015-0474-0.

Vey, S., Güntner, A., Wickert, J., Blume, T., Thoss, H., & Ramatschi, M. (2016b). Monitoring snow depth by GNSS reflectometry in built-up areas: A case study for Wettzell, Germany. *IEEE Journal of selected topics in applied Earth observations and Remote Sensing*, *9*(10), 4809–4816, https://doi.org/10.1109/JSTARS.2016.2516041.

Virtanen, P., et al. (2020). SciPy 1.0: Fundamental Algorithms for Scientific Computing in Python. *Nature Methods*, *17*, 261–272, https://doi.org/10.1038/s41592-019-0686-2.

Vrije Universiteit Amsterdam (2021). VUA-NASA Land Parameter Retrieval Model. Available online: https://www.geo.vu.nl/~jeur/lprm. Accessed: 09.12.2021.

Wanders, N., Karssenberg, D., Roo, A. d., De Jong, S., & Bierkens, M. (2014). The suitability of remotely sensed soil moisture for improving operational flood forecasting. *Hydrology and Earth System Sciences*, *18*(6), 2343–2357, https://doi.org/10.5194/hess-18-2343-2014.

Wang, S., et al. (2020). Evaluation of precipitable water vapor from five reanalysis products with ground-based GNSS observations. *Remote Sensing*, *12*(11), 1817, https://doi.org/10.3390/rs12111817.

White, E. P., Enquist, B. J., & Green, J. L. (2008). On estimating the exponent of power-law frequency distributions. *Ecology*, *89*(4), 905–912, https://doi.org/10.1890/07-1288.1.

Wickert, J., Beyerle, G., Hajj, G. A., Schwieger, V., & Reigber, C. (2002). GPS radio occultation with CHAMP: Atmospheric profiling utilizing the space-based single difference technique. *Geophysical Research Letters*, *29*(8), 28–1, https://doi.org/10.1029/2001GL013982.

Wickert, J., et al. (2005). GPS radio occultation with CHAMP and GRACE: A first look at a new and promising satellite configuration for global atmospheric sounding. In *Annales Geophysicae*, volume 23 (pp. 653–658).: Copernicus GmbH. https://doi.org/10.5194/angeo-23-653-2005.

Wickert, J., et al. (2020). GNSS Remote Sensing at GFZ: Overview and Recent Results. *ZfV: Zeitschrift für Geodäsie, Geoinformation und Landmanagement*, *145*(5), 266–278, https://doi.org/10.12902/zfv-0320-2020.

Wickert, J., Galas, R., Beyerle, G., König, R., & Reigber, C. (2001a). GPS ground station data for CHAMP radio occultation measurements. *Physics and Chemistry of the Earth, Part A: Solid Earth and Geodesy*, *26*(6-8), 503–511, https://doi.org/10.1016/S1464-1895(01)00092-8.

Wickert, J., et al. (2001b). Atmosphere sounding by GPS radio occultation: First results from CHAMP. *Geophysical Research Letters*, *28*(17), 3263–3266, https://doi.org/10.1029/2001GL013117.

Wilgan, K., Rohm, W., & Bosy, J. (2015). Multi-observation meteorological and GNSS data comparison with Numerical Weather Prediction model. *Atmospheric Research*, *156*, 29–42, https://doi.org/10.1016/j.atmosres.2014.12.011.

Woo, K. (2000). Optimum semicodeless carrier-phase tracking of L2. *Navigation*, *47*(2), 82–99, https://doi.org/10.1002/j.2161-4296.2000.tb00204.x.

World Meteorological Organization (2021a). Global Observing System. Available online: https://public.wmo.int/en/programmes/global-observing-system. Accessed: 03.12.2021.

World Meteorological Organization (2021b). Observing Systems Capability Analysis and Review Tool : IASI. Available online: https://space.oscar.wmo.int/instruments/view/iasi. Accessed: 07.12.2021.

World Meteorological Organization (2021c). Observing Systems Capability Analysis and Review Tool : MVIRI. Available online: https://space.oscar.wmo.int/instruments/view/mviri. Accessed: 07.12.2021.

World Meteorological Organization (2021d). Observing Systems Capability Analysis and Review Tool : SEVIRI. Available online: https://space.oscar.wmo.int/instruments/view/seviri. Accessed: 07.12.2021.

Wübbena, G., Schmitz, M., Boettcher, G., & Schumann, C. (2006). Absolute GNSS antenna calibration with a robot: repeatability of phase variations, calibration of GLONASS and determination of carrier-to-noise pattern. In *Proceedings of the IGS Workshop* (pp. 8–12).

Wübbena, G., Schmitz, M., & Matzke, N. (2010). On GNSS in-situ station calibration of near-field multipath. In *International symposium on GNSS space based and ground based augmentation systems and applications, Brussels, Belgium*.

Xu, G. & Xu, Y. (2016). *GPS: Theory, Algorithms and Applications*. Berlin, Germany: Springer, 3 edition. ISBN 978-366-250-365-2.

Yang, H. & Gao, Y. (2017). GPS satellite orbit prediction at user end for real-time PPP system. *Sensors*, *17*(9), 1981, https://doi.org/10.3390/s17091981.

Yang, L., Gao, J., Zhu, D., Zheng, N., & Li, Z. (2020). Improved Zenith Tropospheric Delay Modeling Using the Piecewise Model of Atmospheric Refractivity. *Remote Sensing*, *12*(23), 3876, https://doi.org/10.3390/rs12233876.

Yang, T., et al. (2019). Land surface characterization using BeiDou signal-to-noise ratio observations. *GPS Solutions*, *23*(2), 1–12, https://doi.org/10.1007/s10291-019-0824-4.

Yang, Y., Tang, J., & Montenbruck, O. (2017). Chinese Navigation Satellite Systems. In *Springer Handbook of Global Navigation Satellite Systems* (pp. 273–304). Springer. https://doi.org/10.1007/978-3-319-42928-1_10.

Yeh, T.-K., Hwang, C., Xu, G., Wang, C.-S., & Lee, C.-C. (2009). Determination of global positioning system (GPS) receiver clock errors: impact on positioning accuracy. *Measurement Science and Technology*, *20*(7), 075105, https://doi.org/10.1088/0957-0233/20/7/075105.

Yu, K., Rizos, C., Burrage, D., Dempster, A. G., Zhang, K., & Markgraf, M. (2014). An overview of GNSS remote sensing. *EURASIP Journal on Advances in Signal Processing*, *2014*(1), 1–14, https://doi.org/10.1186/1687-6180-2014-134.

Yunck, T., Parkinson, B., & Spilker, J. (1996). Global Positioning System: Theory and Applications. *AIAA, Washington, DC*.

Zavorotny, V. U., Gleason, S., Cardellach, E., & Camps, A. (2014). Tutorial on remote sensing using GNSS bistatic radar of opportunity. *IEEE Geoscience and Remote Sensing Magazine*, *2*(4), 8–45, https://doi.org/10.1109/MGRS.2014.2374220.

Zhang, C., Li, X., Gao, S., Lin, T., & Wang, L. (2017). Performance analysis of global navigation satellite system signal acquisition aided by different grade inertial navigation system under highly dynamic conditions. *Sensors*, *17*(5), 980, https://doi.org/10.3390/s17050980.

Zhang, X., Li, X., & Guo, F. (2011). Satellite clock estimation at 1 Hz for realtime kinematic PPP applications. *GPS Solutions*, *15*(4), 315–324, https://doi.org/10.1007/s10291-010-0191-7.

Zinner, T., Mannstein, H., & Tafferner, A. (2008). Cb-TRAM: Tracking and monitoring severe convection from onset over rapid development to mature phase using multi-channel Meteosat-8 SEVIRI data. *Meteorology and Atmospheric Physics*, *101*(3), 191–210, https://doi.org/10.1007/s00703-008-0290-y.

Zreda, M., Desilets, D., Ferré, T., & Scott, R. L. (2008). Measuring soil moisture content non-invasively at intermediate spatial scale using cosmic-ray neutrons. *Geophysical Research Letters*, *35*(21), https://doi.org/10.1029/2008GL035655.

Zreda, M., Shuttleworth, W., Zeng, X., Zweck, C., Desilets, D., Franz, T., & Rosolem, R. (2012). COSMOS: The cosmic-ray soil moisture observing system. *Hydrology and Earth System Sciences*, *16*(11), 4079–4099, https://doi.org/10.5194/hess-16-4079-2012.

Zus, F., Balidakis, K., Dick, G., Wilgan, K., & Wickert, J. (2021). Impact of tropospheric mismodelling in GNSS precise point positioning: a simulation study utilizing ray-traced tropospheric delays from a high-resolution NWM. *Remote Sensing*, *13*(19), 3944, https://doi.org/10.3390/rs13193944.

Zus, F., Bender, M., Deng, Z., Dick, G., Heise, S., Shang-Guan, M., & Wickert, J. (2012). A methodology to compute GPS slant total delays in a numerical weather model. *Radio Science*, *47*(2), 1–15, https://doi.org/10.1029/2011RS004853.

Zus, F., Dick, G., Douša, J., Heise, S., & Wickert, J. (2014). The rapid and precise computation of GPS slant total delays and mapping factors utilizing a numerical weather model. *Radio Science*, *49*(3), 207–216, https://doi.org/10.1002/2013RS005280.

Zus, F., Wickert, J., Bauer, H. S., Schwitalla, T., & Wulfmeyer, V. (2011). Experiments of GPS slant path data assimilation with an advanced MM5 4DVAR system. *Meteorologische Zeitschrift*, *20*(2), 173–184, https://doi.org/10.1127/0941-2948/2011/0232.